A NOVEL MINIMALLY INVASIVE DUAL-MODALITY FIBER OPTIC PROBE FOR PROSTATE CANCER DETECTION

by

VIKRANT SHARMA

Presented to the Faculty of the Graduate School of

The University of Texas at Arlington in Partial Fulfillment

of the Requirements

for the Degree of

DOCTOR OF PHILOSOPHY

THE UNIVERSITY OF TEXAS AT ARLINGTON

August 2012

ACKNOWLEDGEMENTS

My Ph.D. journey was a wonderful expedition, full of accomplishments and rewards. There are many people I am grateful to, for giving me unique learning experiences and helping me in one way or the other towards my goal. First and foremost, I would like to thank my Mentor, Dr. Hanli Liu, who has been an excellent influence, always providing me an independent platform to work with, giving ample opportunities for leadership, research and development, and publications, thus making me a better researcher, and individual. Her passion and dedication to her work along with her kind heart and excellent collaborative skills have given me a lot of inspiration throughout times. I am very thankful to have her as my Mentor.

I was extremely blessed to have an excellent Ph.D. committee, and would like to individually thank all my committee members from UT Arlington and UT Southwestern. It was a privilege to work with Dr. Jeffrey Cadeddu, and I thank him for the clinical collaboration, and for providing me with essential criticisms and suggestions, related to practical clinical implementation issues. It certainly gave a better shape to my dissertation. I am extremely grateful to Dr. Payal Kapur, for her help and support for histopathology aspect of my study. Her undying research spirit, willingness and availability for my project, and highly efficient throughput were essential components towards successful completion of my work. I also express my gratitude to Dr. Jer-Tsong Hsieh, who is an excellent researcher and collaborator. Working with him was highly efficient and fruitful and at the same time seemed very effortless, given the resources and expertise he provided. Lastly but not the least, I am extremely thankful to Dr. Geroge Alexandrakis, for always being available for discussions, and for providing theoretical and technical support. I learned a lot from him inside and outside of the classroom.

Apart from my committee members, there are other faculty members who have been very helpful for my study. I am grateful to Dr. Claus Roehrborn from UTSW, for his valuable

suggestions and comments, and for clinical collaboration. I am also thankful to Dr. Ephrem Olweny for his help in patient selection and conduct of clinical study and to Dr. Wareef Kabbani and Dr. Yan Peng for histopathology evaluations. I am immensely thankful to Dr. David Euhus for presenting me with the clinical problem of breast cancer margin detection, and collaborative research thereafter. I sincerely thank Drs. Karol and Ignacy Gryczynski from TCU and UNTHSC, respectively, for their invaluable expert advice and collaboration during fluorescence lifetime validation experiments. I also acknowledge Dr. Khosrow Behbehani, Dr. Digant Dave, Dr. Liping Tang, Dr. Kytai Nguyen, and Dr. Mario Romero, and Dr. Baohong Yuan at UT Arlington, for positively influencing my work directly or indirectly through coursework and/or research collaborations. I am extremely grateful to Dr. Nancy Rowe, for her support in statistical analysis and her willingness for frequent and timely discussions.

I was very fortunate to have support of my colleagues and friends inside and outside my laboratory. I specifically thank Dr. Dheerendra Kashyap, Ms. Sweta Narvenkar, Mr. Nimit Patel, Ms. Shivaranjani Shivalingaiah, and Ms. Ronak Patel, for their contributions at various points during the development of my work. I also thank my colleagues, Dr. Fenghua Tian, Mr. Venkaiah Kavuri, and Mr. Peter Leboullec, for excellent professional companionship and enriching discussions at various times. Outside my lab, I thank Dr. Ashwin Nair and Dr. Aniket Wadajkar, for their friendship and their help and willingness to provide appropriate resources. I am also thankful to all my other lab mates and colleagues.

My family is an integral part of my identity. I am blessed to have two loving sisters, Pooja Sharma and Aarti Sawhney, who along with my brother-in-laws, Vivek Sharma and Sumeet Sawhney, respectively, have shown immense faith in me and encouraged me at all times. My Parents, Dr. M.L. Sharma and Dr. Bimla Sharma are a constant source of inspiration for me, and their love and support has been a major asset towards my successes in past and present. I am also extremely grateful to my wife, Nidhi Sharma, who stepped into my life at the

start of my Ph.D., for her companionship during this momentous journey, and for enduring the idiosyncrasies that are integral part of a Ph.D. student's life.

Finally, I as a believer in a higher power, I am grateful and dedicate my work to God almighty, for giving me the intellect and ability to get this far, and I pray for continuous improvement in both personal and professional domains, as long as I live.

August 7, 2012

ABSTRACT

A NOVEL MINIMALLY INVASIVE DUAL-MODALITY FIBER

OPTIC PROBE FOR PROSTATE CANCER DETECTION

Vikrant Sharma, PhD

The University of Texas at Arlington, 2012

Supervising Professor: Hanli Liu

Prostate cancer is the most common form of cancer in males, and is the second leading cause of cancer related deaths in United States. In prostate cancer diagnostics and theapy, there is a critical need for a minimally invasive tool for in vivo evaluation of prostate tissue. Such a tool finds its niche in improving TRUS (trans-rectal ultrasound) guided biopsy procedure, surgical margin assessment during radical prostatectomy, and active surveillance of patients with a certain risk levels. This work is focused on development of a fiber-based dual-modality optical device (*dMOD*), to differentiate prostate cancer from benign tissue, *in vivo*. *dMOD* utilizes two independent optical techniques, LRS (light reflectance spectroscopy) and AFLS (auto-fluorescence lifetime spectroscopy). LRS quantifies scattering coefficient of the tissue, as well as concentrations of major tissue chromophores like hemoglobin derivatives, β-carotene and melanin. AFLS was designed to target lifetime signatures of multiple endogenous fluorophores like flavins, porphyrins and lipo-pigments. Each of these methods was independently developed, and the two modalities were integrated using a thin (1-mm outer diameter) fiber-optic probe. Resulting *dMOD* probe was implemented and evaluated on animal models of prostate cancer, as well as on human prostate tissue. Application of *dMOD* to human breast cancer (invasive ductal carcinoma) identification was also evaluated.

The results obtained reveal that both LRS and AFLS are excellent techniques to discriminate prostate cancer tissue from surrounding benign tissue in animal models. Each technique independently is capable of providing near absolute (100%) accuracy for cancer detection, indicating that either of them could be used independently without the need of implementing them together. Also, in case of human breast cancer, LRS and AFLS provided comparable accuracies to *dMOD*, LRS accuracy (96%) being the highest for the studied population.

However, the dual-modality integration proved to be ideal for human prostate cancer detection, as *dMOD* provided much better accuracy i.e., 82.7% for cancer detection in intra-capsular prostatic tissues (ICT), and 92.4% for cancer detection in extra-capsular prostatic tissues (ECT), when compared with either LRS (74.7% ICT, 86.6% ECT) or AFLS(67.1% ICT, 82.1% ECT) alone. A classification algorithm was also developed to identify different grades of prostate cancers based on Gleason scores (GS). When stratified by grade, each high grade prostate cancer (GS 7, 8 and 9) was successfully identified using *dMOD* with excellent accuracy in ICT (88%, 90%, 85%), as well as ECT (91%, 92%, 94%).

TABLE OF CONTENTS

LIST OF ILLUSTRATIONS

LIST OF TABLES

CHAPTER 1

INTRODUCTION

Cancer detection is the first step towards the management of this deadly disease. Current gold standards in cancer diagnosis rely on histopathology for final decisions. However, there are many critical situations in clinical settings where waiting for a histopathology decision poses significant drawbacks. One such clinical situation is prostate biopsy, where due to of the lack of definitive imaging techniques, the prostate tissue is sampled in a pseudo-random fashion. Multiple cores (sometimes more than 30) typically measuring 18 mm X 1 mm are resected for pathological analysis. This crude way of biopsy causes injury and related side effects to the prostate tissue, while still missing about 30% of the cancers. Another critical situation is the surgical removal of the cancer bearing tissue, where the goal of a Surgeon is to remove either partial (e.g. Lumpectomy, breast cancer) or whole organ (e.g. Prostatectomy) that has cancer. However, whether there is any cancer left over in the body is decided by histopathology results, where the margins of the resected tissues are analyzed, and labeled as positive if cancer is found on the surface, or negative otherwise. In case of positive margins (20-50% incidence in lumpectomies), the patients either have to go through re-surgery, or explore other treatment options to overcome the leftover traces of cancer. Either of these options would lead to increased cost, and distress to the patient, and are highly undesirable.

The goal of my research is to develop a minimally invasive fiber optic probe that can detect prostate cancer *in vivo*, in a minimally invasive way, with clinically acceptable sensitivity and specificity, so clinicians can make decisions on-site in the above mentioned situations to improve the outcome of biopsy/surgical procedures.

1.1 Background and Motivation

1.1.1 Prostate Gland

Prostate gland is a walnut sized male organ that surrounds the urethra, is located just below the urinary bladder, in front of the rectum and above the penis (see Fig. 1.1). The primary function of the gland is to provide enzymes to the seminal fluid, to maintain its fluid nature, and to also provide nutrients that protect sperms, which originated from the testes and travel through vas deferens into the prostatic urethra before ejaculation.

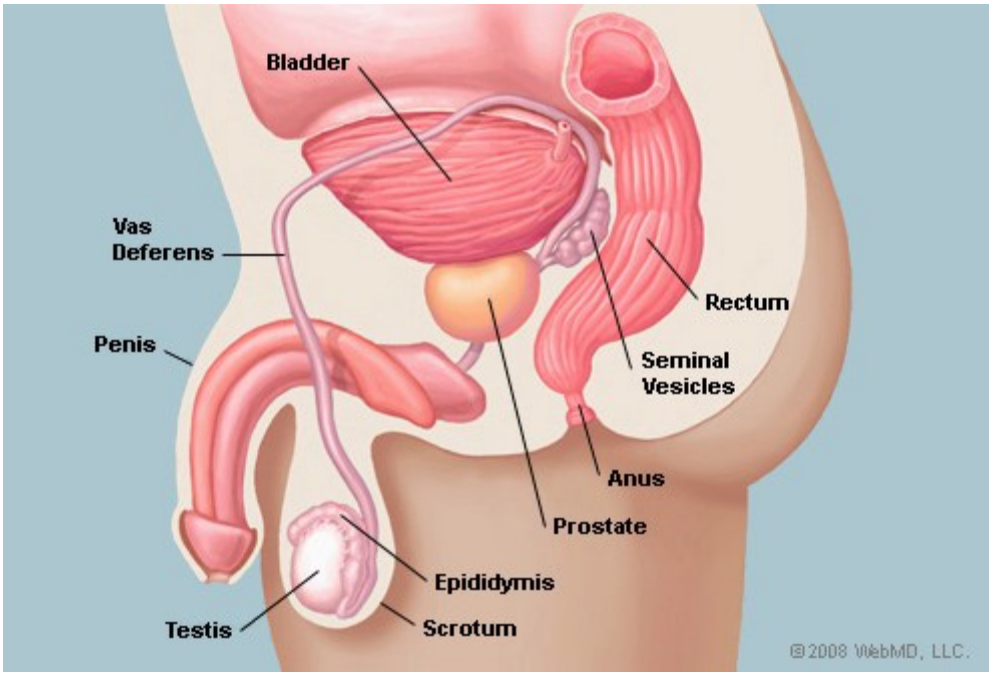

Fig. 1.1 Prostate Anatomy (Image source: http://men.webmd.com/picture-of-the-prostate)

1.1.2 Prostate Cancer Incidence and Current Clinical Needs

Prostate cancer is the most commonly found male cancer in the United States and is the second leading cause of death from cancer in men[1]. In 2011 alone, the number of new prostate cancer cases were estimated to be 240,890, resulting in estimated 33,720 deaths in US[2]. At present, digital rectal examination (DRE), prostate specific antigen (PSA) blood test, and transrectal ultrasound (TRUS) guided biopsy are the clinically available techniques for

prostate cancer screening and diagnosis. Among these, DRE and PSA are the used as screening tools for prostate cancer. For example, a hard lump felt though DRE and/or an elevated PSA level (> 3.0g/ml)[3] could be an indicator of prostate cancer. With abnormal screening results, the gold standard for prostate cancer diagnosis is TRUS guided needle biopsy, which involves resection of multiple cores of prostate tissue with the guidance of an ultrasound probe.

1.1.2.1 Gleason Grading system

Gleason grading system is named after Dr. Donald F. Gleason[4], and is used to predict the aggressiveness of prostate cancer. Gleason grading system is the current gold standard for reporting the histological analysis. Gleason score, which is calculated on TRUS-guided biopsy samples, is critical for further prognostic planning and management.

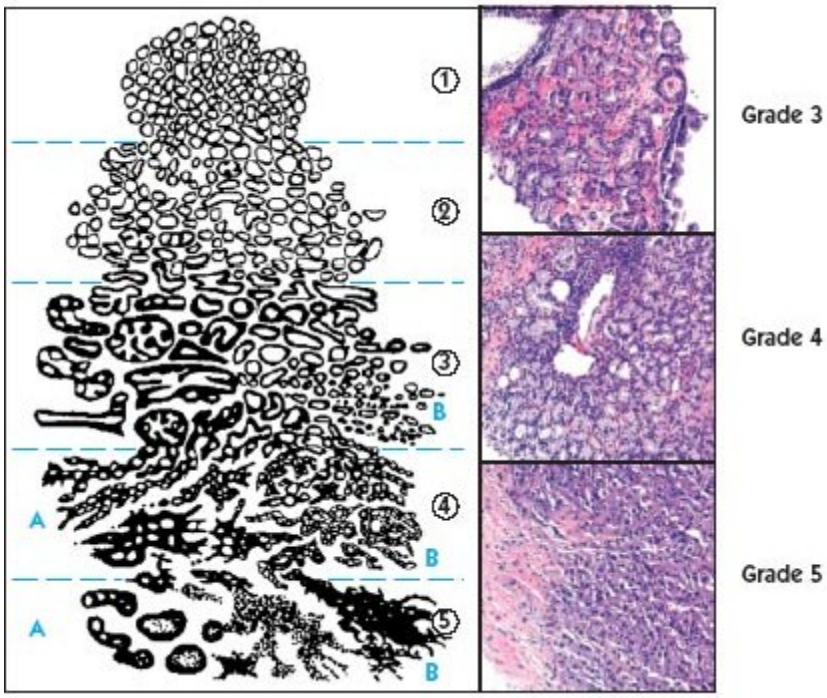

Fig. 1.2 Gleason grading system diagram and illustration (image source: http://www.prostate-cancer.org/pcricms/node/165)

As shown in Fig. 1.2, a grade is assigned based on loss of normal glandular structure including size, shape and differentiation of glands. Grade 1&2 represent closely packed glands forming a nodule. They represent indolent disease, which is rarely progressive. Grade 3 is characterized by small infiltrating glands and complete lumen formation. This is the most commonly observed pattern. In Grade 4, the glands are fused, has incomplete lumen formation, and indicates tumor progression. Grade 5 is characterized by solid sheet or single cell, with no lumen formation[5]. Gleason sum or Gleason score (GS) is assigned by identifying two major Gleason grades present during histological evaluation, and adding them. For example, if primary pattern observed is Grade 3, and secondary pattern observed is Grade 4, then GS is reported to be 7(3+4). Typically, there are multiple foci of prostate cancer, of which primary and secondary patterns are identified. Sometimes, tertiary pattern is also reported[5].

According to EAU (European Association of Urology) guidelines[3] of prostate cancer, active surveillance of the disease is recommended for prostate cancer with GS ≥ 7, which is termed high grade cancer. Thus identifying GS 7, 8, and 9 is highly relevant for clinical prognosis.

Staging of prostate cancer is done based on various factors, like GS, DRE results, PSA levels, and imaging (MRI) results. A detailed description of different stages of prostate cancer is out of scope of this work, and can be found here[5].

1.1.2.2 Clinical problem I: Prostate Biopsy

In TRUS guided biopsy procedure, although ultrasound is able to provide high resolution anatomical images, it lacks the sensitivity in differentiating tumor from normal tissue, especially at early stages, making TRUS guided biopsy a rather “blind” procedure involving quasi-random sampling of the prostate tissue[6]. This drawback leads to a high rate of false negatives, missing cancer in 25% or more cases[7] and requires oversampling of tissue due to non-specific targeting. The current standard biopsy procedure involves resection of 10-12 needle cores, in a predetermined systematic random pattern. Patients often have to go for

secondary biopsies, if the symptoms do not subside, for example: if PSA levels continue to elevate.

It was also hypothesized that by increasing the number of core biopsies, the accuracy in detecting cancer could be improved[8]. However, recent studies [9,10], have shown that there is no significant improvement in detection rates with saturation biopsies (although further studies are warranted to confirm with larger sample size[11]) which typically involve 20-30 cores and could be up to 80 cores. Moreover, increasing the number of cores often results in medical complications associated with the biopsy procedure[8].

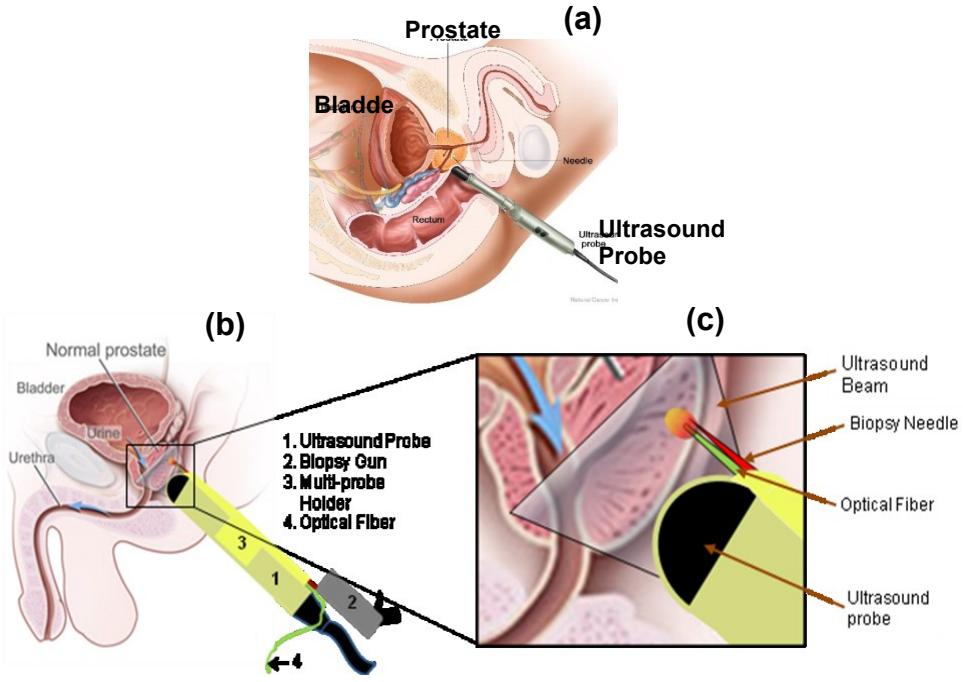

Fig. 1.3 (a) schematic drawing of a TRUS probe inserted into a human rectum; (b) an enlarged diagram showing the human anatomy, a TRUS probe with our designed fiber probe attached; (c) a further enlarged drawing focusing on the posterior of the prostate, the head of TRUS probe, the biopsy needle, and the designed optical fiber tip.

It is thus imperative to develop a technique that addresses the drawbacks of current biopsy procedure, increasing the accuracy of detection, as well as reducing injury and inflammation caused by conventional biopsy procedure. A TRUS guided minimally invasive

optical probe could provide real time detection of cancer tissue, which in turn would allow the surgeons to search for cancer on-site, thus providing them with more flexibility to explore the prostatic tissue for cancer, as well as enabling them to assess the extent of tumor once found. Such a probe would be highly significant in clinical practices as it will improve the accuracy of prostate cancer diagnosis, while reducing the related injury to the tissue.Figure 1.3 represents a conceptual implementation of optical aid for prostate biopsy procedure[12]. Fig. 1.3(a) shows a conventional end-fire TRUS probe, with a biopsy needle. Fig. 1.3(b) and (c) show a possible design improvement for optical biopsy of prostate. Incorporation of optical fiber is highly compatible with the way biopsy is currently performed.

The major advantages of optical biopsy for prostate would be:

a) Real time feedback of tissue condition, allowing clinicians to optimize the sampling on site, to improve the outcome of biopsy, potentially reducing number of secondary biopsies.

b) Since optical biopsy does not involve removal of tissue, the number of cores or the volume of tissue sampled would be drastically reduced, minimizing injury and related complications[13,14].

c) This minimally invasive approach can also be useful for active surveillance of the disease, especially useful, if the optical approach can distinctly identify different grades of prostate cancer.

1.1.2.3 Clinical problem II: Positive Surgical Margins in Radical Prostatectomy

Another critical clinical problem that needs an *in vivo* monitoring tool is surgical margin assessment during radical prostatectomy (RP) for localized prostate cancer[15]. A comprehensive review[16] reported occurrence of positive surgical margins (PSM) in RP for up to 38% of the cases. Presence of PSM is an adverse outcome[17] leading to various prognostic effects based on margin location and its extent[18]. At present, histopathology is the gold standard for detecting positive surgical margins, which takes a few days, whereas an alternative that could assess the

margins during RP procedure is much desired. In this way, surgeons can remove the residual cancer on-site, thus eliminating the need for post-surgical treatment options, which comes with additional trauma and associated costs. Fig. 1.4 shows an example of fiber optic probe, that could be used with different number of fiber channels (4 in this illustration), and be compatible with the robotic RP surgery set-up. The exact design could be customized for desired coverage area and resolution, but the illustration (Fig. 1.3) essentially provides a possibility of implementation.

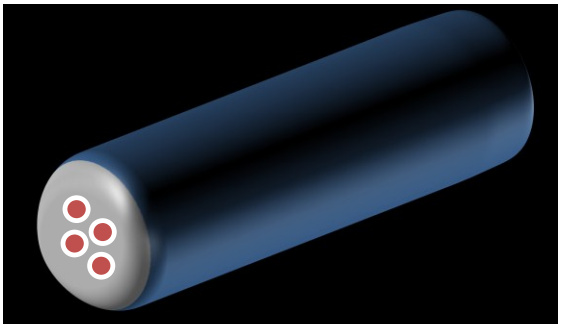

Fig. 1.4 A schematic depicting design of an optical fiber based endoscopic margin assessment tool.

1.2 Dual-Modality Optical Device (*dMOD*) as a solution

There is multitude of optical technologies available for tissue spectroscopy and imaging. Cancer tissue is known to have different morphological and physiological properties when compared to normal tissues given their abnormal growth, with a possibility of an underlying different biochemical environment. In order to exploit these differences from the non-cancer tissue environment, I chose two optical techniques to identify biomarkers (or pre-biomarkers, PB's) of prostate cancer. The proposed dual-modality optical device (*dMOD*) incorporates two independent optical techniques, namely light reflectance spectroscopy (LRS) and auto-fluorescence lifetime spectroscopy (AFLS), in a thin, needle-like fiber optic probe, to detect prostate cancer.

Light reflectance spectroscopy (LRS), also referred to as optical reflectance spectroscopy (ORS) or diffuse reflectance spectroscopy (DRS), has been utilized in various

medical applications to identify tissue types[19], or to differentiate diseased/cancerous tissue from normal/benign tissue[20-22]. Tissue optical properties may themselves serve as biomarkers to differentiate cancerous lesions as light scattering and absorption are highly dependent on morphological and physiological state of the tissue. Typically, LRS uses a broadband light source, and a spectrometer to collect the diffuse reflectance spectra of the tissue in visible and near-infrared range, and uses the spectra to either quantify the absorption and scattering of biological tissues[23], or use characteristic signatures in the spectrum to differentiate tissue types[19]. Quantifying absorption yields the concentrations of chromophores like hemoglobin, and scattering gives an assessment of cell size and density. Given that most tumor microenvironments have abnormal vasculature and cell morphology, LRS makes an excellent candidate for detecting cancer biomarkers.

Fluorescence emission, in contrast to light scattering methods, is shifted towards longer wavelengths as compared to the impinging illumination. The contrast in this case originates from intrinsic properties of certain biomolecules, and is sensitive to the surrounding biochemical environment. Fluorescence spectroscopy has been used for detection of various cancers[24,25]. As compared to steady-state auto-fluorescence spectroscopy, the advantage of time resolved auto-fluorescence lifetime measurement is the intrinsic nature of lifetime measurements, independent of the intensity of excitation light, providing clear finger prints for cancer identification[26,27].

As stated above, the origins of contrast in both these modalities are distinct, which makes them complimentary to each other. The dual-modality approach is thus expected to have a higher discriminatory power compared to single modality alone, especially in cases like prostate tissue where is contrast is inherently low, as evident by its detectability using conventional imaging modalities. This forms the hypothesis of my work which states that "*It is possible to differentiate prostate cancer from benign tissue with high accuracy, using a dual-*

modality optical device based on LRS and AFLS, with further stratification of prostate cancer by grade, in a fiber-based, minimally invasive, surface sensing geometry".

1.3 Thesis Workflow

In Chapters 2 & 3, a detailed description of LRS and AFLS methods, respectively are given, including theoretical principles, instrumentation and algorithm design. Each of these chapters includes instrument validation with phantom models in comparison with gold standards methods in each modality. Followed by description of each method, Chapter 4 starts with implementation of each modality on a subcutaneous ectopic rat prostate cancer model. Followed by that, the integration of the two modalities using a single fiber-optic probe is described. Lastly, Chapter 4 also describes a second animal study where *dMOD* is evaluated on an orthotopic mice prostate cancer model.

After successful implementation on animal models of prostate cancer, Chapters 5 & 6 describe the *ex vivo* study of human prostate cancer, where the capability of *dMOD* to detect different grades of human prostate cancer in presence of benign tissues is evaluated. The human ex vivo implementation is described in two parts. In Chapter 5 (Part I), prostate cancer detection in intra-capsular prostatic tissue is discussed, which is congruent with the optical biopsy application of *dMOD*. In Chapter 6 (Part II), capability of dMOD for detecting prostate cancer in extra-capsular prostatic tissue is discussed, which is congruent with the application of *dMOD* to surgical margin assessment.

Chapter 7, describes extension of *dMOD*'s applicability to other types of cancer, specifically, human breast cancer. An *ex vivo* feasibility study for detecting breast cancer (invasive ductal carcinoma), is described.

Finally, in Chapter 8, major conclusions of this research are presented, along with the future scope and limitations of this work.

CHAPTER 2

METHOD I: LIGHT REFLECTANCE SPECTROSCOPY

2.1 Introduction

Light reflectance spectroscopy (LRS) (also termed diffuse reflectance spectroscopy (DRS) or optical reflectance spectroscopy (ORS)), with small source-detector (SD) separation is based on the spectral changes introduced into the light that traverses the tissue. Light *absorption* and *scattering* are the two major optical parameters that determine the path of light into the tissue and are highly dependent on the morphological and physiological properties of the tissue. Characterization of these optical parameters allows distinguishing tissue types, enabling the use of LRS for various clinical and preclinical applications. Previously, LRS has been applied to diverse focus areas such as cancer diagnosis[20,22,28,29], neurosurgical guidance[19], pre-clinical disease models[30], and measurement of neural activities[31],among other applications. Due to its potential applicability to a variety of clinical settings, researchers have continuously made efforts to quantify the concentration of absorbers as well as the scattering in the tissue. While theoretical derivations are technically challenging[23], semi-empirical models[32,33] have also been developed for quantification.

Theoretically, a widely used mathematical model to understand the propagation of light, including near infrared (NIR) light, in biological tissues is the diffusion approximation. However, such an approximation has its limitations for LRS with short S-D separation, as the diffusion model is not valid when light travels within a few millimeters or less. Also, the diffusion approximation requires that the absorption coefficient, μ_a, be much smaller in magnitude than the reduced scattering coefficient, μ_s'. Such disparity of magnitudes holds well for larger S-D separations and in region of NIR wavelengths; but in the visible range, μ_a and μ_s' can have comparable magnitudes. It is conspicuous that conventional diffusion theory (without inclusion

of empirical parameters) is not a correct model for probe geometry with small (< 1mm) S-D separation. In 2006, Zonios and Dimou [23] proposed an approach to solve this problem and provided a simple expression associating measured reflectance to light absorption and scattering coefficients. This model was also successfully applied to measure optical properties of benign and malignant skin tissue[29,34].

As compared to empirical models, the absolute quantification of scattering and absorption provides a standardized technique for LRS measurements, attributing physiological meaning to the measured signals. This chapter focusses on quantification of these optical properties based on Zonios's model. The effort was initiated in a previous work[35], where the mathematical model was implemented using an ant colony optimization method, which is a robust global optimization method. However, there were some limitations of the previous model, mainly due to scattering model, therefore leading to larger errors at shorter wavelength ranges[35]. My dissertation work includes improvement of the existing methods to complete implementation of Zonios's model, with evaluation on laboratory phantoms and application to in vivo and ex vivo studies.

2.2 Methods

2.2.1. Instrumentation

A typical LRS set-up involves shining light into the tissue using a broadband light source, and detecting the returning light using a spectrometer, that separates the light into its spectral components, and outputs a wavelength dependent intensity profile of the detected light. Therefore, essential components of LRS set-up are a light source, a spectrometer, a bifurcated optical fiber probe for light delivery and collection, and a computer for control and data acquisition. Fig. 2.1 shows a block diagram of LRS measurement set-up. comprised of a tungsten-halogen light source (HL2000HP, Ocean Optics Inc., Dunedin, FL, USA), a single channel CCD (charge-coupled device) array spectrometer (USB 2000, Ocean Optics, Dunedin, FL USA) in the spectral range of ~350-1000 nm, and a laptop computer. The system was

interfaced with the computer using OOIBase32 software provided by the manufacturer. In Fig 2.1b, components of a USB spectrometer are shown[36]. The detector fiber is connected to the spectrometer through the SMA connector port (1). The detected light is first passed through a slit (2) that determines the amount of incoming light and controls spectral resolution. Then the light is passed through a filter (3) to the collimating mirror (4), which focusses the light onto the grating (5). The grating diffracts the light and directs it to the focusing mirror (6) which focusses the light to L2 detector collection lens (7), which in turn focusses the light onto CCD detector elements (8).

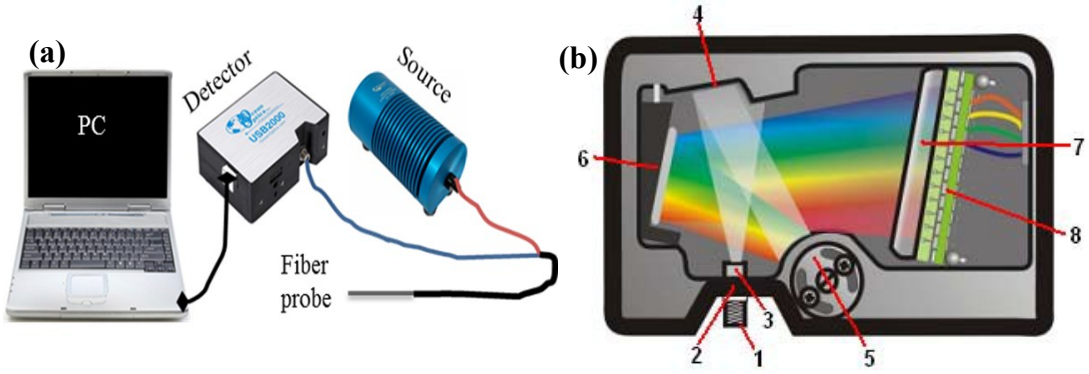

Fig. 2.1 LRS set-up and instrumentation: (a) LRS system components; (b) detailed inside schematic of the detector (USB2000 spectrometer, Ocean Optics, Inc.)[36]

2.2.2. Analytical model for absolute quantification of optical parameters

The model developed by Zonios and Dimou[23] establishes a relationship between the optical reflectance, $R_p(\lambda)$, measured with a short-distance optical probe, the reduced scattering coefficient, $\mu_s'(\lambda)$, and absorption coefficient, $\mu_a(\lambda)$, of the medium, as given below:

$$R_p(\lambda) = \frac{\mu_s'(\lambda)}{k_1 + k_2 \mu_a(\lambda)}. \quad (2.1)$$

All measured spectra, $R_p(\lambda)$, are referenced to a calibration standard (Ocean Optics, Dunedin, FL, USA), which will be referred to as “the white sample” from here onwards. Specifically, $R_p(\lambda)$ represents the spectrum obtained by dividing the measured reflectance, R, by the reference reflectance taken from the white sample. This white sample reference is used to

eliminate the spectral effect of the probe, light source, and detector on the measured reflectance data. In Eq. (2.1), k_1 and k_2 are two calibration parameters depending only on the geometrical characteristics of the optical probes and the optical spectroscopic system, i.e., the light source and detector. In principle, k_1 and k_2 of a selected LRS system can be calibrated experimentally using tissue phantoms. Then, Eq. (2.1) is utilized to quantify both $\mu_a(\lambda)$ and $\mu_s'(\lambda)$ for an unknown tissue sample based on its LRS measurements.

It is well known that $\mu_a(\lambda)$ is a function of chromophore concentrations, most dominant chromophores in 500-800 nm range being deoxygenated hemoglobin, [Hb], oxygenated hemoglobin, [HbO], and water, H_2O. The spectral dependence of μ_a on [HbO], [Hb], and H_2O for blood-perfused tissues can be written as

$$\mu_a(\lambda) = [HbO]\,\varepsilon_{HbO}(\lambda) + [Hb]\,\varepsilon_{Hb}(\lambda) + [\%H_2O]\,\varepsilon_{H_2O}(\lambda), \tag{2.2}$$

where 'λ' is the wavelength in nm, ε_{HbO} (λ), ε_{Hb} (λ) and ε_{H2O} (λ) are the wavelength dependent extinction coefficients of [HbO], [Hb], and water, respectively[37]. [%H2O] represents the percentage of water in the medium. Other chromophores, such as fat, melanin, and beta-carotene may be added to this equation, depending on the wavelength range of interest and tissue type under investigation. The spectral dependence of μs′ can be approximated as given by Mie theory[38]:

$$g = 1.1 - (0.58\times10^{-3})\lambda, \tag{2.3}$$

$$\mu_s' = \mu_s(1-g), \tag{2.4}$$

$$\mu_s = a\lambda^{-b}, \tag{2.5}$$

where μ_s is the effective scattering coefficient, μ_s' is the reduced scattering coefficient, and g is the anisotropy factor. In eq. (5), parameters of a and b are constants and depend on scatterer sizes and types. For 10% intralipid solution[38], the calculated values are a = 2.54x10^9 cm^{-1} and b = 2.4.

2.2.3. Calculation and calibration of k_1 and k_2

The values of k_1 and k_2 can be determined using the least-squares regression approach. By rearranging Eq. (2.1), we obtain

$$\frac{\mu_s'(\lambda)}{R_p(\lambda)} = k_1 + k_2\mu_a(\lambda) \tag{2.6}$$

Eq. (2.6) shows that k_1 and k_2 can be determined by obtaining a linear regression line that best fits $\mu_s'(\lambda)/R_p(\lambda)$ versus $\mu_a(\lambda)$. It is possible to obtain the measured spectra of $R_p(\lambda)$ from the LRS system in the range of 500-850 nm and also achieve quantification of μ_a and μ_s' at 750 nm and 830 nm from ISS oximeter if the measurements by both LRS and ISS oximeter are taken simultaneously. Besides μ_a values, ISS oximeter is also able to provide derived values of [Hb], [HbO], and μ_s' at two wavelengths[39]. Then, wavelength-dependent absorption spectra, $\mu_a(\lambda)$, can be quantified using Eq. (2.2) if the measured [Hb] and [HbO] as well as the hemoglobin extinction coefficients[40] are available. Moreover, given two μ_s' values at two measured wavelengths (750 nm and 830 nm), it is reasonable to interpolate and extrapolate $\mu_s'(\lambda)$ over the desired wavelength range using Eqs. (2.3)-(2.5) based on Mie theory.

During the system calibration phase in my study, I followed the exact principle or procedures given above to acquire $R_p(\lambda)$, $\mu_a(\lambda)$, and $\mu_s'(\lambda)$ from a set of blood-intralipid tissue simulating phantoms (see section 2.1.3.1). A corresponding set of k_1 and k_2 at various total hemoglobin concentrations and reduced scattering coefficients were obtained, averaged, and calculated for their means and standard deviations. If the relative errors for both k_1 and k_2 were less than 10%, then the corresponding set of k_1 and k_2 were accepted as the system calibration parameters for the specific LRS system (i.e., the light source, fiber probe, and spectrometer).

2.2.3.1 Phantom design and experimental set-up

The phantom experiments were designed to simultaneously measure optical properties using two independent optical systems, namely, LRS (which needs to be calibrated), and a gold standard, dual-channel tissue oximeter (OxiplexTS, ISS Inc., IL, USA). The OxiplexTS

measures absolute values of μ_a and μ_s' of the sample under interrogation, thus providing a reference for LRS readings. However, the geometries of the two systems are quite different, i.e. LRS probe is usually ~ 1mm in diameter, whereas OxiplexTS measurement spans a surface area of at least 3.5 cm in longitudinal direction, sensing optical properties over a much larger volume. To account for this mismatch, a large homogenous volume of liquid phantom was used, in a rectangular tank, as shown in Fig. 2.2. Additionally, a magnetic stirrer (not shown) was placed under the tank, to avoid the liquid from settling down, and maintain homogeneity.

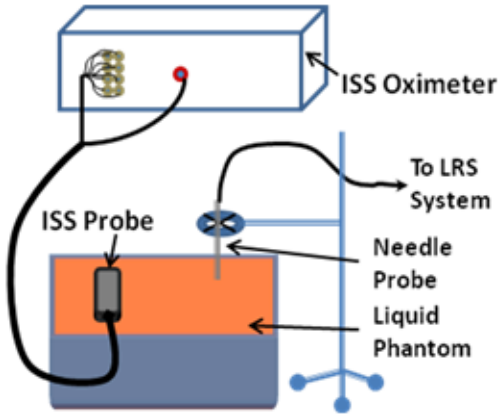

Fig. 2.2 A schematic illustrating the experimental set-up for calibration of k_1 and k_2

The optical fiber probe utilized for this study was a custom built (TechEn, Inc., Milford, MA, USA) bifurcated probe with two multimode fibers: one fiber for light delivery and other for light detection (Fig. 2.1a). The diameter of each multimode fiber was 400 μm, with an average source detector separation of 800 μm. The outer diameter of the fiber probe was 2 mm at the tip. The fiber probe was immersed into the liquid phantom solution with the help of a tripod stand (Fig. 2.2), a few inches away from ISS probe.

To simulate optical properties of biological tissue, blood-intralipid phantoms were utilized for this study. To create a homogenous phantom, a blood-intralipid solution was made by diluting a stock intralipid solution (concentration = 20%, Baxter Healthcare Corporation,

Deerfield, IL) with phosphate buffered saline (PBS) and adding defibrinated horse blood (Hemostat Laboratories, Dixon, CA). The perturbations in absorption and scattering properties were introduced two major methods: (a) Since the intralipid acts as the major scattering agent in the phantom, changing the concentration of intralipid directly introduces a change in scattering coefficient of the phantom; (b) Change in absorption can be achieved either by changing blood volume, or changing relative concentration of the absorbers (i.e., oxy- and deoxy-hemoglobin), by changing oxygenation levels of the phantom. De-oxygenation (reduced oxygen saturation) was achieved by adding yeast to the phantom. 3-4 grams of yeast was enough to deoxygenate a 3 liter phantom in 10-12 minute time frame. Re-oxygenation was then achieved by bubbling 100% oxygenation into the liquid phantom. For the dynamic oxygen saturation phantoms as well as the static phantoms, the uniformity of optical properties was maintained using a magnetic stirrer at all times.

2.2.3.2 Calibration Results

As described earlier (see Eq. 2.6), the calculation of k_1 and k_2 can be achieved by measuring one set of optical properties using both ISS and LRS systems. However, for a robust estimate, k_1 and k_2 were calculated at various oxygenation levels using a dynamic oxygen saturation phantom described above. Table 2.1 shows the values of k_1 and k_2 obtained at various time points of a dynamic phantom, each corresponding to a different oxygenation level. Since the de-oxygenation and re-oxygenation were rapid and did not have a well-defined time constant, the saturation readings are spaced randomly. As can be observed from Table 2.1, the calculated calibration coefficients are stable across a wide oxygenation range with standard deviation of less than 2% about mean. Figure 2.3(a) shows one of the measured set of measured $R_p(\lambda)$, $\mu_a(\lambda)$, and $\mu_s'(\lambda)$ and the linear regression line for probe with k_1 being the y-intercept and k_2 being the slope. While the inverse calculations for an unknown sample will be described in the next sub-section, an illustration of the measured and fitted reflectance is shown in Fig. 2.3(b). The accuracy of parameters k_1 and k_2 critically affects the 'goodness of fit' in the

inverse calculations, and thus influences the accuracy of measured optical properties of tissues under interrogation.

Table 2.1 Calculated values of k_1 and k_2 at different oxygenation levels of a blood-intralipid-yeast phantom. Blue numbers represent data acquired during de-oxygenation and red numbers represent data acquired using re-oxygenation.

% Sat	66	56	50	45	38	31	25	42	47	55	57	64	71	83	Mean (SD)
K_1	9.89	9.89	9.92	9.95	9.97	9.99	10.04	10.04	10.03	10.02	9.97	9.90	9.89	9.84	9.95 (0.07)
K_2	2.73	2.78	2.8	2.77	2.76	2.73	2.73	2.79	2.74	2.71	2.75	2.89	2.81	2.85	2.77 (0.05)

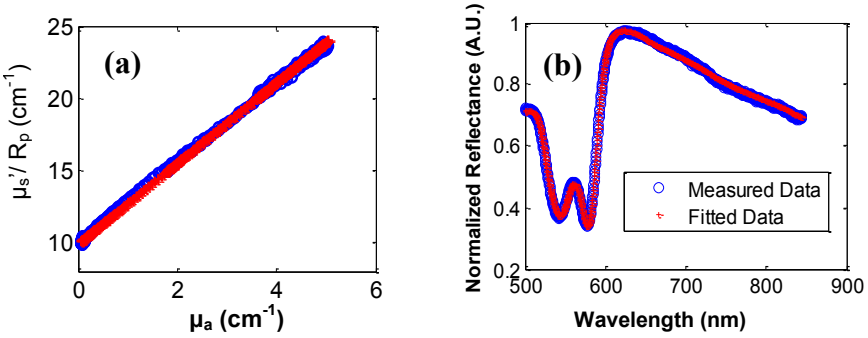

Figure 2.3 Linear fit with a least-squares regression line to determine values of k_1 and k_2. (a) A linear fit to the measured data using a phantom of total hemoglobin ([HbT]) = 45 μM and μ_s'(750nm) = 11.2 cm^{-1}, giving rise to k_1= 9.89 cm^{-1} and k_2 = 2.81. (b) Spectra predicted (red) by the model and measured (blue) using a tissue phantom of [HbT] = 34 μM and μ_s'(750 nm)=8.31 cm^{-1}.

2.2.3.3 A note on white sample measurement

It is noteworthy to point out that k_1 and k_2 depend highly on the white sample measurement for eliminating instrumentation effects on the measured spectrum of the sample under examination. Incorrect measurement of the white sample will lead to serious errors for the fitted parameters, i.e., [Hb], [HbO], *a* and *b* in Eqs. (2.2, 2.5).

White sample measurement can vary with the following parameters: distance between the fiber tip and sample surface; integration time; or light source intensity. Measuring different types of tissues may require a different integration times for the detector. Fig 2.4 shows the typical measurement geometry for the white sample. Since each reflectance curve needs to be

divided by a reference curve from the white sample, care should be taken to standardize the procedure. This can be done either by fixing the distance between the fiber and the white sample (Fig. 2.4) and collecting reflectance reading at various integration times to create a look-up table, or by linearly scaling the white sample reflectance curve to match the integrations time to the measured tissue reflectance spectrum. The latter method is based on our observation that the relationship between reflectance spectra and integration times is approximately linear. In my dissertation research, I use the latter method.

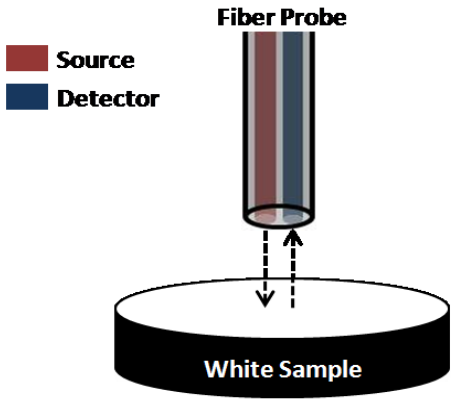

Fig 2.4 Illustration of geometry for white sample measurement: the optical fiber is placed on top of the pure reflectance sample (white sample), and the distance from surface is adjusted based on the integration time of the spectrometer. The distance should be chosen to have a relatively uniform filed of illumination under the probe area.

2.2.4 Inverse calculation

The inverse calculation of Eq. (1) deals with determination of tissue chromophore concentrations and effective scattering coefficients from the measurements of LRS taken on the tissue surface. The mathematical problem of inversion can be practically solved by an approach of function minimization using an optimization algorithm. The algorithm searches for an optimal set of values, as represented by $\boldsymbol{x}$ = ([Hb], [HbO], a_{factor}, b), from the given multi-parameter space that best match the measured $R_p(\lambda)$ using the least- squares analysis. Here, a_{factor} represents the scaling term for the parameter 'a', in Eq. (2.5). Notice that a scaling term is used instead of using 'a' as a fitting parameter, given the large magnitude of a (2.54×10^9, for 10%

intralipid) which can lead to an unbalanced solution space. The function minimization problem can be mathematically expressed as follows:

$$f(x) = \sum_{i=1}^{M} \left[R_p(\lambda_i)^{(measured)} - R_p(\lambda_i)^{(predicted)} \right]^2, \quad (2.7)$$

where $f(\boldsymbol{x})$ represents an objective function and needs to be minimized by finding an optimal set of the parameters, $\boldsymbol{x}_{opt}$, M is the number of wavelengths, $R_p(\lambda_i)^{(measured)}$ and $R_p(\lambda_i)^{(predicted)}$ are the reflectance values (at wavelength λ_i) measured by the optical probe and predicted by Eqs. (2.1) - (2.5), respectively, with the parameter set, $\boldsymbol{x}$, to be optimized.

Evolutionary algorithms are widely utilized in the field of optimization [41-43]. The algorithms work on a population of values rather an initial guess, making the solution independent of an initial guess. Their inherent characteristics make them suitable to search for a global minimum, rather than being stuck in local minima. The ant colony optimization (ACO) algorithm, introduced by M. Dorigo [44], is a probabilistic evolutionary technique for solving computational problems. This basic technique was modified to suit function minimization for this study, by a previous PhD student, Dheerendra Kashyap [35]. Since ACO requires the bounds to be set for the fitting parameters, it allows the algorithm to search for the global minimum only within the bounds. It is important to make sure that the global minimum is within these bounds. A detailed explanation of this phenomenon can be found in Section 2.3.2.1.

Equation (2.1) is very non-linear and spans a wavelength range of 500 nm to 850 nm. In order to obtain optimal fit between the measured and calculated reflectance curve, I incorporated a multiple-step sequence; within each step the objective function for minimization, Eq. (2.7), was selected somewhat differently. First, the entire spectrum (500 nm – 850 nm) was utilized for fitting, and the fitted values of [Hb], [HbO], a_{factor} and b in Eq. (2.5) were obtained. Second, the $\mu_s(\lambda)$ parameters (i.e., a_{factor} and b) were further re-fitted with $\pm$15% bounds around the values found in step one; in this step, a smaller spectral region of 520-590 nm that has a strong hemoglobin absorption band was selected for re-fitting to improve 'goodness of fit' for

[Hb] and [HbO]. Third, after refining the fitted parameters of [Hb] and [HbO], they were re- fitted within ±20% bounds around the values found in step two while $\mu_s(\lambda)$ values (or *a* and *b)* were also refitted without the ±15% bounds refinement. In the third (last) step, the entire spectrum (500-850 nm) was utilized, leading to the finally optimized values of $\boldsymbol{x_{opt}}$ ($[Hb]_{opt}$, $[HbO]_{opt}$, $a_{factor\text{-}opt}$ and b_{opt}). Overall, three fitting steps with changing parameter bounds and spectral regions were utilized in order to obtain an optimal fit for scattering and absorption parameters. An example to show comparison between the measured and fitted reflectance for blood-intralipid phantom is already given in Fig. 2.3(b). It is possible to add additional absorbers to the problem, as will be seen in following chapters, when measurements are made on tissues instead of phantoms. Additionally, in certain cases, it is reasonable to assume that scattering parameter 'b' is a constant, and fit only for 'a_{factor}' to obtain 'μ_s'. Further discussion on the bounds selection and robustness of the algorithm are presented in Section 2.3.1.

2.3 Testing and Validation

2.3.1 Validation of LRS method on tissue phantoms

In order to validate the algorithm for absolute quantification, I created dynamic tissue phantoms (explained in Section 2.2.3.1) and performed the measurements with both LRS system and a tissue oximeter (ISS Oximeter), which was used as a gold standard device for comparison. Figure 2.5(a) shows comparisons between the values obtained from ISS tissue oximeter and those quantified with the algorithm, when a change in oxygen saturation (O_2 Sat) was achieved by adding yeast to the liquid phantom. The measurements were made at 12 different time points in the O_2 Sat range of ~20%-80% during the oxygenation and deoxygenation process, as described previously in Section 2.2.3.1. It is clear from Fig. 2.5(a) that oxygen saturation(O_2 Sat) values measured by both modalities are very consistant in the O_2 Sat range of 20%-80%. The absolute errors were also calculated at each data point (n=12) and are plotted in Fig. 2.5(b): average absolute errors for O_2 Sat, [Hb] and [HbO], along with standard error of mean (SEM), were 3.0±0.7 %, 0.9±0.2 μM, and 0.9±0.2 μM, respectively.

Similar experiments were repeated several times, and the results were very similar to those seen in Figs. 2.5(a) and 2.5(b).

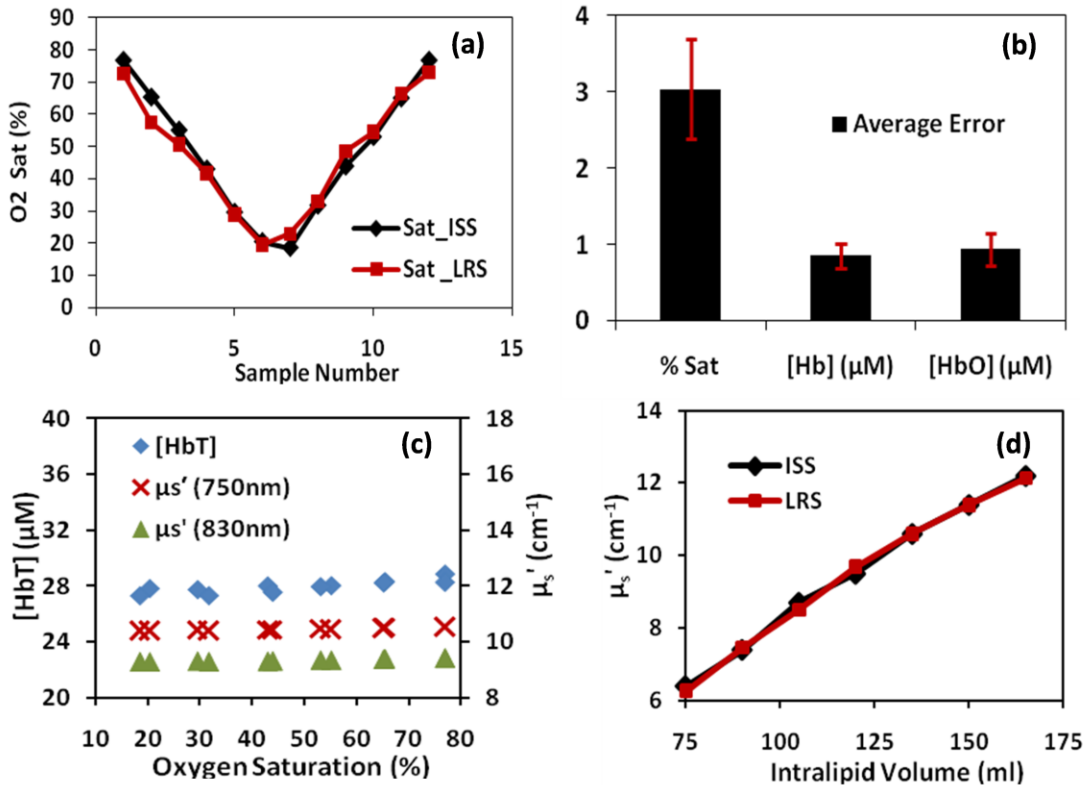

Fig. 2.5 Comparison of parameters quantified from the LRS system and ISS oximeter: (a) oxygen saturation values obtained from ISS oximeter (black) and LRS system (red). (b) Average absolute errors in three calculated parameters of O_2 Sat (3.0±0.7%), [Hb] (0.9±0.2 μM) and [HbO] (0.9±0.2 μM), with respect to those given by ISS oximeter. The error bars indicate standard error of mean. (c) Changes in [HbT] and μ_s' (at 750 nm and 830 nm) observed during the cycle of oxygen saturation, as shown in (a). (d) Comparison of μ_s' calculated at 830 nm using ISS oximeter (black) and LRS system (red).

The reasons for limiting the comparison in the O_2 Sat range of 20% - 80% are as follows: (1) The ISS oximeter being used as a gold standard device in this study is a tissue oxygen saturation monitoring apparatus that is known to work well in the chosen physiological range [45,46]. The errors in measurement beyond this range tend to increase, contingent upon one of the parameters (either [HbO] or [Hb]) approaching zero under either 100% or 0% hemogobin oxygen saturation. (2) Optical measurements through fiber probes interrogate a 3-dimensional volume with a banana pattern. The interrogated tissue volume in general includes both blood-

perfused vessels and bloodless tissue background. The mixture of these two components will create a partial volume effect, leading to an averaged O_2 Sat value lower than a regular arterial O_2 Sat, and most likely to be in the region around 80% or lower. (3) It is almost physiologically impossible to have any value of O_2 Sat lower than 20%. Therefore, it is reasonable to select the range of vascular O_2 Sat to be 20-80% used for algorithm validation.

The reliability of the LRS device was also evaluated by comparing the changes in total hemoglobin concentration, [HbT], and μ_s' for each set of the above measurement. Since yeast does not induce much change in either [HbT] or μ_s', these two parameters should ideally remain constant when the oxygenation state is altered. Figure 2.5(c) shows the measured values of [HbT] and μ_s' (at 750 nm and 830 nm) with changing O_2 Sat. As expected, those values are found to be constant across the saturation range of 20-80% with small SEMs as [HbT] = 28.0 ±0.4 μM, μ_s' (750 nm) = 10.46±0.05 cm^{-1}, and μ_s' (830 nm) = 9.34±0.04 cm^{-1}.

Another set of experiments were conducted to test the consistency of μ_s' when Intralipid volume was varied from 75 ml to 170 ml within the given liquid phantom volume. Figure 2.5(d) shows a comparison of values obtained by the ISS oximeter and LRS system at 830 nm. The mean difference (with standard deviation) between the scattering values obtained by two methods was calculated to be 0.02±0.13 cm^{-1}, demonstrating almost perfect match between the outcome of two methods.

2.3.2 Algorithm Testing

In this section, I will evaluate two practical aspects of a data fitting and optimization algorithm. First, I will address the effects of changing bounds of individual fitting parameters on the final outcome of the optimization algorithm. Second, I will compare the three-step fitting routine described here, versus single-step fitting routine, to highlight the significance of using three-step process.

2.3.2.1 Effects of different bounds on optimization outcome

As stated above, the ant colony optimization (ACO) requires upper and lower bounds to be given for each variable implicitly used in Eq. (2.7) when we search for the optimal set of absolute values of [HbO], [Hb], a_{factor}, and b, where a_{factor}, and b account for μ_s' seen in Eqs. (2.4) and (2.5). ACO allows the algorithm to arrive at the global minimum only within the given bounds. While the bounds that I use in my data analysis are reasonable based on the tissue of interest, the final outcome of fitted parameters of $\boldsymbol{x}_{opt}$ are in theory affected by the selected bounds. It is therefore important to examine whether the global minimum for Eq. (2.7) exists outside the selected bounds or how much the fitted results depend on the selection of different bounds. To answer these questions, I investigated if expanding the bounds would affect the results. Specifically, I chose three different ranges of bounds for all four parameters of [HbO], [Hb], a_{factor}, and b as follows: (1) the *original* set of bounds that were used in the current data analysis presented in Section 2.3.1, (2) a *modified* set of bounds broader than the original set, (3) and an *infinite* set of bounds that represent the values much beyond their physiologically possible limits.

The normal levels of hemoglobin concentrations in pure blood are up to 10.7 mM in human adults[47]; in general NIRS measures vascular hemoglobin concentrations in tissue vasculature, which are much lower than those in pure blood[48]. For comparison, the three regions of bounds for both [HbO] and [Hb] are tabulated in Table 2.2. It is also well known that the range of μ_s' values for biological tissues is from 1-40 cm^{-1}, and might extend up to 200 cm^{-1} under extreme conditions in a highly light-scattering medium, such as white matter in brain tissues. I also included three regions of bounds for μ_s', a_{factor} and b in Table 2.2, where a = (2.54 X 10^9)/a_{factor} and b are associated with μ_s' through Eqs. (2.3) - (2.5).

As seen in Section 2.2.2, Eq. (2.1) is coupled with Eqs. (2.2) - (2.5) and is very non-linear with a broad spectral span from 500 nm to 850 nm. In order to obtain an optimal fit between the measured and calculated reflectance curve, I have incorporated a three-step fitting sequence. Each of the three bounds (for all fitting parameters) listed in Table 2.2 was initially

set as broad bounds for step-1 fitting routine; the fitting bounds for step-2 and step-3 sequence were determined according to the fitting outputs in step-1, as explained in Section 2.2.4. The criteria to stop the fitting iterations at each step were defined either by a chosen number for maximum iterations or when a desired value of the objective function (i.e., eq. (2.7)) was achieved. I evaluated the fitting efficiency by comparing three output parameters by the end of fitting routine: (1) the number of total iterations ($n_{iteration}$), (2) the actual value of the objective function (v_{obj}), and (3) final fitted [HbO] values. The numbers of minimum and maximum iterations were chosen to be 20 and 50 during step-1 fitting, 20 and 300 for step-2 and step-3. The criterion value of v_{obj} to end the iterations was chosen to be 2, 0.01, and 0.05 during the three steps of fitting, respectively.

Table 2.2. Three sets of parameter bounds that are chosen to study their effects on the performance of fitting routine

	[Hb], [HbO] (mM)		$a_{factor} = 2.54\times10^9/a$		b		$\mu_s' = a\lambda^{-b}$ (cm^{-1}) (λ=750 nm)	
	upper bound	lower bound	upper bound	lower bound	upper bound	lower bound	upper bound	lower bound
Original	0.9	0.0001	1000	0.01	2.6	2.3	1.8×10^4	2.5×10^{-2}
Modified	3	0.0001	1000	0.1	3.0	1.7	9.8×10^4	1.8×10^{-3}
Infinite	20	0.0001	100000	0.01	10	0.1	3.9×10^{10}	1.3×10^{-25}

It was found that by increasing the bounds, the number of iterations increased significantly, as illustrated in Table 2.3, which was created using one of the data points shown in Fig. 2.5(a) as an example. Five more data points with different O_2 Sat values were also utilized for fitting-routine testing; the results obtained were similar to results listed in Table 2.3. It is also clear from this Table 2.3 that the number of iterations increases significantly when the bounds become broader, from the original bounds to the modified bounds and then to the infinite bounds. The actual objective function values obtained when the fitting was complete were often correspondingly higher in most cases using either modified or infinite bounds than the original bounds.

Table 2.3. A comparison of number of iterations, $n_{iteration,}$ and value of the objective function, v_{obj}, for a specific O_2 Sat data point using three different bounds

	Fitting step 1		Fitting step 2		Fitting step 3	
	$n_{iteration}$	v_{obj}	$n_{iteration}$	v_{obj}	$n_{iteration}$	v_{obj}
Original bound set	21	0.11	21	0.001	21	0.046
Modified bound set	86	0.94	300	0.015	22	0.050
Infinite bound set	300	8.01	300	0.147	300	0.153

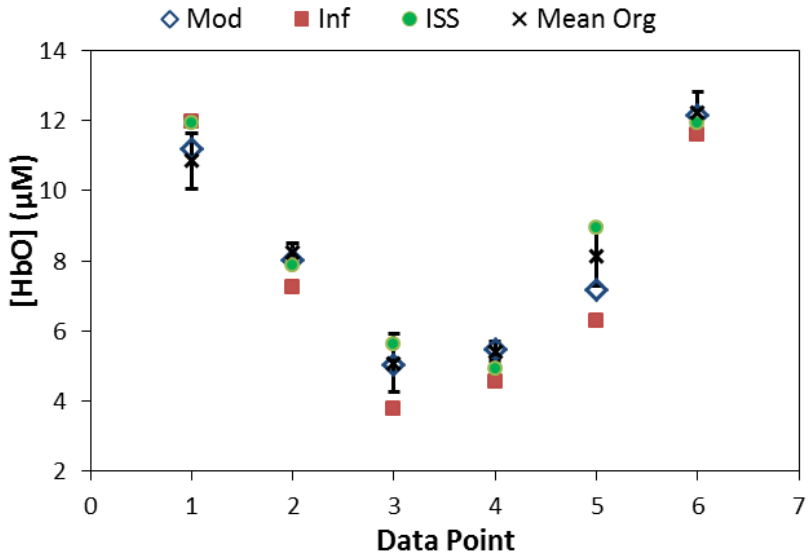

Fig 2.6. Comparison of fitted [HbO] values obtained using three different bounds with the expected values (solid circles) given by ISS oximeter. The six data points were taken from the phantom study presented in Fig. 2.5(a). Here, 'Mod' represents the case with modified bounds, 'Inf' represents the case with infinite bounds, 'ISS' represents the expected values determined by ISS oximeter, and 'Mean Org' represents mean values obtained after 15 fitting-routine runs with original bounds; error bars mark the respective standard deviations.

Furthermore, to directly compare the results with different bounds, a set of fitted [HbO] values are shown in Fig. 2.6 using 6 different O_2 Sat values. This figure shows [HbO] values obtained using all three fitting bounds, plotted along with the expected values determined by the standard ISS oximeter. The fitted results may vary somewhat each time when the fitting routine

runs due to the nature of least squares fitting. I executed the 3-step fitting routine 15 times using the original bounds to create a mean fitted value of [HbO] with standard deviation, as represented by the black vertical bars in Fig. 2.6. The results shown in this figure confirm that the fitted [HbO] values are in good agreement with the expected ones when either original or modified bounds were used. The infinite bounds are still able to provide us with reasonable fitted parameters with a certain degree of under-estimation, as seen in the figure, where the fitted results lie slightly below the range of mean fitted [HbO] values obtained by either the original or modified bounds.

Overall, this part of study demonstrates that the 3-step fitting sequence based on ACO in my earlier fitting routine with physiologically determined bounds should be robust to create reliable results. Selections of different upper and lower bounds have insignificant effects on the final output of fitted parameters, which establishes this implementation of ACO as a global optimization routine in a true sense.

2.3.2.2 Comparison of three-step fitting with single-step fitting

My optimization algorithm is designed to vary wavelength ranges when executing the 3-step fitting sequence: in step 1, 500-850 nm was used with bounds as given in Table A1; in step 2, the wavelength range was narrowed down to 520-590 nm with restricted scattering bounds (±15% variation around the fitted *a* and *b* parameters); in step 3, the spectral range returned to 500-850 nm with restriction in [Hb] and [HbO] bounds (±20% variation around the fitted values of [Hb] and [HbO] given in step 2) but without restriction in scattering bounds (i.e., having the same bounds for a_{factor} and *b* as the ones used in step 1). Next, I compare and evaluate the difference in optimization outcome between 3-step fitting and 1-step fitting in the wavelength range of 500-850 nm.

Single-step fitting routine was utilized to fit the same data set as those in Section 2.3.2.1, with the same bounds listed in Table 2.2. The maximum number of iterations was set to 600, and the minimum objective function value, v_{obj}, was set to be 0.05, as in case of 3-step

fitting. It was found that the objective function could not converge to the preset v_{obj} within 600 iterations for all three kinds of bounds. In the case of using infinite bounds, the results were not usable since the output values of objective function were as high as (up to) 7. When the original and modified bounds were employed, the objective function values were around 0.1, but the [HbO] values were overestimated in most cases. Careful inspection on the fitted curves in the wavelength region of 500-600 nm revealed that the fitting was not adequate in that range, although the overall objective function values were relatively low.

To summarize, in this implemention, 1-step fitting is not satisfactory or adequate, particularly with infinite bounds. The accuracies of fitting parameters are improved gradually as 3-step fittings are performed: step-1 fitting routine results in a set of parameters close to the expected set in the overall spectral range, but not good enough as the final output. Step-2 fitting provides us with more accurate values of [HbO] and [Hb] based on 500-600 nm spectra. Step-3 refines the fitting in the overall wavelength region again (500-850 nm) and outputs the best set of fitting parameters.

One way to improve the accuracy of 1-step fitting may be weighted-fitting with more weight in the 500-600 nm range. The results of this study indicate that with the current fitting method, a good set of fitting parameters can be more accurately and quickly achieved with prior knowledge on the physiological bounds of the measurement. With tighter and narrower bounds, the speed and accuracy of the fitting algorithm increases. Also, computational cost or speed may be improved if parameter *b* is assumed to be constant (b = 2.4), as previously determined for intralipid[38], reducing a major dimension in the solution space.

2.4 Summary and Discussion

In this chapter, I developed and evaluated a quantification method that can be used to determine tissue optical properties based on LRS with the use of small S-D separation fiber probes. The quantification approach originates from Zonio's reflectance model [23] for absolute calculation of [Hb], [HbO], and μ_s'. This method utilizes the wavelength range of 500-850 nm

and obtains the absolute values of [Hb], [HbO], and μ_s' by least-squares regression using a multi-step sequence, optimization approach. This method was evaluated by comparison with a commercial oximeter (ISS, inc.) by performing laboratory experiments on homogenous liquid-tissue phantoms, both static and dynamic, and the results were found to be in close agreement with chosen gold standard. A systematic calibration procedure for finding the system parameters, k_1 and k_2, is also described.

Previously published studies[29,34,49] utilized the same reflectance model but a different mathematical expression (i.e., a linear function) for the spectral dependence of light scattering[23] when investigating skin properties. My observation is that if adequate bounds are applied for the optimization function, similar results of fitted [Hb], [HbO], and μ_s' could be obtained using either a linear or Mie function for light scattering pattern. However, the goodness of fit in that case is best governed by the true scattering profile of the tissue under investigation.

In general, the volumes measured by ISS and LRS are not necessarily comparable, depending on the places where the probes are placed. The ISS probe measures the optical properties of the medium 1-2 cm below the sources and detectors which are usually separated ranging from 2.0 cm to 3.5 cm. The LRS probes usually have a S-D separation of several hundred microns and thus sense the optical properties 0.5-1.5 mm right beneath the probe tip. Since the tissue phantom was constructed using homogenous intralipid solution mixed with blood, and continuously stirred through the measurement, the phantom to be measured by both ISS and LRS was completely uniform throughout the container. Thus, the optical properties of the phantom would not vary when being measured in different interrogation volumes; the results obtained from both modalities are comparable and appropriate, as shown in Fig. 2.5(a).

It seems intuitive that standard deviation would be a valuable parameter to compare the results from both modalities, i.e., ISS and LRS. In the case for Fig. 2.5, however, standard deviation could not be obtained for Figs. 2.5(a) and 2.5(c) because these readings were single point measurements as explained below. The blood de-oxygenation (controlled by yeast) and

re-oxygenation (controlled by oxygen bubbling) processes were dynamically varied, i.e., the values of optical properties under study were changing as a function of time. Only one simultaneous reading could be taken at one specific oxygenation level during de-oxygenation or re-oxygenation process. Similar experiments were repeated several times, but each time it was impossible to take the readings at the exact oxygen saturation level, O_2 Sat (%). Instead, the average errors between the two modalities could be quantified by collectively taking into account all the readings at different levels of O_2 Sat (%), along with the standard error of mean (SEM) plotted for each parameter in Fig. 2.5(b).

The absolute quantification method of evaluating LRS provides insight into structural and functional changes happening inside the tissue and can be applied to various clinical applications, such as for cancer diagnosis[50] and neurosurgery guidance[19] as well as perhaps for neuro-functional monitoring, as demonstrated by application of this technique, published in Neuroimage[51]. In my dissertation, I applied this method for cancer diagnosis, both in animal models and in human tissue, as will be described in Chapters 4-6. In the next Chapter 3, I will describe the second technique/modality that I used in addendum to LRS to strengthen the diagnostic ability.

CHAPTER 3

METHOD II: AUTO-FLUORESCENCE LIFETIME SPECTROSCOPY

3.1 Introduction

Fluorescence has been widely utilized in biological sciences including biochemistry and biophysics among other disciplines, since its discovery in later part of the 19th century. In biological tissues, there are various chemical compounds that re-emit light after excitation with light. These chemical compounds are called fluorophores, a lot of which have been studied extensively. Auto-fluorescence is simply a term used for fluorescence originating from endogenous fluorophores (i.e., those which are intrinsic to the biological tissue, as opposed to injectable contrast agents), which include extracellular structural proteins like collagen and elastin, as well as components of intracellular metabolism like NADH, flavins, porphyrins, lipopigments among others [27,52]. Among a plethora of biological applications of fluorescence, fluorescence spectroscopy and fluorescence lifetime measurements have also been studied by various researchers for application to tissue differentiation in various pathological conditions including cancer diagnosis in clinical as well as pre-clinical setting[26,53-60]. Fluorescence spectroscopy is relatively simpler, and involves measuring the emission spectrum followed by a specific photo-excitation, whereas fluorescence lifetime measurement involves measuring time-resolved fluorescence in nanosecond time range, using ultrafast sophisticated hardware systems. Fluorescence spectroscopy although a sensitive technique, has a few limitations like high false positive rates as well as lack of its ability to discern various fluorophores due to overlap in their emission spectra [27]. Fluorescence lifetime, on the other hand, can provide improved fluorophores specificity, and has a potential to assess local environment through changed in radioactive and non-radioactive decay constants[27]. Overall, time resolved measurements are richer in information than the steady-state measurements[61].

As mentioned above, fluorescence techniques have been applied to various cancer types. Specifically, fluorescence lifetime has been applied to differentiate cancerous tissue from healthy tissue in breast tissues[58], colon[62], and brain [63], and other human and animal biological tissues[27,64]. However, application of fluorescence spectroscopy to prostate tissue has been limited[15], with no publications exploring use fluorescence lifetime as an endogenous contrast.

Given the promising nature of the technique which provides a contrast that is complementary in nature to that of LRS described in Chapter 2, auto-fluorescence lifetime spectroscopy (AFLS) was chosen as the second modality to enhance prostate cancer detection. In this chapter, initially I will briefly explain the principles of fluorescence, and time-domain measurements using a time correlated single photon counting (TCSPC) system, then describe the design of the custom-built (ISS Inc., IL, USA) fluorescence lifetime system that is employed for this study, and finally describe the analysis algorithms, followed by testing and validation of the device.

3.2 Theory and Principles

3.2.1. Fluorescence

Incandescence and luminescence are two ways in which light can be observed from an object. While incandescence refers to light produced as a result of high temperatures (for example, Sun, electric bulb), luminescence refers to 'cold light' that can be emitted at lower/regular temperatures. In the latter case, a source of energy excites an electron to move to higher energy levels, and during relaxation process, light energy is produced based on the energy gap between the excited and ground states. Luminescence can be of various types, based on the source of excitation, namely, bioluminescence (eg. firefly), electroluminescence (LCD screen), photoluminescence, etc. Fluorescence is a subtype of photoluminescence, which is a luminescence arising from direct photoexcitation of emitting species. Fluorescence, by current definition, is "spontaneous emission of radiation (luminescence) from an excited

molecular entity with retention of spin multiplicity"[65]. There are other types of photoluminescence like phosphorescence, which are out of scope for present study.

The first observarrtion of fluorescence phenomenon was published by J.F.W. Herschel in 1845, using quinine solution. However, the term "Fluorescence" was coined by G.G. Stokes in his paper "On the change of Refrangibility of light", in 1852[66], after he observed blue emission from quinine solution that was irradiated using ultraviolet (UV) light.

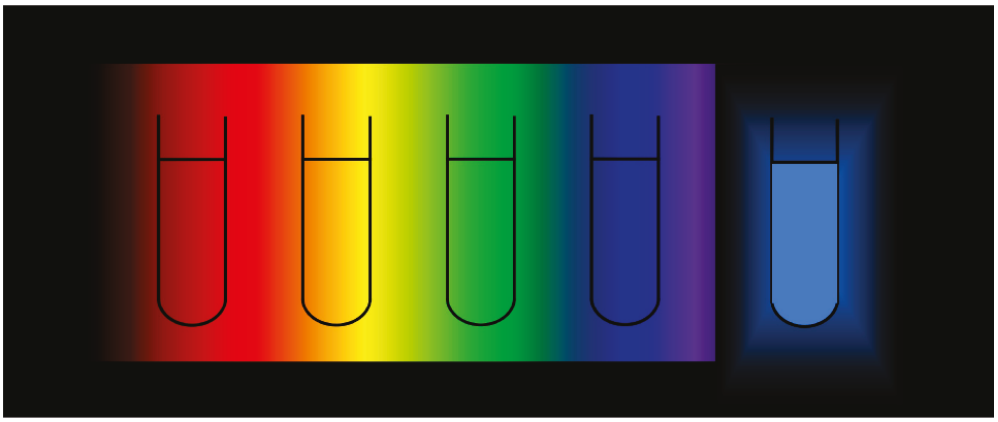

Fig 3.1 An illustration of Stokes's experiment, showing no effect on the solution of quinine when irradiated by the visible spectrum, but emission of blue light when irradiated with UV light[67].

Fluorescence phenomenon is best explained by the use of a Jabloknski energy diagram, a typical form of which is represented in Fig. 3.2. In the figure, S_0,S_1, and S_2 represent the ground, forst and second singlet states, respectively. Whithin each state, a number of vibrational levels can exists, depicted by 0,1 and 2 in S_0. Once a fluorophores is excited with appropriate energy photons, the electrons in the singlet ground state jump to a higher state (S_1, S_2) in a time scale of about 10^{-15} seconds. There is internal conversion followed by absorption, in a time frame of about 10^{-12} sec, during which in most cases the electron relaxes to the lowest vibrational level of S_1. Finally, when the electron relaxes to the ground state, which happens in nanosecond range (~10^{-8} sec), it emits a photon with an energy less than the incident energy, i.e. a higher wavelength photon. When the photon relaxes to the ground state, it may return to a higher vibrational level, and then reach thermal equilibrium. Relaxation to higher vibrational

states also causes a spread in the emission spectrum, which is usually a mirror image of the excitation spectrum.

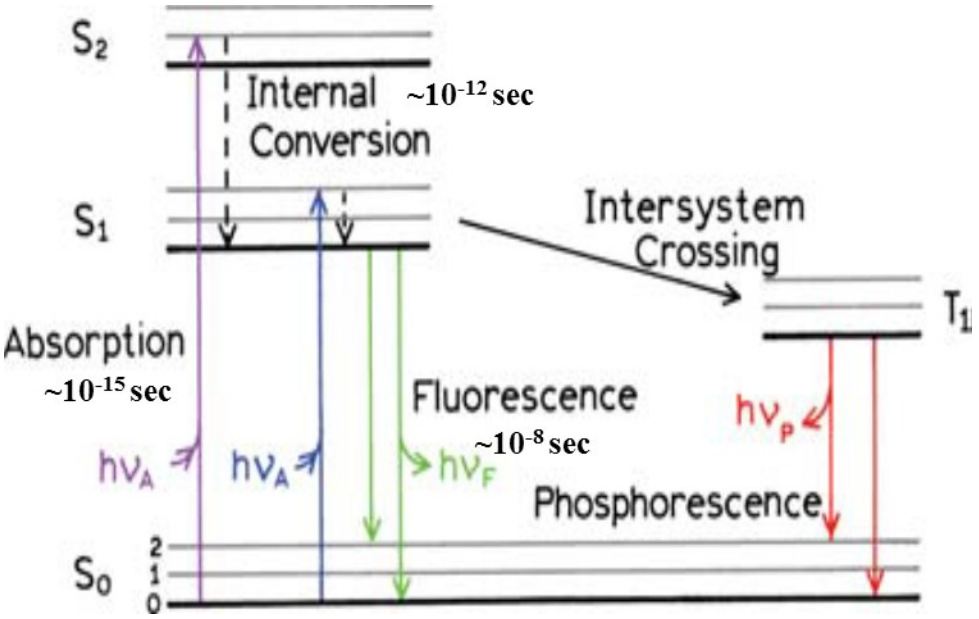

Fig. 3.2. A form of Jablonski diagram, illustrating the phenomenon of fluorescence and phosphorescence. The diagram has been modified from reference[61].

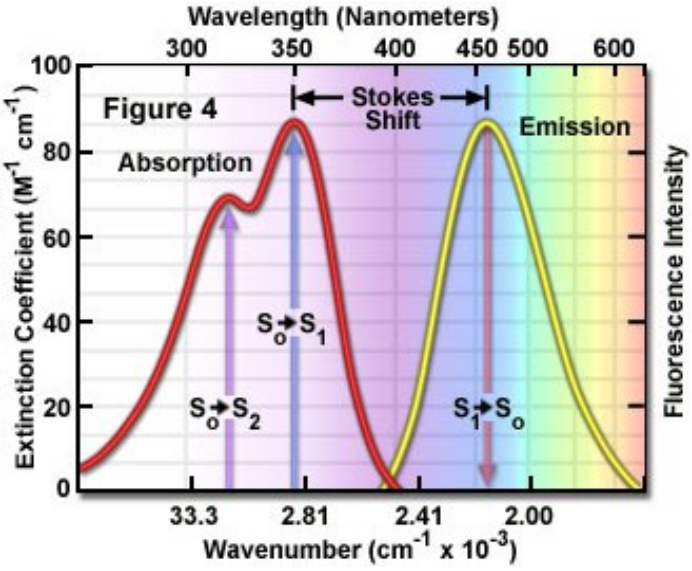

Fig. 3.3 Excitation-emission spectra of Quinine (Image Source: http://www.olympusconfocal.com/theory/fluoroexciteemit.html).

A typical excitation-emission spectrum for quinine is shown in Fig 3.3. There is a lack of symmetry in absorption and emission spectra, in this case, as the singlet state S_2 is involved too. Since the fluorescence emission results only after internal conversion, i.e. after relaxation to singlet state S_1, the emission spectrum is always a mirror image of the absorption spectra for first singlet state only[68]. The difference in the excitation and emission energies is so-called stokes shift as this phenomenon was first observed by Sir G.G. Stokes [66].

3.2.2 Fluorescence lifetime

As mentioned earlier (Fig. 3.2), the fluorescence phenomena takes place at a time scale of nanoseconds, typically in 10^{-7} to 10^{-9} sec. If rather than a single molecule, a bulk of fluorophore substance is excited, the fluorescence emission is rather a stochastic process, with a decay of fluorescence emission intensity as a function of time. Also, not all the electrons that are excited follow the radiative decay, i.e. some also follow non radiative decay to the ground state. This difference also defines the quantum efficiency of a fluorophore:

$$Q = \frac{\Gamma_r}{\Gamma_r + \Gamma_{nr}} \tag{3.1}$$

Where, Q is the quantum efficiency, Γ_r is the emissive rate of fluorophore, and Γ_{nr} is the rate of non-radiative decay. The total decay rate is given by defined by the sum of radiative and non radiative decay rates, i.e., $\Gamma + \Gamma_{nr}$. Thus, for an initial population (n_o) of fluorophores, the decay can be expressed as,

$$\frac{dn(t)}{dt} = (\Gamma_r + \Gamma_{nr})n(t) \tag{3.2}$$

Where, n(t) represents number of excited fluorophores at a given time instant t. Solving Eq. (3.2) results in first order kinetics describing the exponential decay of excited population, given as: $n(t) = n_o exp(-t/\tau)$; where τ is the lifetime of the decay [$\tau = (\Gamma + \Gamma_{nr})^{-1}$]. Since n(t) is directly proportional to the intensity, I(t), the above expression can also be written as:

$$I(t) = I_0 \exp(-t/\tau) \tag{3.3}$$

As seen in Eq. (3.3), fluorescence decay for a fluorophore is typically described by a single exponential. However, in case of multiple fluorophores, more complex models can be used, which will be addressed later in section 3.3. Fluorescence lifetime is a representative of average time spent by a fluorophore in the excited state, and is a very important characteristic of a fluorophore, as it is a function of the environment in which the fluorophore resides.

However, given the timescale of the process, measuring fluorescence lifetime is not trivial. Next section will describe one of the most robust methods available for lifetime measurement, that is, time correlated single photon counting (TCSPC).

3.3 Instrument Design and Description

3.3.1 Time-domain fluorescence measurement using TCSPC

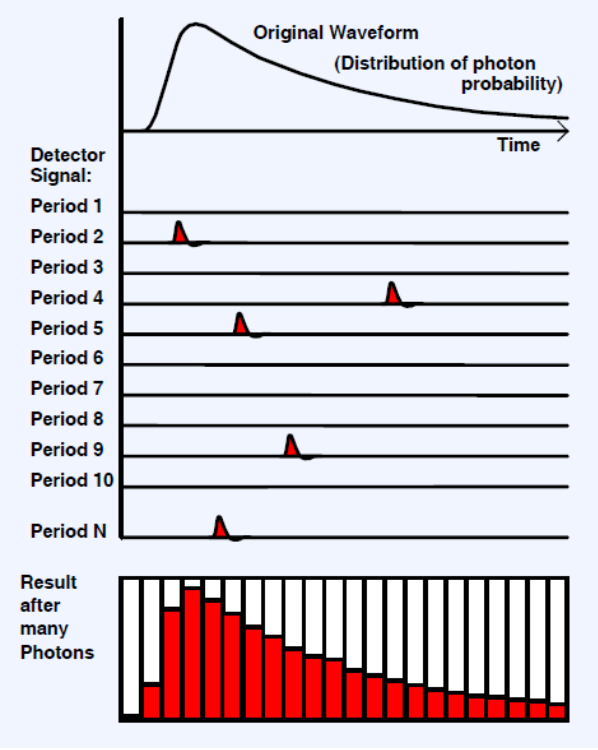

Fig. 3.4. Illustration of principle of TCSPC (Image source: TCSPC Handbook, 4th Ed. Becker and Hickl GmbH)

The principle of TCSPC is illustrated in Fig. 3.4. TCSPC detection involves measurement of timing of a single photon upon excitation by very narrow pulse of light. Typically, the system is configured such that less than one photon per laser pulse is emitted, and as a result there are many empty periods. Each arriving photon is stored into a memory location corresponding to its arrival time. As seen in 3.4, after many photons, a histogram based on the arrival times is constructed, which represents the lifetime of the fluorophore. The total acquisition time is determined by the concentration and quantum efficiency of the fluorophore, the power of the excitation source, and the desired signal to noise ratio.

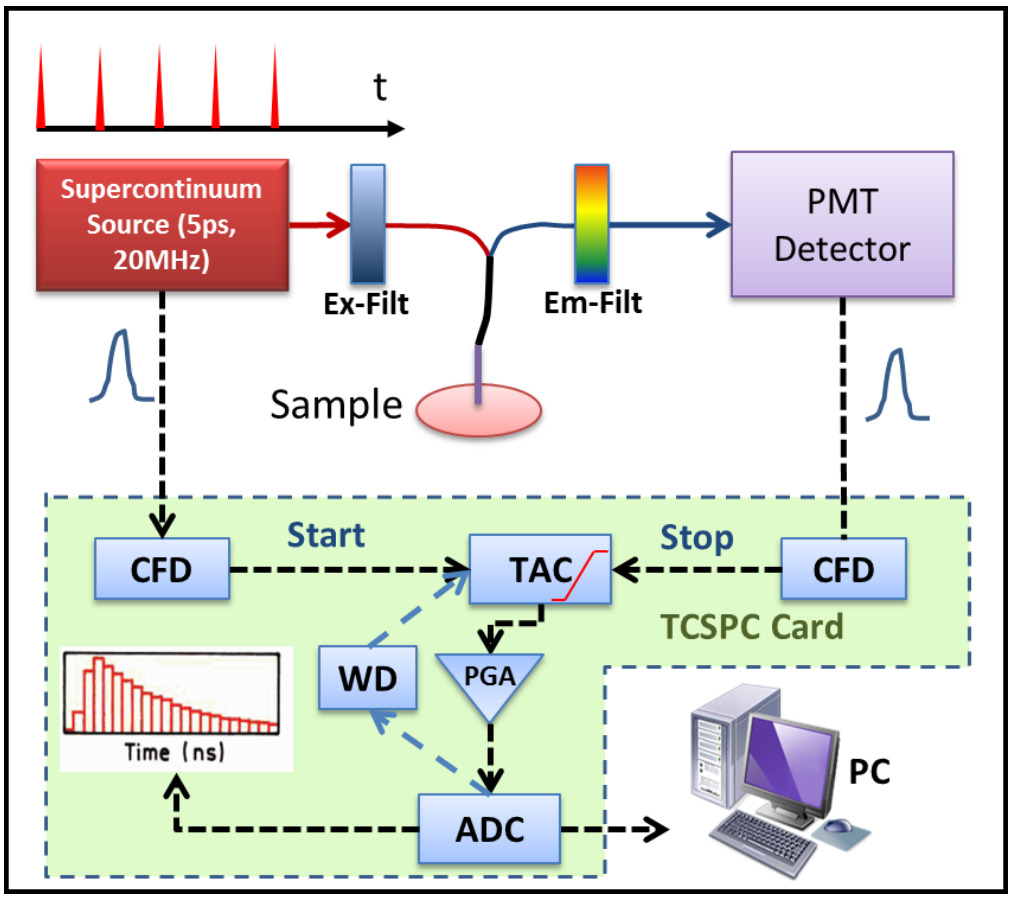

Fig. 3.5. A simplified block diagram representation of the TCSPC based lifetime system employed in this study.

3.3.2. System components and description

A block diagram of the TCSPC system is shown in Fig. 3.5. This system was custom built by ISS, Inc. (ISS Inc., Champaign, IL, USA) to do measurements with an optical fiber probe in reflectance geometry. The system essentially consists of a picosecond pulsed supercontinuum laser source (SC - 450, Fianium Inc., Eugene, Oregon) , with a 5 picosecond (ps) pulse width and a broadband spectrum (~ 440 nm - 2 μm) at a repetition rate of 20 MHz. The laser is coupled to an excitation chamber, which contains a 5-slot filter wheel with excitation filters. The excitation beam is passed through the desired excitation filter, and coupled though a variable neutral density (ND) filter into the excitation channel of a multi-furcated fiber optic probe using an SMA connector and a collimator. The resulting fluorescence is collected through emission channel of the multi-furcated fiber optic probe and is coupled to emission chamber, also through an SMA connector and a collimator. The emission chamber also contains a 5-slot filter wheel, where emission filters are installed. The filtered emission light is directed to a cooled photomultiplier tube (PMT) detector (PMC 100, Becker & Hickl, GmbH), which is sensitive to a spectral range of 185 – 820 nm. The PMT has an excellent TCSPC instrument response of <200 ps FWHM and is controlled through a detector control card (DCC-100, Becker and Hickl, GmbH) which controls the cooling and PMT (Fig. 3.6(c)) gain and has overload protection.

Individual photons are detected using the PMT followed by the pulsed excitation. The detection is achieved through a TCSPC card (SPC-130, Becker and Hickl, GmbH). The TCSPC card (Fig. 3.6(b)) has multiple essential components included onto a single board, as shown in Fig. 3.5. These are two constant fraction discriminators (CFD), and a time to amplitude convertor (TAC), programmable gain amplifier (PGA), analog to digital convertor (ADC), and window discriminator (WD). Since the working of this module is the heart of TCSPC detection, each of these is will be described in further detail below.

The function of a CFD is to accurately detect the timing of each photon pulse, irrespective of the amplitude. Since there is a lot of jitter in the amplitude of the pulse, which is so called “gain noise” and is inherently present in all PMT detectors, a simple thresholding approach would be inaccurate. The working of a CFD is illustrated in Fig. 3.6 (a), where the input pulse is first split into two, one of them is delayed, and then a difference is obtained between the original and the delayed pulse. Zero crossing point is then considered as the time of arrival of pulse, which is essentially independent of the pulse amplitude.

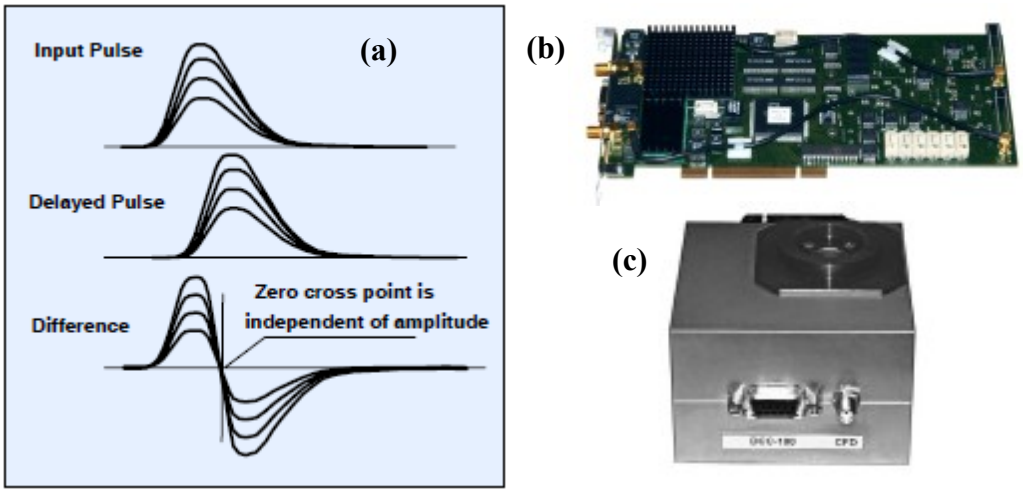

Fig. 3.6. (a) CFD detection scheme; (b) SPC-130 TCSPC card; (c) PMT (PMC-100) with DCC-100 controller card (Source: TCSPC Handbook, 4th Ed. Becker and Hickl, GmbH).

The two CFD’s each give a pulse to TAC, one of which acts as ‘start’ pulse and the other as ‘stop’ pulse. When TAC receives start pulse, it starts charging a capacitor, till the ‘stop’ pulse is received. SPC-130 works in reverse start-stop configuration, where ‘start’ pulse is given only when a photon is detected by the PMT, and the voltage is decreased from maximum, till the next excitation pulse is received. The TAC signal is amplified by the PGA and sent to ADC for digital conversion. The output is the appropriately stored in the memory based on its arrival time. A window discriminator is used to check for false reading by limiting the range of detected voltage. Signals outside the range are suppressed by WD and the TAC is reset to maximum value.

The TCSPC card is installed in the desktop PC, which is also interfaced to rest of the system (excitation/emission chambers). The system is operated using a software package provided by the manufacturer (*Vinci*, ISS, Inc.).

3.3.3 Wavelength selection

In this study, I utilized one excitation filter, with center wavelength 447 nm, and bandwidth 60 nm, also written as 447(60) nm, and four emission filters, namely, 532(10) nm, 562(40) nm, 632(22) nm, and 684(24) nm.

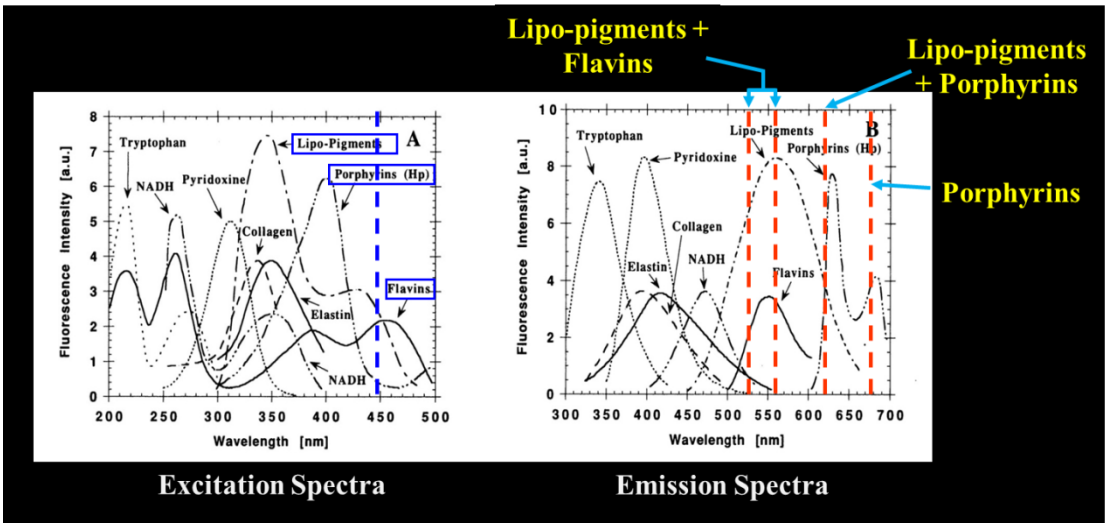

Fig. 3.7. The excitation and emission spectra of endogenous fluorophores, with the targeted fluorophores highlighted (Figure modified from [52]).

As can be observed from Fig 3.7, the specified excitation band excites three endogenous fluorophores: lipo-pigments, porphyrins and flavins to various degrees. On the emission side, each vertical line represents the center wavelength of the filter used. At each given emission wavelength, multiple (or in most cases 2) fluorophores display emission bands. The choice of the wavelength combination was governed by a few factors:

a) Longer wavelengths allow deeper penetration into the tissue, thus providing better depth sensitivity, which is often a concern while assessing tissue margins.

b) A preliminary evaluation with *ex vivo* tissue from a prostate cancer animal model showed fluorescence emission peaks as well as good lifetime signal with excitation at ~450 nm (data not available).

c) A pilot study on subcutaneous prostate cancer rat model revealed excellent contrast between cancer and benign tissue (data presented in Chapter 4).

d) The emission wavebands cover multiple combinations of fluorophores. Since this region is relatively unexplored for prostate tissue, a wide coverage was also an experimental decision.

Therefore, the excitation filter wheel contains only one filter, and remains static for the duration of experiment, while data were sequentially acquired by rotating the emission filter wheel after each lifetime curve acquisition. The automation and control for data acquisition was achieved through *Vinci* software (ISS, Inc.).

3.4. Data Processing and Analysis

Eq. (3.3) describes typical fluorescence decay of a fluorophore. With such a model, a non-linear least square approach is typically used to fit the exponential model to the measured data, obtain value of the lifetime constant, τ. However, biological tissues are more complex than a standard fluorophore dye, such that there can be multiple fluorophores that can be excited within the tissue with same excitation. In such cases, a multi-exponent model can be utilized to model the fluorescence decay, a general form of which is given by Eq. (3.4)

$$I(t) = \sum_i a_i \exp\left(-t/\tau_i\right) + c \tag{3.4}$$

$$\tau_m = \sum_i f_i \tau_i \tag{3.5}$$

$$f_i = \frac{a_i \tau_i}{\sum_i a_i \tau_i} \tag{3.6}$$

Where a_i is the amplitude of lifetime component τ_i, and f_i represents the fractional contribution of i^{th} lifetime decay component. The constant 'c' was added in Eq. (3.4), to account for baseline (DC) noise. Equations (3.5-3.6) describe the calculation of integral-intensity-weighted or fractional-weighted mean lifetime (τ_m), which is the most common way of representing mean lifetime in presence of multiple exponents. The above model was utilized for data analysis, and non-linear least square curve fitting using trust-region optimization method was implemented in Matlab (The Mathworks, Inc., USA).

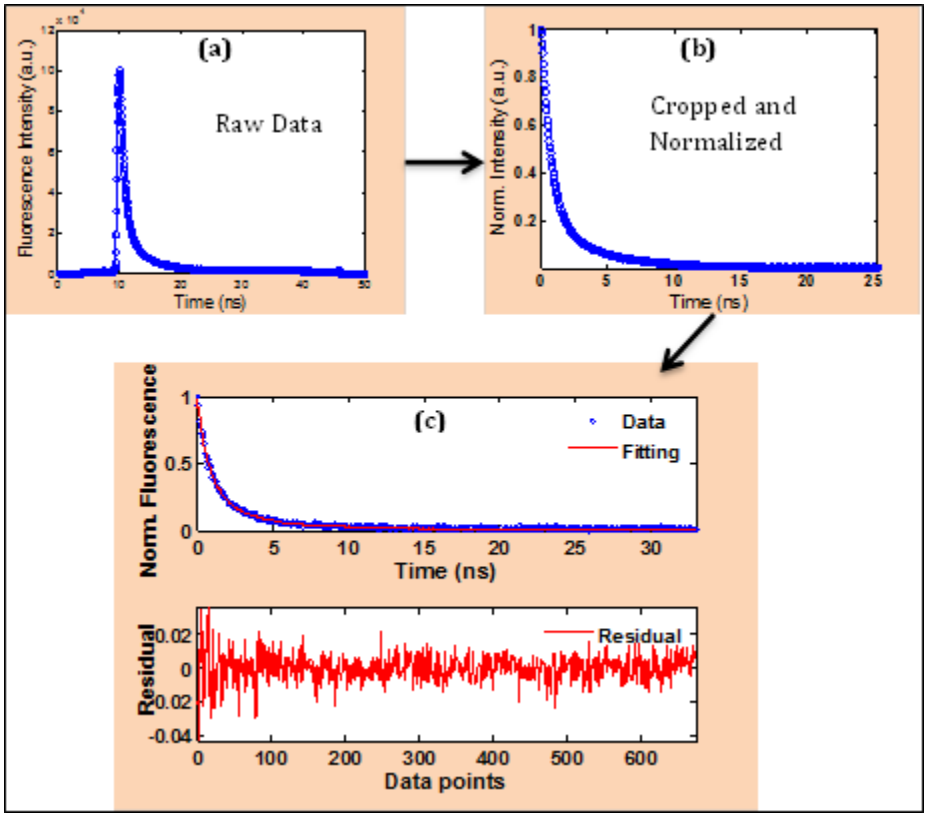

Fig. 3.8 Lifetime Data processing flow: (a) Raw data from ex vivo prostate tissue; (b) Data Cropped to the peak, and normalized from 0 to 1; (c) Result of data fitting to a two component exponent model (i = 2 in Eq. (3.4)), with residuals plotted at the bottom.

3.4.1 Analysis algorithm

The raw data was cropped till the peak intensity value, and the resulting decay cuve was normalized between 0 and 1. This normalization process was done to remove the effects of

fluctuations or changes in laser intensity on the obtained lifetime values in my longitudinal study. The normalized data was then fitted using multi-exponent model, described by Eq. (3.4). A stepwise graphical representation of data processing using a two component model using one of human ex vivo prostate lifetime reading is presented in Fig. 3.8.

There were two important findings in the data processing routine. First, the addition of a constant term in Eq. (3.4) is essential to account for the baseline noise. In absence of constant term, the model tries to compensate for the baseline noise by the exponent terms, which often leads to features in the residual, as can be seen from Fig. 3.9. Although the curves overlap well, features observed in the residual indicate an inadequate fit. The error also leads to unstable values of longer lifetime component (τ_2), especially for noisy data.

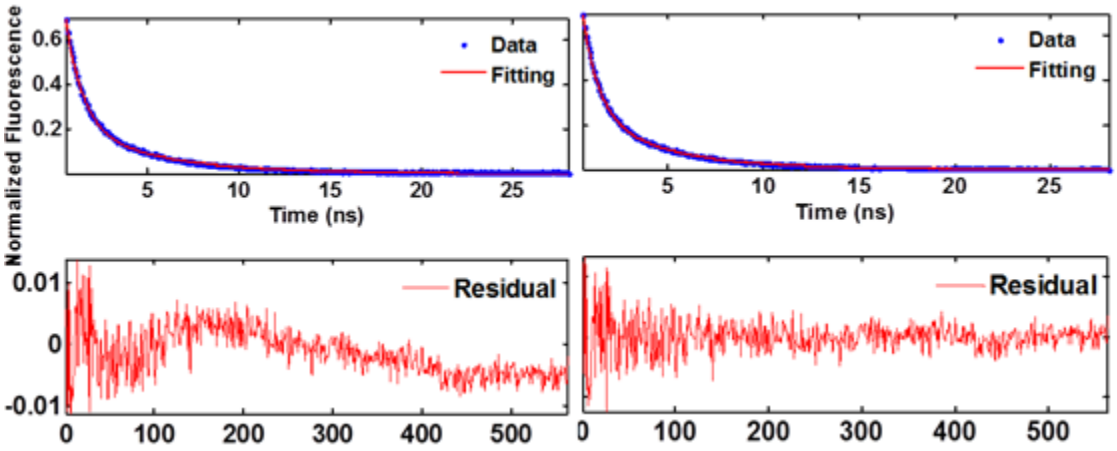

Fig. 3.9. Effect of adding constant 'c' in the two exponent model: (left) fitting without a constant term; (right) fitting with constant term included. The difference is more evident in the residual.

The second important finding for data fitting is the selection of two-exponent model. Looking at Fig. 3.7 again, it can be observed that all chosen emission bands predominantly cover two fluorophores, hinting towards the use of a two component exponent model biological tissues. However, to establish this fact, three different models were compared, including single-exponent (*Exp 1*), two-exponent (*Exp 2*), and three-exponent (*Exp 3*) models. To do so, 16 lifetimes curves from ex vivo human prostate tissue were selected at 532 nm emission, and

each curve was analyzed using all three exponent models. To assess the goodness of fit, three metrics were calculated for each fit, names, sum squared error (SSE), coefficient of determination (R-square) and adjusted R-square. Mean and standard deviation obtained using all 16 curves for 532 nm is plotted in Fig. 3.10.

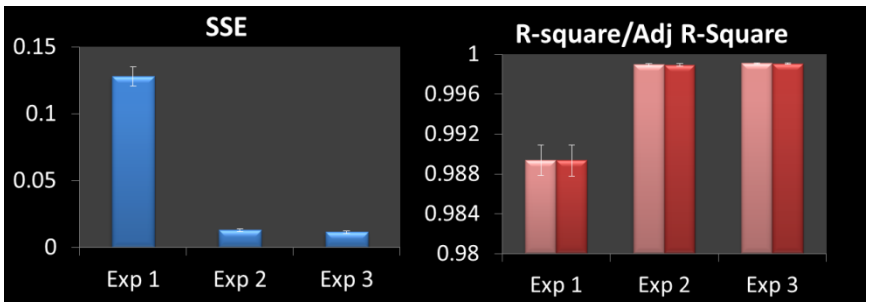

Fig. 3.10. A comparison of three exponent lifetime decay models with one, two or three exponent terms included. The error bars represent standard deviation across 16 curves.

It was observed that *Exp 2* showed significant improvement over *Exp 1* whereas, *Exp 2* and *Exp 3* were comparable, as indicated by all three goodness of fit parameters. Since *Exp 2* and *Exp 3* are comparable, I decided to choose *Exp 2* for data analysis, to avoid overfitting, and also to be consistent with theory observed in Fig. 3.7. Similar results as shown in Fig. 3.10 were also obtained for other three emission wavelengths, i.e. 562 nm, 632 nm and 684 nm.

To summarize, it has been established that a two-exponent model is an adequate fit for the designed excitation-emission wavelength combinations, and explains the obtained curves well. For each lifetime curve, five parameters will be extracted, namely, a_1, τ_1, a_2, τ_2, and τ_m, as decribed by Eqs. (3.7-3.8) below:

$$I(t) = a_1 \, \mathrm{e}^{-t/\tau_1} + a_2 \, \mathrm{e}^{-t/\tau_2} + c \tag{3.7}$$

$$\tau_m = \frac{a_1\tau_1^2 + a_2\tau_2^2}{a_1\tau_1 + a_2\tau_2} \tag{3.8}$$

3.5 Device Testing and Validation

In section 3.4, a data processing routine was established, which fits the tissue lifetime data very well. However, the accuracy of the lifetimes measured still needs to be validated. In this section, the testing procedure will be described and the results will be presented.

The best way validate the system is to evaluate it against a known standard. This was achieved by establishing a doubly scrutinized test protocol. Two standard dyes with well separated lifetimes were chosen, and the lifetimes were compared with the lifetimes obtained with the AFLS system described here. Also, to add one more standardization aspect, same solutions were also measured with an independent gold standard fluorescence lifetime measurement system (Courtesy: Dr. Ignacy Gryczynski and Dr. Zygmunt Gryczynski at *The University of North Texas Health Science Center* and *Texas Christian University*, respectively).

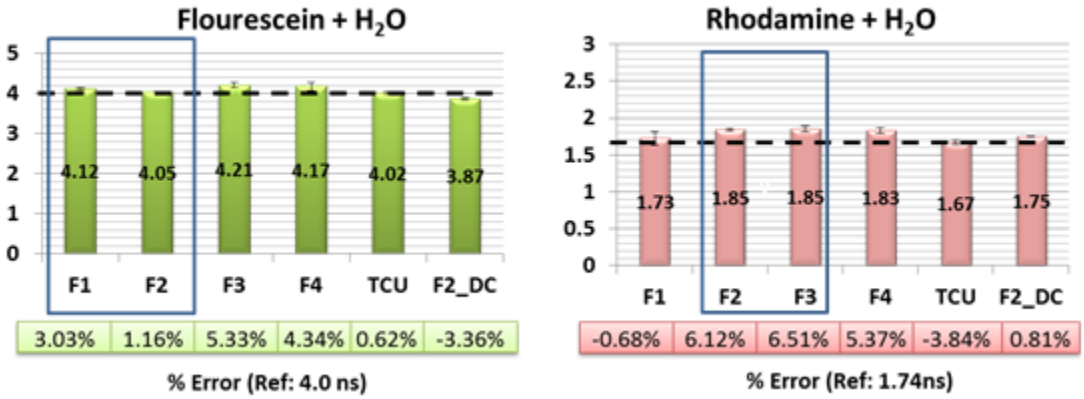

Fig. 3.11. Validation results obtained using reference dyes measured by all four emission filters (F1 = 532 nm, F2 = 562 nm, F3 = 632 nm, and F4 = 684 nm). TCU represents the readings taken at TCU using the Fluotime system, and F2_DC represents the deconvolved response from filter F2. The numbers below represent % error compared to the reference lifetime from literature. Y-axis represents mean lifetime in (ns).

The details of this experiment were as follows: two standard fluorescence dyes, one with longer lifetime (Fluorescein, 4.0 ns), and one with shorter lifetime (Rhodamine B, 1.74 ns)[69] were selected. These dyes were dissolved in water, and a solution of each was prepared. First, a part of this solution was measured by fiber-based AFLS system in reflectance geometry by

placing the solution in a black well-plate. The measured integral-intensity-weighted mean lifetimes calculated using a two component exponent model using all four filters (F1 to F4) are shown in Fig. 3.11. Considering the emission spectra of these dyes, F1 & F2 in case of Fluorescein and F3 & F3 in case of Rhodamine are closest to the peak, so should present the estimate with best signal to noise ratio. They are highlighted in Fig. 3.11. As can be seen, the maximum errors were less than 7% in all cases. These results were also confirmed by measuring a part of the same solution with another commercial TCSPC system (FluoTime 200, PicoQuant GmbH, Germany), using 1 mm thick cuvette and front-face geometry as described in[70]. The system is equipped with a micro-channel plate (MCP) detector[71] and excitation wavelength is selected from tunable laser system (Fianium SC400-4) with opto-acoustic filter system. This data set was analyzed using a commercial FluoFit software package (PicoQuant GmbH). The calculated integral-intensity-weighted lifetimes were 4.02±0.03 ns and 1.67±0.03 ns, for Fluorescein and Rhodamine B, respectively (TCU in Fig. 3.11), displaying an error of less than 5%. Overall, the deviations between measured lifetimes by our AFLM system and the PicoQuant unit were within 10% of each other.

3.4.1 Instrument response function of TCSPC system

While analyzing fluorescence lifetime data using any system, instrument response function (IRF) is one important aspect that should be considered. So far in my analysis, I have ignored this factor, for a good reason, that will be described in this section.

One of the advantages of TCSPC systems lies in the fact that its IRF is not limited by the IRF or single electron response (SER) of the PMT. Since it counts one photon at a time, the resolution is rather limited by transit time spread (TTS) of the detector which is typically an order of magnitude shorter than the SER, rendering a much better temporal resolution to TCSPC system. The IRF of the system is shown in Fig. 3.12, which was measured using a silver coated optical mirror. As can be seen, the FWHM for the IRF is about 300 ps. Considering such small

FWHM, it can be hypothesized that for considerably long lifetimes, de-convolution of IRF may not affect the measured lifetimes to a significant degree.

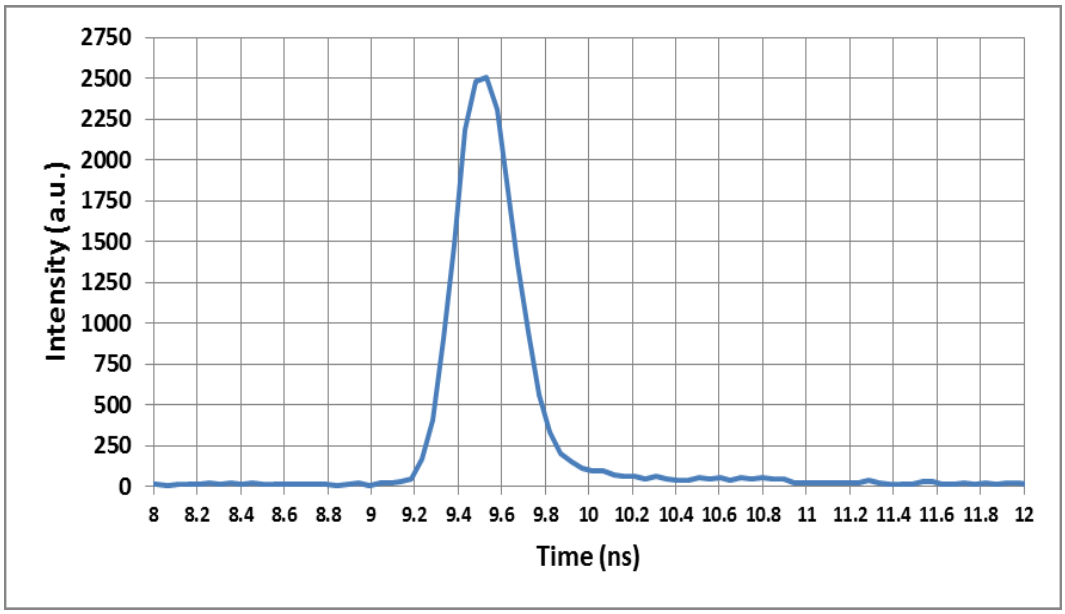

Fig. 3.12 IRF of AFLS system, measured using an optical mirror.

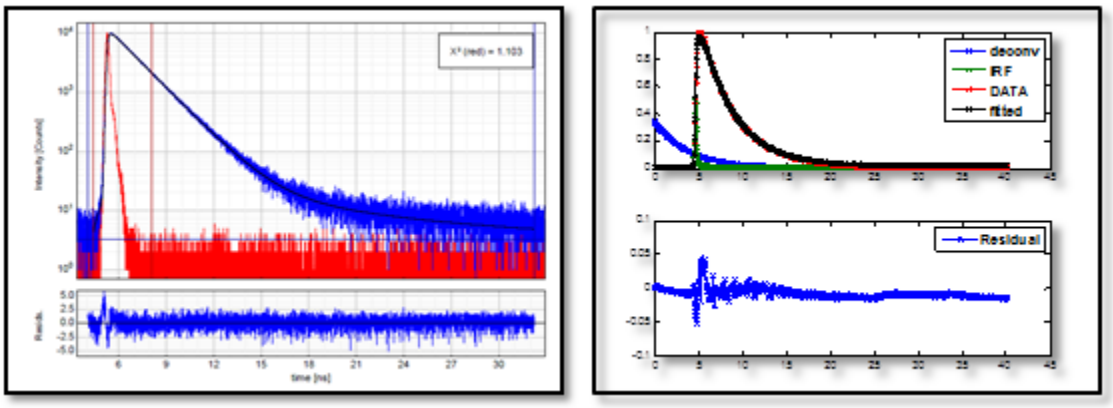

Fig. 3.13 Comparison of curve fitting using de-convolution of IRF: (Left) results of commercial analysis software (FluoFit). Red is IRF, blue the measured data, and black line is the fit; (Right) results of software routine implemented in Matlab to deconvolve the lifetime curve (blue) from measured data (red). Black curve represents the fit; In both cases, bottom curve shows the residual, which is comparable in each case. Also, note the y-axis is plotted in log-scale in left curve.

The stated hypothesis is supported by the results reported in Fig. 3.11, where the TCU lifetime was obtained after de-convolution of IRF, whereas, F1-F4 lifetimes were obtained

without de-convolution. Also, for comparison, a de-convolution routine was implemented in Matlab, and the measured IRF (Fig. 3.12) was de-convolved from F2 filter curve for both dyes (F2_DC in Fig. 3.11). Two observations can be made at this point: (1) The errors between convolved and de-convolved lifetimes are within 7%, and (2) the errors are smaller for longer lifetimes (Fluorescein, Fig. 3.11).

Also, an illustration of de-convolution based fitting is shown in Fig. 3.13. While both commercial software and in-house algorithm result in similar residuals, a comparison with Fig. 3.9 does not convincingly show improvement. Additionally, the process of de-convolution is not trivial, and may itself induce some variability (although small) in the results. Based on the above arguments, a de-convolution free data processing approach will be employed throughout this dissertation.

3.6 Summary and Conclusions

Auto-fluorescence lifetime spectroscopy (AFLS) technique has been developed, with excitation at 447(60) nm and four emissions at 532(10) nm, 562(40) nm, 632(22) nm, 684(24) nm, acquired sequentially. For the given design, a two-component exponential decay model is found adequate for data analysis. Comparison with a commercial TCSPC system was conducted to validate the accuracy of the custom AFLS system, and the results were satisfactory (less than 10% error in measurement), with even better repeatability (assessed by standard deviation, Fig. 3.12). In the next Chapter, integration of the two modalities described in Chapters 2 & 3 will be given, and two animal studies based on dual-modality optical system will be described.

CHAPTER 4

SYSTEM INTEGRATION AND ANIMAL STUDIES

4.1 Animal Study I: Rat subcutaneous prostate cancer model

The first tissue feasibility study for the proposed dual modality optical device was conducted on a subcutaneous tumor model on rat fore back. The AFLS part of this study was conducted mainly by Nimit Patel, who was a Research Associate at UT Arlington at the time of the study, which was published[59] in 2011.

The feasibility of both LRS and AFLS systems to be able to differentiate between cancerous and non-cancerous tissues using a rat prostate cancer model was assessed with both ex vivo and in vivo measurements. LRS was used to calculate the absolute concentrations of oxy-hemoglobin, deoxy-hemoglobin and scattering properties of the tissue, while AFLS provided auto-fluorescence lifetime of the tissues at four emission wavelengths (as described in Chapter 3), followed by excitation at 447 nm. Various measured parameters were analyzed to assess the contrast between the tumor and benign tissue, and the efficacy of using these parameters as classifiers for identification of the tumor was determined using support vector machine classification.

4.1.1 Methods

4.1.1.1 Animal model and preparation

Four one-year old, Copenhagen rats weighing 300-400 g were used in this study. Dunning R 3327 AT3.1 rat prostate carcinoma cells (~5×10^6) were injected subcutaneously on the fore back of each rat, followed by everyday monitoring of the tumor growth till it reached the volume of ~1.5 cm^3. Once the desired volume was reached (in about a week), the rat was then anesthetized using a Ketamine/Xylazine combination. An incision was then made on the rat's fore back to expose the tumor and also part of normal fore back tissue. The exposed

tissue/tumor surface was cleaned by flushing phosphate buffered saline (PBS), followed by multiple optical measurements with a bifurcated optical probe (see Fig. 1 and next sub-section). All procedures for the animal studies were approved by IACUC at University of Texas at Arlington.

4.1.1.2. Instrumentation and measurement protocol

The instrumentation used for this study has been described in Chapters two and three in detail. A block diagram schematic of this implementation is shown in Fig. 4.1. A separate fiber optic probe was used for each modality.

For LRS, a bifurcated fiber with source and detector fiber diameters of 100 μm, and core-to-core separation of ~110 μm, was utilized. Calibration constants k_1 and k_2 (see Chapter 2, Section 2.2.3) for this system were calculated to be 3.08 and 16.821, respectively.

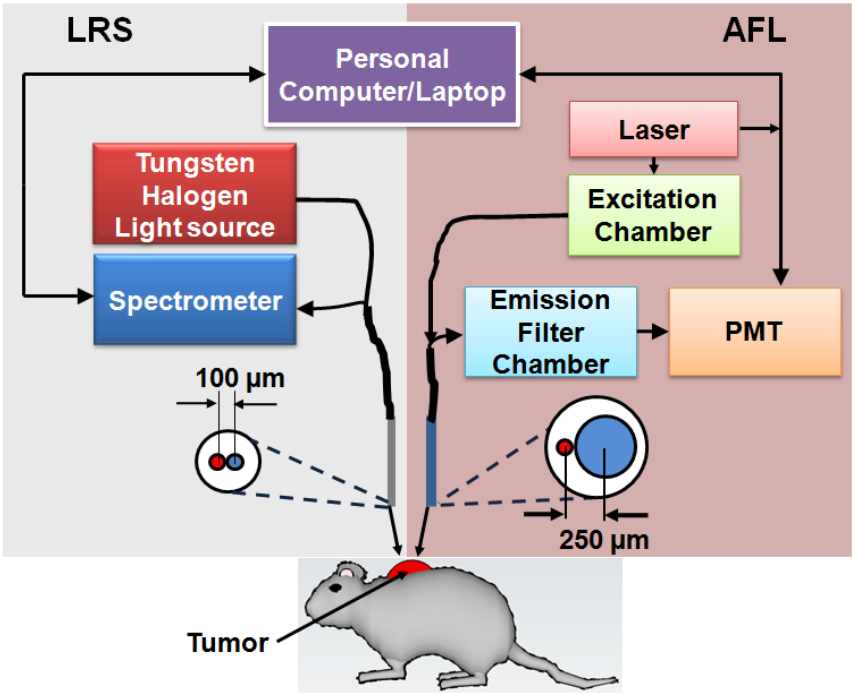

Fig. 4.1 A block diagram illustrating experimental set-up for a LRS system (left) and AFLS system (right). Measurements were made sequentially, by placing the fiber tips on the tissue surface. A closer view of bi-furcated fiber tips are shown for each fiber (red = source; blue = detector).

LRS probe was placed in contact with the tissue, and a stereotactic frame was used (Fig. 4.2) to make sure the pressure on the tissue was minimal, and consistent across measurements. Rat 1 readings were obtained without the use of sterotactic frame, and were thus excluded from the analysis for consistency.

For AFLS, another bifurcated fiber probe with source fiber diameter 100 μm, and detector fiber diameter 400 μm was utilized (Fig. 4.1). For AFLS measurements, the probe was held at ~1 mm above the tissue. The readings were obtained sequentially for both modalities. Up to 5 readings were obtained on each tissue type. The measured locations were not co-localized across two modalities, and represent the bulk average readings across the two tissue types.

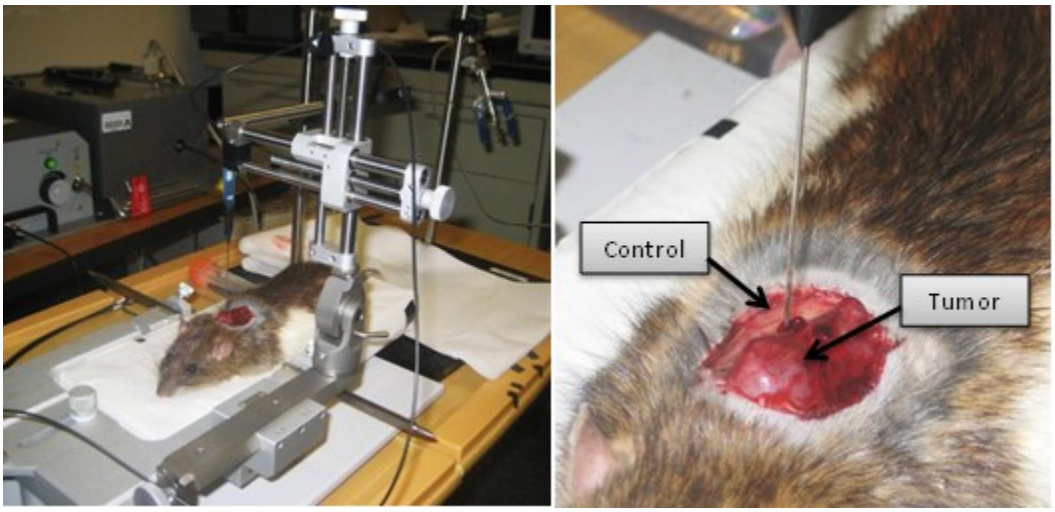

Fig. 4.2 Animal experiment set-up showing LRS measurement: (Left) LRS probe place in contact with the tissue using a stereotactic frame holder; (Right) a closer view shows tumor location and morphology.

4.1.2. Results and Analysis

4.1.2.1 AFLS results*

*(*Disclaimer: The analysis presented in this section was performed by Nimit Patel, Research Associate in our Laboratory, at that time*)

The lifetime curves obtained for each emission wavelength were analyzed using a two component exponent model (Eq. 4.1), without the use of constant term. The mean lifetime for each emission wavelength was selected as contrast parameter, and was averaged over all 4 rats. Figure 4.3 shows the comparison for averaged mean lifetime with standard deviation for *in vivo* measurements.

$$I(t) = a_1 \mathrm{e}^{-t/\tau_1} + a_2 \mathrm{e}^{-t/\tau_2} \quad ; \qquad \tau_m = \frac{a_1\tau_1^2 + a_2\tau_2^2}{a_1\tau_1 + a_2\tau_2} \tag{4.1}$$

It can be noticed from the plots that the averaged mean lifetime from cancer is lower than that from normal tissue at all emission wavelengths, as summarized in Table 4.1. This table also contains p-values that were obtained using a mixed model repeated measures ANOVA between the cancer and normal group. In addition, the average mean lifetime over 4 emission wavelengths was found to be 1.52±0.09 ns and 2.61±0.22 ns for *in vivo* cancer and control, respectively.

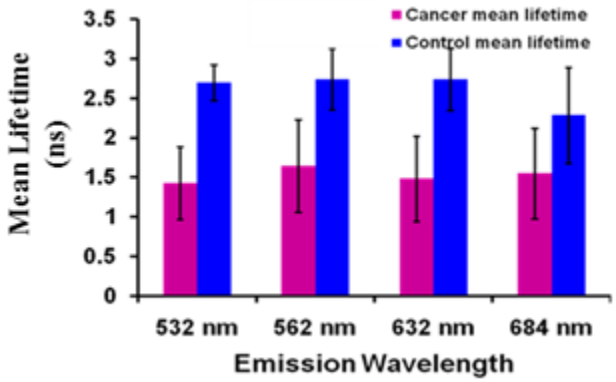

Fig. 4.3 Comparison of averaged mean lifetime for cancer and control tissues (n=20).

Table 4.1 Summary of AFLS mean lifetimes for tumor and control tissue

		Emission Wavelength (nm)			
		532	**562**	**632**	**684**
Mean Lifetime (ns)	**Tumor**	1.43	1.65	1.48	1.55
	Control	2.7	2.74	2.74	2.29
p-value		2.85×10^{-13}	5.70×10^{-8}	9.04×10^{-11}	2.0×10^{-4}

4.1.2.2. LRS results

LRS data was analyzed using the absolute quantification algorithm explained in Chapter 2. The fitted parameters obtained were concentrations of oxy-hemoglobin ([HbO]) and deoxy-hemoglobin ([Hb]), scattering coefficient (μ_s'), and derived parameter, (HbT] = [HbO] + [Hb]). Figure 4.4 shows the results of these four parameters derived through LRS. The spectra were averaged over multiple points of each tissue type (either cancer or control) from each rat, and standard error of mean (SEM, represented by error bars) was calculated and shown. The values of [HbO] and [HbT] exhibited an increase in concentration in the tumor tissue as compared to the normal tissue in all 3 rats.

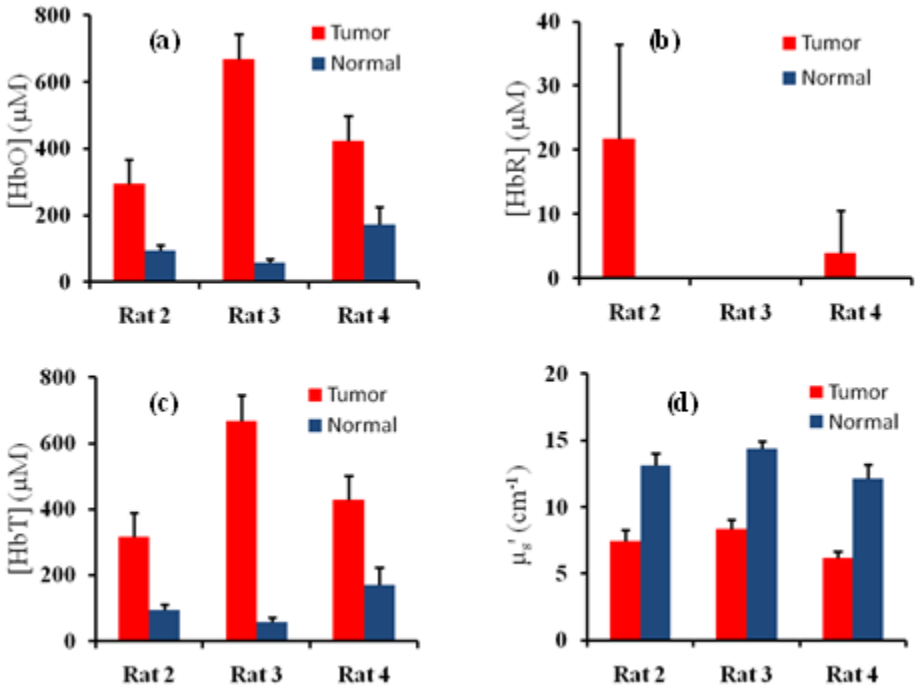

Fig. 4.4 Comparison of (a) [HbO], (b) [HbR], (c) [HbT], and (d) μ_s' values at 750 nm derived from *in vivo* rat tumor tissue and control tissue with LRS. Note that values of [HbR] are very heterogeneous, having a large range from 20 μM to 0.1 μM, some of which are unrecognizable in the figure.

The values of [HbR], on the other hand, were found to be very small compared to those of [HbO], and the standard error was relatively higher. Furthermore, the values of μ_s' were found to be smaller with a relatively small SEM in tumor tissue, as compared to those in the normal

tissue. A mixed model analysis for repeated measures revealed significant differences between tumor and control tissue in [HbO] (p = 0.03), [HbT] (p = 0.03), and μ_s' (p = 0.01). Difference in [Hb] was found to be insignificant with p-value of 0.22.

4.1.2.3. Classification accuracy

In order to evaluate whether any of the parameters hold potential to be used as an intrinsic biomarker, a support vector machine (SVM) classification algorithm was employed[72]. In this approach, first, any two independent parameters are chosen from the list of fitted parameters, such as four mean lifetimes at the four emission wavelengths, [HbO], [HbT], and light scattering coefficient, as classifiers; second, the leave-one-out cross validation method is used to determine the sensitivity and specificity for the chosen paired classifiers. Since more than two parameters were available as classifiers, various combinations of parameters were tested (see Table 4.2) to examine which pairs of parameters could be selected as best classifiers. For AFLM, with 20 data points available in each category (tumor and control) for testing, and perfect sensitivity and specificity of 100% was obtained for all possible pairs in wavelength combinations. Table 4.2 lists only a couple of wavelength pairs as an example. For LRS, 14 data points were available in each category, and the best pair as classifiers was determined to be of [HbO] and μ_s' at 750 nm, which gave both sensitivity and specificity of 92.86%.

Table 4.2 Sensitivity and specificity values calculated for different pairs of obtained parameters using two modalities.

	Classification Parameters				
	LRS (n = 14)			**AFLM (n = 20)**	
	[HbO] and [HbT]	**μ_s' (750nm) and μ_s' (830nm)**	**[HbO] and μ_s' (750nm)**	**532nm and 562nm**	**632nm and 684nm**
Sensitivity (%)	71.43	78.57	92.86	100	100
Specificity (%)	71.43	92.86	92.86	100	100

4.1.3 Discussion and conclusions of rat study

This study shows the feasibility of using LRS and AFLS as independent techniques for differentiating rat cancer tissue from normal tissue. Several optical parameters were obtained which could serve as potential biomarkers to identify cancerous tissue. Specifically, Fig. 4.3 presents significant differences in mean lifetime between cancer and non-cancerous tissue, *in vivo*. Such results are expected since AFLS is sensitive to biochemical environment of the fluorophores, which is expected to differ in diseased and healthy tissues. Because of such good sensitivity to local tissue environment, AFLS was found to be very robust, with 100% sensitivity and specificity when the mean lifetimes from any two wavelengths out of the four emission wavelengths were selected to classify cancer from normal tissue. Table 4.2 shows examples of two groups of wavelength combinations.

In case of LRS, an increase in total blood concentration was found, which is indicative of increased vasculature of tumor tissue (Fig. 4.4) as compared to normal tissue. It was also found that in most cases [HbR] levels were very low, indicating a very high level of hemoglobin oxygen saturation (~99%). This could be partially attributed to the fact that the optical readings were taken on the surface of the tissue which was exposed to room air. For deeper tumor regions, we may expect higher values of [HbR] as tumors are generally known to be hypoxic due to their leaky vasculature[73]. Furthermore, light scattering, which is closely associated with cell size and morphology, was found to be significantly different between tumor and normal tissues. This set of results is also expected as cell size and morphology are known to be different in cancerous cells compared to normal cells. It was further observed that μ_s' variability was relatively low at the individual level (indicated by error bars in Fig. 4.4), and that the μ_s' values were well significantly separated between the cancer and control groups, as indicated by a lower p value of 0.01.

While AFLM seems to be able to optimally determine or detect rat prostate cancer with perfect sensitivity and specificity, the following studies will still explore dual-modality approach

for an improved power of discrimination of tissues. One reason is that human prostate is quite different from a solid rat tumor and often has multi-focal cancer lesions with different grades (Gleason scores). It is quite likely that AFLM alone may not be able to clearly identify low-grade prostate cancer lesions, and a second detection modality, such as LRS, may provide a complementary solution. Secondly, in this study a subcutaneous tumor was utilized, which has a morphology that is quite distinctively aggressive (see Fig. 4.2) as compared what may be expected from an orthotopic tumor growing in the prostate itself. An orthotopic model of prostate cancer[74].

In summary, from this limited population pilot study, there is an indication that both AFLM and LRS are robust methods to differentiate prostate tumor from normal tissue in rat prostate cancer model. The sensitivity and specificity of this technique is high, especially for AFLM, which showed 100% accuracy. However, there were certain limitations as mentioned above, including small population size, and tumor not being in its natural environment (prostate tissue). In the next step (Section 4.3), the dual-modality approach will be utilized to investigate discrimination ability in an orthotopic mice model.

4.2 System Integration

In Section 4.1, both the systems were utilized for cancer demarcation in a subcutaneous rat prostate cancer model. Although the results obtained are great, one limitation of the study is that due to two sets of fiber optic probes, different regions of tissue are probed, although belonging to the same tissue. This is fine for independent assessment of the techniques, but to use them as combined dual-modality method, co-localization of obtained readings is essential.

The integration two modalities, LRS and AFLS, into a dual-modality optical device (*dMOD*) was achieved using a custom designed (FiberTech Optica Inc., Montreal, QC, Canada) quad-furcated fiber optic probe. Fig. 4.5 shows the complete set-up of integrated dual-modality system, which works by sequentially acquiring the LRS and AFLM data through the same fiber

optic probe. As can be seen in a schematic of probe tip in Fig. 4.5(c), there are four fiber channels, two dedicated to each modality. Among the two channels, one acts as a source and other as detector. For LRS, both source and detector fibers diameters were 200 μm, with 370 μm core-to-core separation. These fibers are arranged in an orthogonal geometry to AFLS fibers, which comprise of a 100 μm source fiber and a 400 μm detector fiber, with a core-to-core separation of 272 μm. Fig. 4.5(a) shows the system assembled on a portable cart, with various components labeled. Fig 4.5(c) shows an inset of probe with an adjustable probe holder, which was used to make sure all the measurements were made with minimal pressure on the tissue, by eliminating the effect of weight of the probe on sample under interrogation.

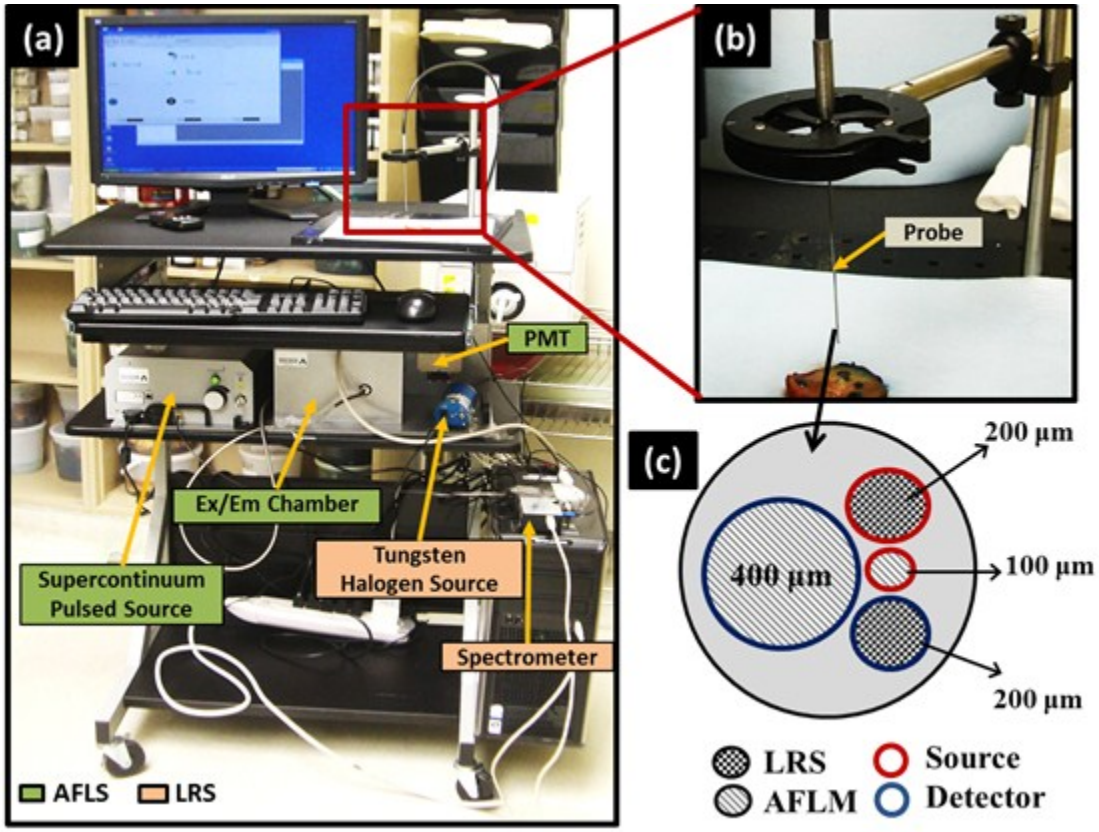

Fig. 4.5 Integrated Instrumentation: (a) Dual-modality optical device on a portable cart (b) Inset showing probe positioning on the sample (c) Front face of the probe tip showing arrangement of source and detector fibers.

4.3 Animal Study II: Mouse orthotopic prostate cancer model

After successfully evaluating the two techniques in vivo in a subcutaneous model in Section 4.1, this part of my study aims at discrimination of prostate cancer in its natural environment, from the surrounding benign prostatic tissue by utilizing a mouse model of orthotopic prostate cancer. The *dMOD* system shown in Fig. 4.5 was utilized for this study.

4.3.1 Methods

4.3.1.1 Animal procedures for tumor implantation and measurement

10 SCID (Severe Combined ImmunoDeficiency) mice were injected with cancer cells for this study. All the animal procedures were performed by researchers in Dr. J.T. Hsieh's laboratory (Crystal Gore and Timothy Dobin) at the Department of Urology at UTSW Medical Center, Dallas, TX. All the animal procedures were approved by the IACUC committee at UTSW Medical Center.

Briefly, the tumor was grown on the site of prostate gland by orthotopic prostate injection. The mouse was briefly anaesthetized with mouse cocktail (ketamine / xylazine / acepromazine) with a dose of 1ml/kg via IP (intra-peritonial) route. An incision of 1 – 2 cm was made right across the abdomen above the fat pad and the muscle layer was cut. The bladder was then carefully pulled outside the body; if full, it was emptied using a gauze pad. The prostate was localized at the base of the bladder. PC3-DAB2IP-KD cells ($1X10^6$, transfected with luciferin gene), were then injected into the ventral lobes of the prostate using a 28 ½ gauge syringe. The prostate and the bladder were placed back into the body cavity. The muscle wall was then carefully closed by using absorbable sutures. Also, the skin was completely closed using autoclips.

5 days after the injection, bioluminescence imaging (BLI) was performed for all 10 mice to monitor the tumor growth. Gaseous anesthesia was administered by small animal anesthesia machine following manufacturer's instructions (with oxygen and 1% isoflurane). Animals

received anesthetic via a facemask. Anesthetized animals were held in place by use of Velcro straps. A solution was prepared of D−luciferin, sodium salt monohydrate (Biosynth, Chicago, IL; L−8240) in phosphate buffered saline (PBS; pH 7.4; Invitrogen Corporation, Carlsbad, CA) to a concentration of 17 mg/ml. The tumor was observed in all 10 mice, with varying BLI intensities, indicating different sizes. The optical measurement was done on day 7, day 8 and day 10, depending on the tumor size observed on BLI.

On the day of measurement, the mouse was anesthetized using mouse cocktail (ketamine / xylazine / acepromazine) with a dose of 1ml/kg via IP route. An incision was made in a manner similar to the tumor cell implantation; the prostate was localized at the base of the bladder, and was exposed for optical measurement. The tissue was then resected and preserved in formalin for further histological analysis

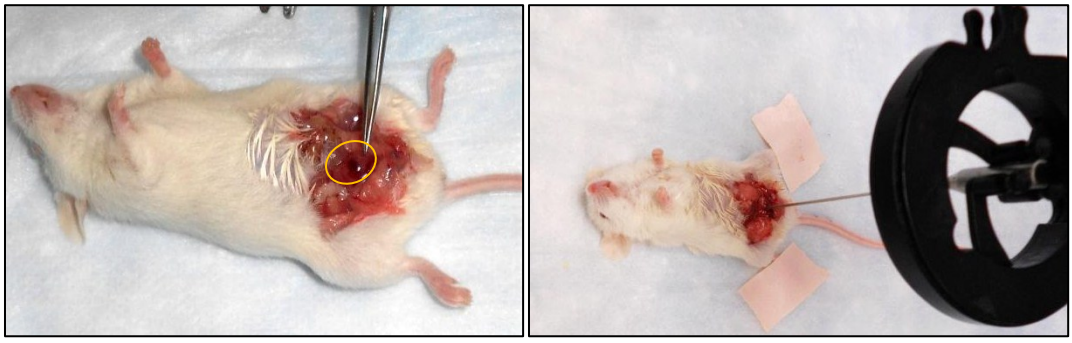

Fig. 4.6 (Left) Tumor bearing prostate of mouse exposed for measurement. The prostate is circled in yellow. (Right) *In vivo* measurement set-up.

4.3.1.1 Optical Measurement

Once the prostate was exposed, the probe was gently placed on the prostate tissue, and readings from both LRS and AFLS were obtained sequentially. Foe each prostate, 2-3 readings were obtained each on ipsi-lateral and contra-lateral sides, given the small size of prostate tissue.

4.3.2 Results

As mentioned in methods, 10 mice were injected with prostate cancer cells. However, this population would be sufficient to compare ipsilateral and contralateral sites of injection for

tumor and benign tissue, iff the growth of tumor could be contained only on one side. However, in practice, it is not possible to precisely control the growth especially since the mice prostate is very small. Therefore, additional control mice were used to compare the cancer vs. non-cancer tissue (n =11, 7 SCID mice and 4 B6/129 mice).

4.3.2.1 AFLS Results

Each lifetime curve was used to derive 5 parameters using the two component exponent model, as described in Chapter 3 (Eq. 3.7, 3.8), namely, τ_1, τ_2, τ_m, a_1, a_2. Each of these parameters was analyzed for differences between cancer and control side.

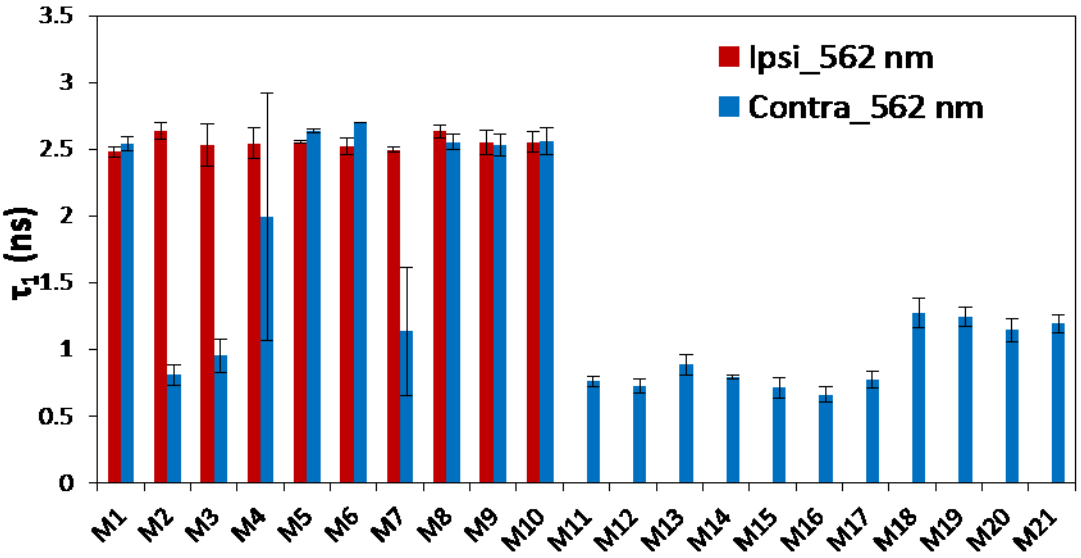

Fig. 4.7 Comparison of lifetime (τ_1) for cancer (M1 to M10) and control mice (M11 to M21), at 562 nm emission, where M1 represents mouse number 1 of 21. Ipsi (red) and Contra (blue) represent the average of readings taken on ipsilateral (side of injection) and contralateral readings for M1 to M10, whereas for M11 to M21, Contra (blue bars) represents the average of all the readings on the specific prostate. Error bars represent standard deviation.

Figure 4.7 shows the averaged readings of τ_1 for all mice at 562 nm. For mouse number 1 to 10 (M1 to M10), red bars represent the readings taken on the side of injection, whereas the blue bars represent the readings taken on the opposite side (contralateral). 2-3 readings were taken on each side and the plot shows average and standard deviation (error bars) in each case. For control mice (M11 to M21) only blue bar is plotted, which represents the average of

~4 readings taken on either side of the prostate along with the error bar. It can be observed from Fig. 4.7 that τ_1 is longer in cancer mice (ipsilateral side), as compared to control mice. Within mice comparison of ipsilateral and contralateral side of cancer mice shows that some mice (M2, M3, M7, and possibly M5) show contralateral signals similar to control mice, indicating that the tumor may not have spread to the opposite side, while in the other cases, the cancer was most likely spread.

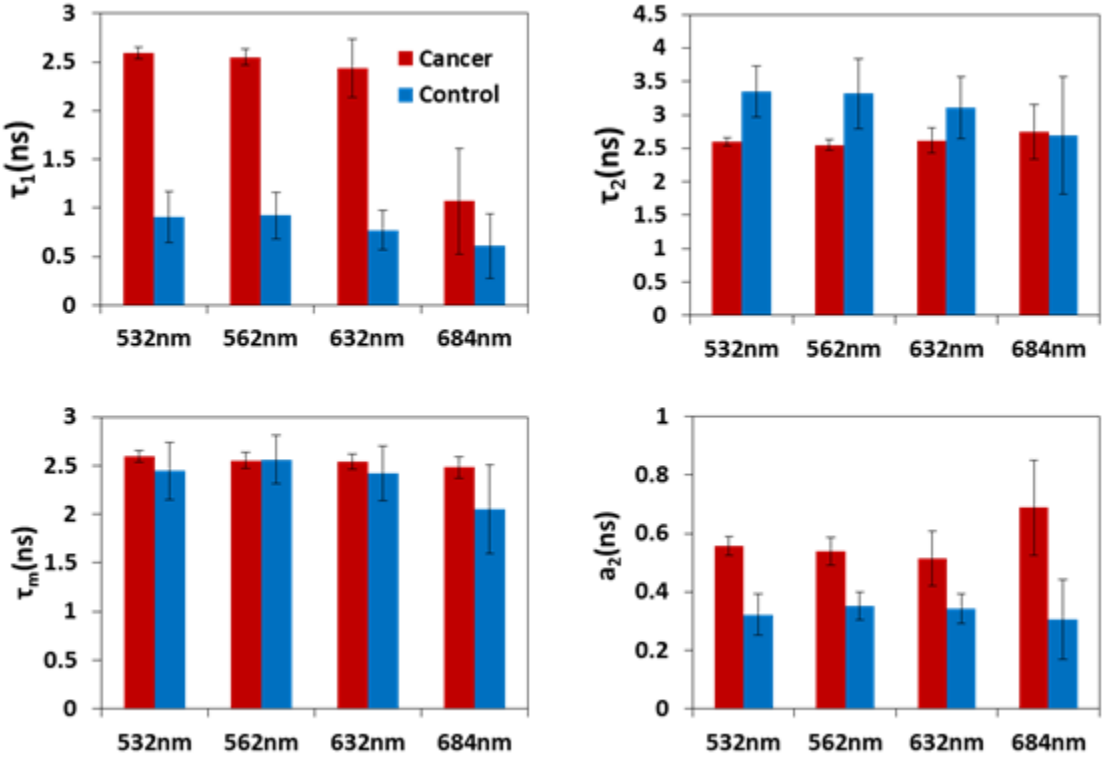

Fig. 4.8. Mean of various lifetime parameters, showing comparison of cancer and control mice for all emission wavelengths. The error bars indicate standard deviations. $\mathbf{a_1}$ (not presented here), did not show much contrast between cancer and control as compared to $\mathbf{a_2}$.

Based on the information obtained from Fig. 4.7, the contralateral readings on the cancer mice will be ignored for further analysis, for true comparison between cancer and control tissues. Figure 4.8 shows such comparison of four lifetime parameters, τ_1, τ_2, τ_m, and a_2. As evident, τ_1 provided the highest contrast between cancer and tumor tissue at three of four

emission wavelengths, namely, 532 nm, 562, nm, and 632 nm. τ_2 and a_2 also show good contrast, at these three emission wavelengths.

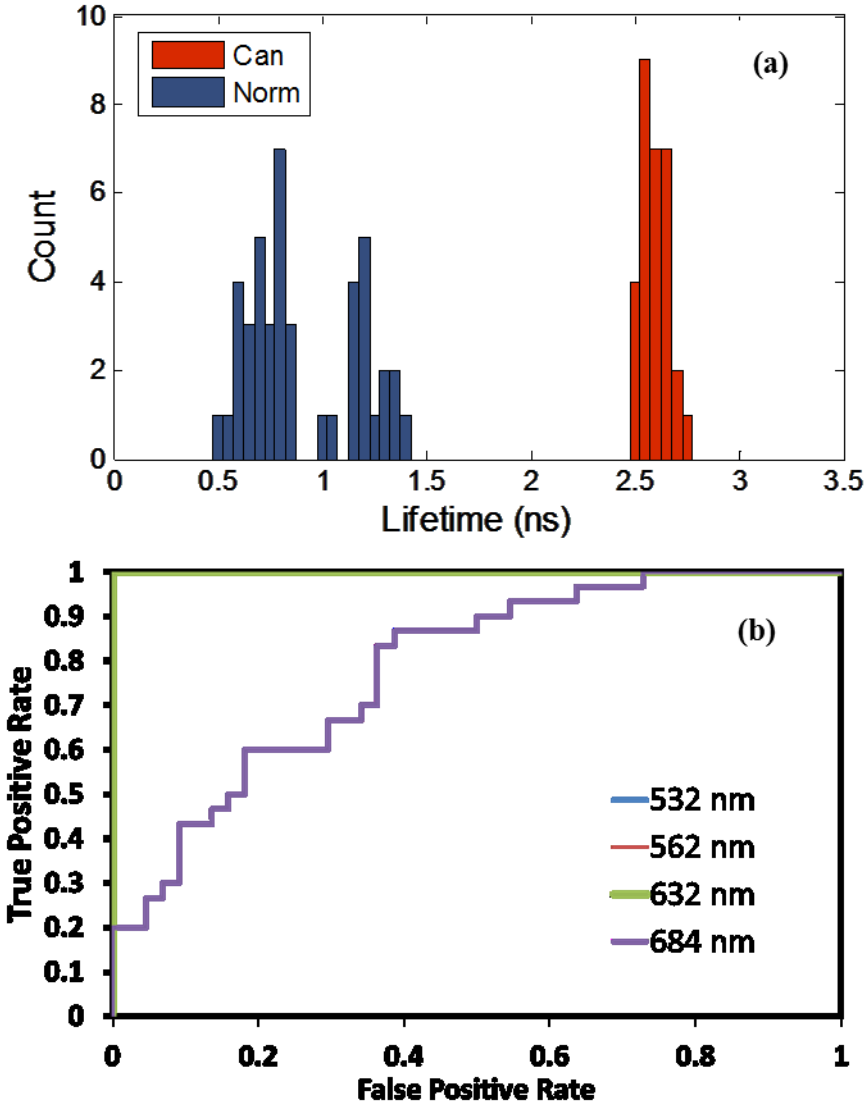

Fig. 4.9 (a) A histogram distribution of cancer (Can) and control (Norm) τ_1 (at 532 nm) values for entire population, showing the separation in two categories; (b) ROC curve generated for τ_1 at all four emission wavelengths. AUC was 1 for all except for 684 nm (AUC = 0.78).

Figure 4.9(a) shows the distributions of cancer (n=30) and control (n=44) tissues for τ_1 at 532 nm. Also observed in Fig. 4.8, these distributions are distinct with no overlap. Therefore the receiver operating characteristic (ROC) curve has an area under the curve (AUC) = 1. This

is also true for 562 nm and 632 nm. Also, seen in Fig. 4.9(b), AUC for 684 nm is 0.78, which is consistent with results shown in Fig. 4.8.

4.3.2.1 LRS Results

LRS results were obtained using quantification algorithm described in Chapter 2. k_1 and k_2, the calibration constants for this set-up were calculated to be 16.732 and 3.505, respectively. An additional absorber, β-carotene was added to the μ_a equation (Eq. 2.2), to account for the pigment in tissue. Some fitted values of total hemoglobin ([HbT] = [HbO] + [Hb]) were found to be in the range of [200 to 1500 μM]. These values were found to be much above the mean observed values of HbT, which was typically below 150. Since the measurement was made in vivo, to exclude the possibility of measuring blood vessels directly, the values exceeding 2 standard deviations were excluded as outliers, reducing the sample size for cancer (n = 26) and control (n = 37) measurements. The resulting mean of contrast parameters along with standard error of mean (SEM) is plotted in Fig. 4.10.

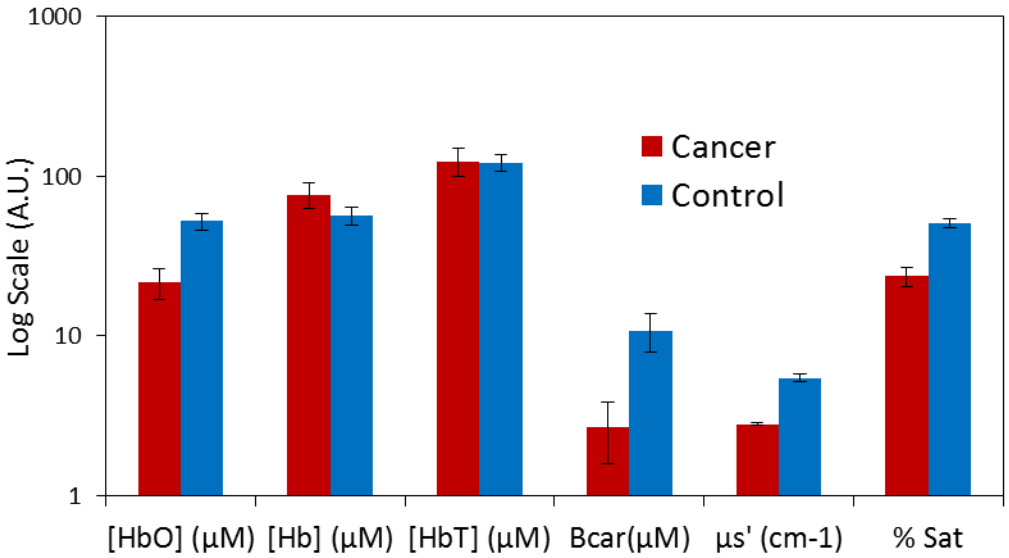

Fig. 4.10 Contrast parameters obtained through LRS measurement for cancer (n=26) and control(n=37) tissue. Units are presented with x-axis labels. Notice that log-scale has been used for visibility. Bcar represents β-carotene and % Sat is the oxygen saturation calculated using [Hb] and [HbO]. Scattering coefficient, $\boldsymbol{\mu_s'}(cm^{-1})$ shown here was calculated at 750 nm. The error bars represent standard error of mean (SEM).

Out of the 6 parameters shown in Fig. 4.10, 3 exhibited significant contrast: [HbO] was found to be significantly lower in cancer tissue compare to control tissue ($p<0.01$); scattering coefficient (μ_s') was calculated at 750 nm and was also found to be lower in cancer tissue compared to control tissue; finally, oxygen saturation [or % Sat = ([HbO]/[HbT])*100], was also lower in cancer tissue compared to control tissue.

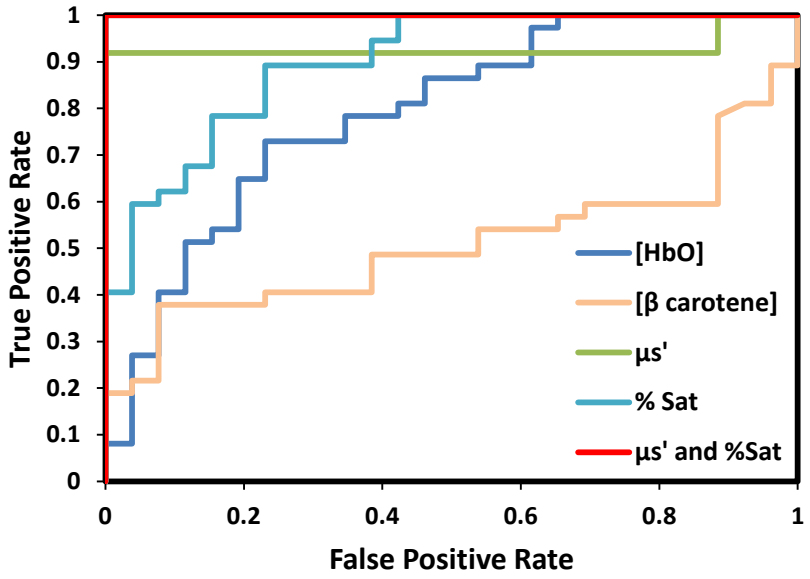

Fig 4.11. ROC curves for various LRS parameters.

Corresponding ROC curves of the four significantly different LRS parameters are plotted in Fig. 4.11. The AUC's for independent parameters were as follows: [HbO] = 0.789; β-carotene = 0.506; μ_s' = 0.928, %Sat = 0.90. It can be observed that the none of these individual parameters compare to the accuracy provided by AFLS (see Fig. 4.9(b)). However, it is possible to take a combination of these parameters in a logistic regression model, and generate a probability value corresponding to each data point (or measured LRS spectrum). Different combination of parameters were tested for logistic regression model, and it was found that combining μ_s' and %Sat provided complete separation between cancer and control tissues (AUC = 1, Sensitivity/Specificity = 100%), as shown in Fig. 4.11. The detailed implementation of

logistic regression (classification algorithm) is provided in Chapter 5. Here, a binomial logistic regression was implemented using 'glmfit' function in Matlab.

4.3.3 Discussion and Conclusions of mice study

In this part of the study, an orthotopic mouse model of prostate cancer was successfully implemented, and dMOD was evaluated for its capability to differentiate cancer bearing prostate tissue from benign tissue. Both LRS and AFLS techniques were able to provide complete differentiation, with 100% accuracy.

AFLS data suggested that excellent contrast can be obtained using only a single emission wavelength (532 nm, 562 nm, or 632 nm), making the design of the system simpler for this implementation. Another noteworthy observation in this study was that τ_1, τ_2, τ_m for cancer tissue were very similar to each other, whereas the control tissues had a short and a long component in τ_1 and τ_2. (see Fig. 4.8). One possible explanation for this could be that there is a single dominant fluorophore in cancer bearing tissue, as compared to control tissue. Alternatively, there could be two fluorophores in each case, with similar and dissimilar lifetime distributions, depending upon pathological condition. In either case, there is a stark biochemical contrast between the two tissue types.

In case of LRS, four parameters were found to have significantly different means between cancer and control tissues. However, further ROC analysis suggested that scattering and oxygen saturation provided better contrast, and a combination of both yielded complete tissue differentiation. However, an important observation in this case is that some points had to be excluded from analysis due to contamination with blood. This is a practical issue that is inherent to *in vivo* LRS measurements. A possible solution to this problem is to set a threshold value for total hemoglobin, based on population studies of absolute maximum tissue [HbT] levels to identify outliers. In this case, 2 times standard deviation was chosen as exclusion criteria.

Finally, this study utilized a control population of two different species, one same as the cancer bearing species (SCID), while the other was different (B6/129). The results therefore suggest that the prostate cancer differentiation in mice may be species independent, although further studies will be needed to confirm this across various species.

4.4 Chapter Summary and Conclusions

In this chapter, LRS and AFLS were evaluated in two distinct animal models: a subcutaneous (SC) rat model, and an orthotopic (OT) mice model. While the first one was a pilot study, the other one was a more statistically and methodically advanced study, with a sufficiently large sample size and in prostate tissue itself.

In both animal studies, excellent contrast was found between cancer and control tissues using AFLS. Each of these studies suggested that use of a single emission wavelength is sufficient to obtain enough contrast for cancer differentiation. However, the contrast parameters were different in both cases, e.g. τ_m being robust for SC model did not provide much contrast for OT model, where τ_1 provided best distinction. This could be attributed to different species in each model, as well as apparently distinctive morphology of both tumors (see Figs. 4.2 and 4.6). Nevertheless, AFLS is proven to be a robust cancer identification tool in different prostate cancer animal models.

In case of LRS, scattering was found to be the most robust contrast parameter in both animal models. Also, the trend was same, scattering being higher in control tissue compared to tumor tissue, although the values were different in both models. However, [HbO] and [HbT] showed different behavior in both animal models. In SC model, both [HbO] and [HbT] were higher in cancer tissue, whereas in OT model, [HbT] was found to be similar, where [HbO] was lower in cancer tissue leading to lower oxygen saturation (% Sat) in cancer tissue. The latter (OT model) finding is consistent with well-known hypoxic nature of tumors [73].

So far, I have established the feasibility and proven the applicability of dMOD in animal models of prostate cancer. However, naturally growing human prostate cancer can be very

different from animal models, and it is very hard to exactly mimic progression or human prostate cancer in mice model. Accordingly, although it appears at this point that only one modality (especially AFLS) may be enough to differentiate prostate cancer from benign tissues, that too with limited emission filters, the true validity of this can only be established after studying human prostate tissue. In light of the above discussion, next chapter will focus on a study of ex-vivo human samples using *dMOD* to examine the feasibility of differentiating human prostate cancer using this novel probe.

CHAPTER 5

HUMAN EX VIVO PROSTATE STUDY: PART I

5.1 Introduction

After the successful evaluation in animal models, the next logical step is to evaluate *dMOD* for human prostate cancer detection. An ex-vivo study was conducted in clinical collaboration with a team of surgeons (urologists) and pathologists to achieve this goal. Prostatectomy samples were selected, and optical readings were taken from fresh tissue (within 1-2 hours of prostate resection), from three types of prostate tissues, namely, prostate cancer (PCa), benign peripheral zone tissue (nPZ), and benign prostatic hyperplasia (BPH, predominantly in transition zone). Different grades of prostate cancer were included in the study, ranging from Gleason grades 7 to 9, which are considered high-grade cancer. About 70% of prostate cancer occurs in peripheral zone, therefore, nPZ was chosen as a discriminatory region. Additionally, BPH was selected as third tissue type, as it is very commonly found in prostate cancer patients, and covers the transition zone, therefore covering the majority of tissues in a typical prostate gland. The goal of this study was to use optical signals obtained from dMOD, and distinguish these tissue types based on their characteristic optical signatures.

Few studies have been reported in recent past, in effort to distinguish prostate cancer from benign prostate tissue[15,50,75-78], mainly utilizing optical methods[15,50] or electrical impedence[15,76-78]. Salomon et. al.[15] reported a sensitivity and specificity of 75% and 87.3%, respectively, for detecting prostate cancer, using a triple spectroscopy method tested on ex vivo prostate tissue. More recently, Halter et. al.[78] reported the use of electrical properties to differentiate prostate cancer from benign tissue, reporting areas under curve (AUC) of 0.9 for discriminating between benign and malignant tissue, and 0.75 for discriminating between low and high grade cancer tissue.

The approach used here to detect prostate cancer is distinct, such that it employs two complimentary optical approaches in *dMOD*, both of which have applied successfully in cancer detection [28,79], but their application to human prostate has been limited, with one publication in LRS[50], by our group, and no published work for AFLS, especially with my current design, as per literature search in July 2012.

In this study, I evaluated *dMOD*, as a potential tool to differentiate prostate cancer from benign tissues. Since the vasculature, morphology and biochemical composition of prostate cancer-bearing tissue is expected to differ from that of benign tissues, with the differences being presumably more pronounced with higher grade and advanced disease, it was hypothesized that LRS and AFLS, alone or in combination, could be used in the identification of prostate cancer. The ability of the *dMOD* optical probe to discriminate between PCa, nPZ and BPH was determined. Also, the performance of this probe in the detection efficiency of individual Gleason grades of prostate cancer, among men with Gleason 7 or higher prostate cancer was evaluated. For each of the above cases, tissue discrimination was achieved through classification algorithm, and sensitivity (Sn), specificity (Sp), Accuracy (Acc) andAUC for a receiver operating characteristic (ROC) curve were obtained as classification measures.

5.2 Patients and Methods

5.2.1 Patient selection and procedures

The study was conducted as per the guidelines of Institutional Review Board at UT Southwestern Medical Center, Dallas, TX, and each patient's informed consent was obtained before the surgery. Patients were selected for intermediate to high grade disease (Gleason score ≥ 7) and moderate to high volume prostate cancer (at least two contiguous biopsy cores each with 20% or more cancer involvement and/or bulky disease by endorectal MRI) so as to optimize spectral yield in this initial proof-of-concept study.

Each patient underwent robotic-assisted radical prostatectomy by one of three surgeons (J.A. Cadeddu, C.G. Roehrborn, and G. Raj) via a transperitoneal anterior or posterior

approach. In each case, the prostate glands were extracted after having completely been disconnected from their blood supply for at least 30 minutes.

5.2.2 Experimental Protocol

Resected prostate glands were immediately immersed in saline, and submitted for *dMOD* measurements. Each gland was first inked as per standard protocol at UTSW for histological evaluation (blue for the left lobe, orange for the right lobe, green for the anterior zone) (Fig 5.1). Dyes were fixed using acetic acid washes. The specimens were divided in a coronal plane, cutting through the location of the tumor nodule as determined by pre-operative biopsy mapping, pre-operative MRI and/or palpation, such that tumor was clearly visible at the cut surface. When necessary, a Diff quick stained touch-prep slide was made of suspected cancer-bearing tissue, confirming the location of prostate cancer cells cytologically. The location of nPZ, and BPH regions on the cut surfaces of the specimens was also identified (Fig 5.1).

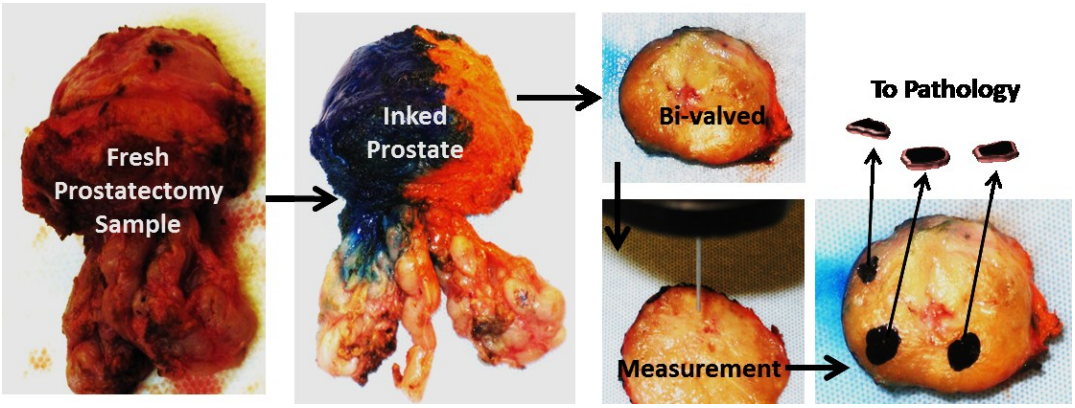

Fig. 5.1 Measurement Protocol

The *dMOD* probe (See Fig 4.5, Chapter 4) was placed in contact with the cut surface of the prostate gland and LRS and AFLS spectra were recorded from each of the pre-specified regions (PCa, nPZ, and BPH). Eight measurements were obtained from each region. Each measured region was then marked with colored dye, and a ~ 1 mm thick section of each measured region was labeled and separately submitted for histological evaluation. Hematoxylin and eosin stained sections from these separately submitted tissue were evaluated by urologic

pathologist for presence and extent of tumor and Gleason grade. Optical measurements were then categorized according to the histologically confirmed regions of interest.

5.2.3 Instrumentation and measurements

The instrument set-up has been described previously in Chapter 4 (see section 4.2). The same set-up as described for mice study was used for this study. The specific procedural changes are described in the next paragraph.

Since the study was carried out in a busy pathology room at UTSW/Zale Lipshy hospital, a light-blocking black fabric was used to cover the measurement area, to avoid ambient light during the measurement. LRS and AFLS data were acquired sequentially for each measured location, without any specific order. The integration time for LRS measurement was in the range of 20-60ms. For AFLS, 5 sec integration time was used for each fluorescence curve. Since 4 wavelengths were utilized, total acquisition time was 20 s. Considering manual switching between the two modalities, and time lag of filter wheels for AFLS measurements, the average acquisition time for each measured location was about 60 s.

5.2.4 Data Processing

For LRS, a spectral width of 500-850 nm was chosen; the corresponding data were fitted to a mathematical model (Eq. 2.1 to 2.5), the details of which have been previously described in Section 2.2.2. Briefly, the measured reflectance *R(λ)*, is used to extract are absorption and scattering coefficients (μ_a and μ_s') of the tissue, using an analytical model[23]. In this study, absorption equation (Eq. 5.1) was modified from Eq.(2.2) to add additional absorbers present in the tissue:

$$\mu_a(\lambda) = [HbO]\,\varepsilon_{HbO}(\lambda) + [Hb]\,\varepsilon_{Hb}(\lambda) + [\%H_2O]\varepsilon_{H_2O}(\lambda) + [Mel]\varepsilon_{mel}\ldots \\ \ldots + [\beta_{car}]\varepsilon_{\beta_{car}} + [Dye_{Or}]\varepsilon_{Or} + [Dye_{Bl}]\varepsilon_{Bl} \tag{5.1}$$

Where, [*Mel*], [β_{car}], [Dye_{Or}] and [Dye_{Bl}] are concentrations of melanin, β-carotene, orange dye and blue dye, respectively. The ε's are the corresponding extinction coefficients for [*Mel*], and [β_{car}] were obtained through Oregon Medical Laser Center (OMLC) online database

created by Scott Prahl (http://omlc.ogi.edu/spectra/; http://omlc.ogi.edu/spectra/Photochem-CAD/html/041.html). The ε_{Or} and ε_{Bl} on the other hand, were the absorption spectra of the dyes, measured using a UV/VIS benchtop spectrometer (Perkin Elmer, Inc.). The dye spectra were added to account for the possible contamination during the bivalving of the prostate, although care was taken to fix the dyes before the cut (see Section 5.2.2). However, it should be noted that since the initial molar concentrations of dyes were not known, the concentrations [Dye_{Or}] or [Dye_{Or}] do not reflect the true concentrations, but are used to remove their weighted contribution to the absorption spectrum, thus giving more accurate values of other absorber concentrations.

Since the water concentration was fixed at 80%, 5 usable parameters were derived from absorption coefficient for tissue discrimination, namely, [Hb], [HbO], [HbT], [Mel] and [β_{car}]. Cell size and density dependent μ_s' was also calculated at 750 nm, yielding overall 6 LRS parameters per measured region. Statistical differences in spectral parameters for PCa, nPZ and BPH were analyzed using a linear mixed model regression analysis implemented in SAS (SAS Institute Inc., NC, USA).

AFLS data analysis has been described in detail in Chapter 3, Section3.3. Briefly, each lifetime curve was fitted with a two-component exponent model, to obtain two lifetimes, $\boldsymbol{\tau_1}$, and $\boldsymbol{\tau_2}$, and their respective weights, $\mathbf{a_1}$ and $\mathbf{a_2}$. Integral-intensity-weighted mean lifetime ($\boldsymbol{\tau_m}$) was also calculated, generating 5 usable contrast parameters per emission wavelength. Since there are four emission curves per measured locations, overall 20 (5X4) parameters were obtained at each location. Each of these parameters were then evaluated for statistical differences between PCa and nPZ, as well as PCa and BPH, using a linear mixed model analysis for repeated measures, implemented in SAS.

5.2.5 Classification and ROC Analysis

As explained above, both LRS and AFLS methods resulted in 20 lifetime-driven, 4-wavelength-dependent parameters from AFLS and 6 absorption and scattering dependent parameters from LRS at each measured location on the prostate specimens. These 20 plus 6

characteristic parameters can be utilized as classification features for PCa discrimination. A two-step process was implemented in order to assess the classification ability of each technique independently, as well as of the combined dual-modality approach: step one was to implement a feature selection algorithm in order to select the best feature set for tissue type classification; step two was to develop a multinomial logistic regression model along with 10-fold cross validation to classify three tissue types and obtain respective classification parameters for each tissue type. Each of the two steps is explained in detail below.

5.2.5.1 Multinomial logistic regression classification

A multinomial logistic regression (MLR) based generalized linear model[80] was used as a classification tool. Details of MLR method can be found in reference [80]. Briefly, MLR is an extension of binary logistic regression, where one of the outcomes is considered as a baseline, and odds ratio of other outcomes against the baseline are computed. Our problem consists of three possible outcomes, namely, PCa (Y = 0), nPZ (Y = 1) and BPH (Y = 2), where Y is an index that represents the nominal outcome. The MLR model can then be constructed to obtain a classifier for predicting the presence of cancer, as described by Eqs. (5.2)-(5.4)[80]:

$$P\left(Y=j\middle|x\right)=\frac{\mathrm{e}^{g_j(x)}}{\sum_{k=0}^{n}\mathrm{e}^{g_j(x)}} \tag{5.2}$$

$$g_j\left(x\right)=\ln\left(\frac{P\left(Y=j\right)}{P\left(Y=0\right)}\right)=\beta_{j0}+\beta_{j1}x_1+\ldots+\beta_{jn}x_n,\quad for\ j=1,2 \tag{5.3}$$

$$g_j\left(x\right)=0,\quad for\ j=0 \tag{5.4}$$

where $P(Y=j)$ represents the probability for outcome j; $g_j(x)$ is logit function; x_n is the n^{th} feature characteristically identified in either AFLS or LRS, and β_{jn} is the corresponding coefficient for the n^{th} parameter of the j^{th} model.

This model was implemented in Matlab[81] with the use of “mnrfit” function. A 10-fold cross validation method was used to calculate the classification parameters, as described below. First, the data was partitioned into 10 segments using ‘crossvalind’ function, while

making sure that each tissue type had equal distribution. One of the segments was chosen as test set and the rest as training set. Second, for a given training set, 'mnrfit' and 'mnrval' were used to compute probabilities P(Y=j), for each of three tissue type, j (Eq. (5.2)). Third, the three probability distributions were used to create an ROC for each tissue type (PCa, nPZ, BPH), followed by determination of Youden index[82] to obtain an optimum cut off value for the classification. Fourth, Sn, Sp and Acc of all three tissue classes were calculated on the test set. Fifth, steps one to four were repeated while selecting a different test set each time out of 10 partitions of data generated during cross validation process, and Sn, Sp, and Acc were averaged over the ten iterations. Similarly, an averaged value of AUC was also obtained for each set from all 10 ROC curves that were generated in cross validation. Finally, steps one to five were repeated 10 times, to obtain 10 independent performance evaluations of cross-validated classification parameters. Means and standard deviations of Sn, Sp, Acc and AUC were then calculated, across the 10 values of each obtained in the fourth step. A flow chart describing the ROC analysis is given in Fig. 5.2.

By selecting different sets of parameters or features, [x], in Eq. (5.2), the above classification algorithm was implemented to evaluate the ability of discriminating PCa by three methods: (a) AFLS-only, (b) LRS-only, and (c) *dMOD* with combined features of AFLS and LRS. For each of the three methods, a feature selection algorithm was first used to select a "best feature set" for classification, as further explained in the next section.

The above algorithm is for a 3-level classification, where there are 3 tissue types (PCa, nPZ, and BPH). A similar algorithm was implemented also for 5-level classification, where *j* in Eq. 5.2 varies from 0 to 4 instead of 0 to 2, the class levels are PCa (GS 9), PCa (GS 8), PCa (GS 7), nPZ and BPH.

5.2.5.2 Feature Selection

As described in Section 5.2.4, the measured data resulted in a large feature set, consisting of 6 features from LRS and 20 features from AFLS. However, all these features may

not contribute equally and constructively to the classification model, which was described in Section 5.2.5.1. Also, using a relatively large feature set could lead to the over-fitting problem for the classification model, especially for sparse datasets. A feature selection algorithm was therefore developed to select an optimum feature set from a given set of features: i.e., 6 in case of LRS, 20 in case of AFLM, and 26 (6+20) in case of *dMOD* method. In this study, a sequential feature selection algorithm was implemented in Matlab[81]. Sequential feature selection is a commonly used method for feature selection[83,84], and will only be briefly discussed here. In general, sequential feature selection involves adding [sequential forward selection (SFS)] or removing [sequential backward selection (SBS)] features, one at a time, to or from an empty/full feature set, and evaluates a given model using a chosen criterion. This process continues until adding or removing more features does not improve the model prediction, as defined by a specified criterion. Both SFS and SBS can be used independently as feature selection methods, and can produce varying results for different datasets.

I implemented both of these methods to select a set of features, along with two criteria, which gave a total of four independent "feature sets". The two criteria used to select significant features were: (a) In criterion A, I computed the deviance of the multinomial logistic regression model fit (mnrfit, see Section 5.2.5.1), and tested if the new deviance after adding/removing the new feature was significantly ($p < 0.05$; chi-square test) reduced. (b) In criterion B, I used the same multinomial model as in criterion A, but instead of using deviance, I utilized 10-fold cross validation to compute classification accuracy of cancer. The misclassification rate, computed using average of 10 test sets, was then used as the criterion value. If there was no decrease in the criterion value, the new feature was not added or removed for SFS or SBS, respectively. For more details, the interested reader can refer to the Matlab documentation for "*sequentialfs*" function[81].

Thus, for each initial feature set obtained from LRS, AFLS or LRS + AFLS, a total of four algorithms were implemented, based on the direction (SFS or SBS) and inclusion/exclusion

criteria (A or B), namely, SFS+A, SBS+A, SFS+B, and SBS+B. The four algorithms generated four independent sets of selected features, one out of which could be the "best feature set" determined by its best classification performance, as reflected through Sn, Sp, Acc, and AUC. Such best feature sets were selected for each of the three approaches: LRS-only, AFLS-only, and *dMOD*.

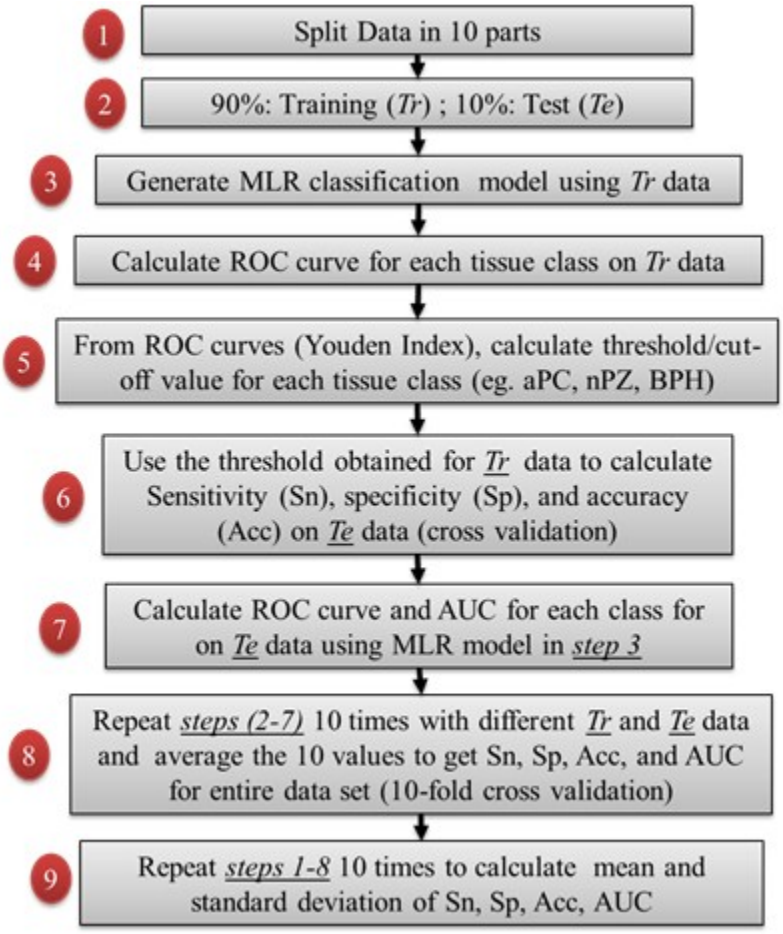

Fig. 5.2 An algorithm flow chart describing calculation of sensitivity (Sn), specificity (Sp), accuracy (Acc) and generation of ROC curves through cross-validated classification process.

5.3 Results

A total of 29 patients were enrolled in the study, of whom 6 were excluded from the final analysis after histologic evaluation revealed 25% or less PCa in the tissue evaluated. Clinical characteristics of the included 23 patients are shown in Table 5.1. Mean (SD) patient age was

60.7 (6.0) years. Several patients had multiple foci of PCa, resulting in 27 PCa regions measured from 23 different patients. As previously mentioned, multiple spectral measurements were obtained from each region yielding a total of 221 PCa, 176 nPZ and 142 BPH measurements (Table 5.2).

Table 5.1 Patient Characteristics*

Subject No.	Age	pre-treatment PSA	Primary Gleason grade	Secondary Gleason grade	Gleason sum	p stage	N stage
1	62	6.89	4	5	9	3a	0
2	68	7.9	4	5	9	3a	0
3	58	12.2	4	5	9	3b	1
4	53	3.2	4	5	9	3a	0
5	61	4.2	4	5	9	3b	0
6	69	5.7	4	4	8	3a	0
7	72	7.4	4	3	7	3b	0
8	56	5.9	4	4	8	2c	0
9	56	3.6	4	4	8	2c	0
10	54	6	4	3	7	3a	0
11	57	18	4	3	7	3b	0
12	48	6.1	4	3	7	3a	0
13	63	16.6	4	4	8	3b	0
14	66	2	3	4	7	2c	0
15	62	4.49	4	5	9	3a	0
16	55	3.2	3	4	7	3a	0
17	69	3.5	3	4	7	2c	0
18	64	2.7	4	4	8	3b	0
19	55	6.2	4	3	7	3a	x
20	64	4.9	4	3	7	2c	0
21	65	3.5	3	4	7	2c	0
22	60	3.1	3	4	7	2b	0
23	59	21.8	4	3	7	3b	0

* The Gleason sums presented here are based on whole prostate (final pathology), which matched the optically measured region in all cases except case 8, where measured region was Gleason 7 (4+3).

Of the 20 measured AFLS parameters, 16 showed statistically significant differences ($p<0.001$) between PCa vs nPZ in the multinomial logistic regression model while 19 showed

significant differences ($p<0.001$) between PCa vs BPH. As an example, Fig. 5.3(a) shows four of those parameters, representing mean-lifetimes (τ_m) at four emission wavelengths. It was observed that the mean-lifetimes of PCa at all four wavelengths were significantly longer than those of nPZ, but shorter than those of BPH at respective wavelengths.

Table 5.2 Number of measurements classified by tissue type*

	GS-7	GS-8	GS-9	Total
$N_{Subjects}$	13	4	6	**23**
$N_{Regions}$	15	5	7	**27**
N_{meas} **(PCa)**	125	40	56	**221**
N_{meas} **(nPZ)**	104	32	40	**176**
N_{meas} **(BPH)**	88	24	30	**142**

* For each column, values for nPZ and BPH reflect measurement from these regions from glands containing the Gleason sum classification shown.

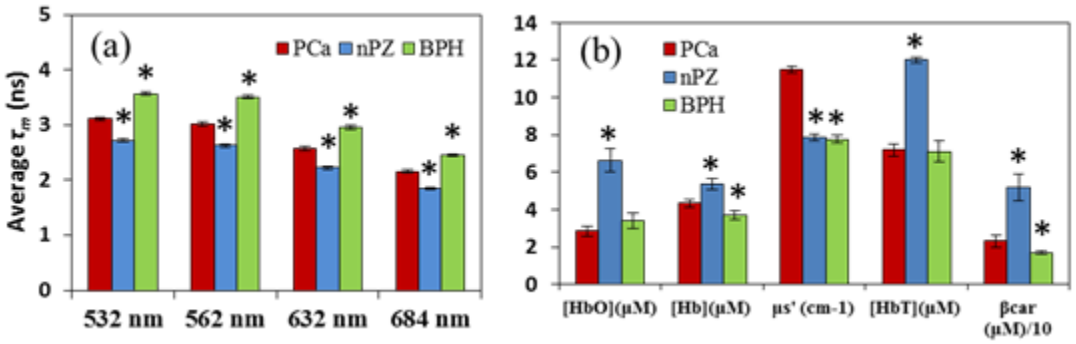

Fig. 5.3 (a) Comparison of four AFLS-derived features, mean-lifetimes, τ_m, at all four emission wavelengths across three tissue types. (b) Comparison of five LRS-derived features across three tissue types. μ_s' was calculated at 750 nm, and β_{car} is scaled down by a factor of 10 for display purposes. In both (a) and (b), the '*' above nPZ and BPH bars indicates significant difference ($p < 0.02$) when compared to PCa; error bars indicate standard error of mean.

Table 5.3 Classification metrics of PCa (all cancer grades combined) against non-cancer tissue types (nPZ and BPH).

Mode	Sensitivity	Specificity	Accuracy	AUC*100
AFLS	64.2 ± 2.5	69.2 ± 1.8	67.1 ± 0.7	72.9 ± 0.5
LRS	63.0 ± 1.5	82.9 ± 1.6	74.7 ± 1.0	80.4 ± 0.2
dMOD	79.0 ± 1.7	85.2 ± 1.1	**82.7 ± 0.7**	**90.8 ± 0.4**

In LRS analysis, 5 of 6 parameters showed significant differences ($p < 0.001$) between PCa vs nPZ, and 3 of 6 were significantly different ($p < 0.02$) between PCa vs BPH (Fig. 5.3b). Classification results are presented in Tables 3 & 4. Table 3 shows outcomes of the

classification analysis for PCa (all cancer grades combined) versus benign tissue types (nPZ+BPH), using AFLS and LRS parameters individually, and in combination (*dMOD*).

Table 5.4 Classification metrics of PCa graded by Gleason scores. The values listed in the left-most column implicate each PCa tissue group (e.g., GS 9) against rest of the tissue groups.

PCa Type	Mode	Sensitivity	Specificity	Accuracy	AUC*100
GS 9	*LRS*	84.4 ± 2.3	56.5 ± 0.7	59.4 ± 0.6	72.9 ± 0.5
	AFLS	76.5 ± 3.2	75.9 ± 1.0	76.0 ± 0.9	85.4 ± 0.6
	dMOD	82.3 ± 2.4	85.4 ± 0.7	**85.1 ± 0.6**	**91.5 ± 0.7**
GS 8	*LRS*	71.8 ± 2.6	72.6 ± 1.8	72.5 ± 1.6	77.1 ± 0.7
	AFLS	76.3 ± 4.9	86.7 ± 0.8	86.0 ± 0.6	90.0 ± 0.6
	dMOD	81.5 ± 3.4	90.8 ± 0.9	**90.1 ± 0.8**	**93.6 ± 0.7**
GS 7	*LRS*	71.9 ± 2.2	82.7 ± 1.3	80.2 ± 0.7	87.9 ± 0.2
	AFLS	70.9 ± 2.0	72.4 ± 0.9	72.1 ± 0.7	78.6 ± 0.7
	dMOD	86.0 ± 2.4	88.5 ± 0.7	**87.9 ± 0.6**	**94.7 ± 0.4**

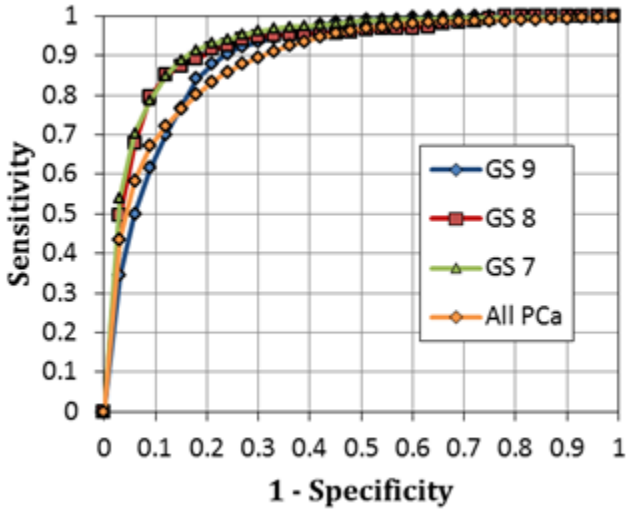

Fig. 5.4 ROC curves obtained using the *dMOD* and the MLR classification for identifying individual PCa grades (GS 9, GS 8, GS 7) and all grades combined (All PCa types).

Sensitivity, specificity, accuracy and AUC were found to be highest for *dMOD*. Table 5.4 shows outcomes of the ROC analysis for individual grades of PCa versus benign tissue types. For each tumor grade, overall accuracy and AUC were once again highest for *dMOD* among all methods. The ROC curves obtained using *dMOD* for individual cancer grades, as well as all cancers combined (All PCa) are plotted in Fig. 5.4.

Table 5.5 shows the "best feature set" that were selected for each classification category (3 Level and 5 Level), and each modality. Sequential forward selection with criterion A (SFS+A) method was found to be optimal for 3 level classification whereas sequential backward selection with criterion B (SBS+B) was found to be optimal for 5 level classification. It should also be noted that feature set of LRS was reduced to 5 from 6, because only 2 out of [HbO], [Hb], and [HbT], can be selected as independent parameters, and will lead to multicollinearity if all three are used. It can also be noted that in LRS only case, no feature selection method was used. This was because all four methods selected all the features during the run.

Table 5.5 Results of feature selection for each method in the two classification categories.

Classification	Modality	Feature Selection Method	Selected Features	No. of Features
3 Level	*dMOD*	SFS+A	[HbO], [Mel], μ_s',[β_{car}], HbT, 532 nm [τ_1, τ_2, τ_m, a_1, a_2], 562 nm [τ_1, τ_2, τ_m, a_1, a_2], 632 nm [τ_1, a_1], 684 nm [τ_1, τ_2, τ_m]	20/25
	AFLS	SFS+A	532 nm [τ_1, τ_m, a_1], 562 nm [τ_2, τ_m, a_1, a_2], 632 nm [τ_1, a_1, a_2], 684 nm [τ_1, τ_2, τ_m, a_1, a_2]	15/20
	LRS	none	[HbO], [Hb], [Mel], μ_s',[β_{car}]	5/5
5 Level	*dMOD*	SBS+B	[HbO], μ_s',[β_{car}],[HbT],532 nm [τ_1, τ_2, τ_m, a_2], 562 nm [τ_2, τ_m, a_1, a_2], 632 nm [τ_1, τ_m, a_1], 684 nm [τ_2, τ_m, a_2]	18/25
	AFLS	SBS+B	532 nm [τ_2, a_1, a_2], 562 nm [τ_1, τ_m, a_1, a_2], 632 nm [τ_1, τ_2, τ_m, a_1, a_2], 684 nm [τ_2, τ_m, a_1, a_2]	16/20
	LRS	none	[HbO], [HbT], [Mel], μ_s',[β_{car}]	5/5

5.4 Discussion and Conclusions

The results of this study suggest that both LRS and AFLS provide significant contrasts to detect or discriminate prostate cancer against non-cancer tissues (i.e., nPZ and BPH), as shown in Table 5.2. However, the accuracy is much improved when both modalities are used

together (*dMOD*), which could be expected, as each individual modality has distinct contrast parameters resulting from different physiological, morphological, and biochemical origins.

The contrast in LRS originates from changes in light absorption and scattering caused by prostate cancer tissues: light scattering is highly influenced by the cell size and density, whereas light absorption is closely related to various physiological markers, such as oxygenated and deoxygenated hemoglobin concentrations. By obtaining a wide-range (500-850 nm) reflectance spectrum, it is possible to decouple these properties and to quantify absolute values of respective physiological parameters, which can in turn serve as bio-markers and signatures of cancer. Specifically, nPZ showed a higher concentration of total hemoglobin (*[HbT]*) as compared to PCa (see Fig. 5.4(b)). This observation is consistent with a previous independent study by our group[85]. Additionally, light scattering (μ_s') was found to have a much higher value in PCa as compared to those retrieved in both nPZ and BPH. Although limited literature can be found on changes in physiological and morphological properties due to prostate cancer, my observation that prostate cancer leads to increased μ_s' and reduced [β_{car}] is consistent with a report given on breast cancer tissue[86].

In AFLS, the 447-nm excitation (with a 60-nm bandwidth) excited multiple endogenous fluorophores, i.e., flavins, prophyrins and lipo-pigments[52]. From Table 5.5 it can be observed that all four emission wavelengths provided contrast for classification. Therefore, all emission wavelengths used in the design are an essential part of the system to achieve the reported high accuracy (Table 5.3, 5.4). Considering spectral overlap in the emission spectra of these fluorophores, it is hard to determine which fluorophore has the biggest contribution in the determination of contrast, but the unanimity of the results across the emission range (Fig. 5.4) suggests that multiple fluorophores must contribute to the observed contrast (Fig. 3.7). This theory is also supported by the fact that a two component model provides an adequate fit. Although determination of exact biochemistry remains as a limitation of this study, it certainly provides a proof that biochemical environment pertaining to the given excitation-emission

domain significantly differs in prostate cancer and benign tissues, to provide an excellent contrast for tissue discrimination.

While studies and reports on methods designed towards discriminating prostate cancer tissues *in vivo* in a minimally invasive environment are limited, different approaches have been reported to address this issue, based on different methodologies[15,78]. Salomon et. al.[15] used a used a triple spectroscopy approach on frozen then thawed prostate tissue (16 malignant, 75 benign samples), to discriminate malignant tissue from benign tissue. They reported a cross validated sensitivity (Sn) and specificity (Sp) of 75% and 87.3%, respectively. Halter et. al.[78] measured electrical properties in a relatively large sample size (71 malignant, 465 benign). They reported tissue differentiation based on a detailed stratification by GS, also comparing the low grade cancer (GS < 7) to high grade (GS > 7). The maximum accuracy for GS 7 or greater was reported to be 81.8%. In comparison, an accuracy of 85 to 90% was obtained with *dMOD* (Table 5.4). This study also report the largest sample size utilized in comparative studies, making the results more robust.

In summary, the *dMOD* system, which combines auto-flourescence and light reflectance spectroscopy, discriminates between Gleason 7 or higher PCa and benign prostate tissue with excellent sensitivity, specificity and accuracy *ex vivo*. With further development, it has the potential to be used as: (a) an intraoperative aid for the assessment of adequate margins during radical prostatectomy; (b) to help improve the diagnostic yield of prostate biopsies, and (c) monitoring of tumor foci within the prostate during active surveillance.

CHAPTER 6

HUMAN EX VIVO PROSTATE STUDY: PART II

In Chapter 5, prostate cancer was successfully identified in presence of benign peripheral zone and benign prostate hyperplasia (transition zone) tissues. However, application of *dMOD* to intraoperative margin detection also requires the ability to distinguish prostate cancer from other benign extra-capsular tissues that line the prostate. Figure 6.1[87] shows an illustration of cancer spread in different stages. The cancer can spread out to the capsule and outer tissues in 3 of 4 of the stages. The extra-capsular tissues include bladder base muscle, prostate capsule, and urethra at the apex of prostate.

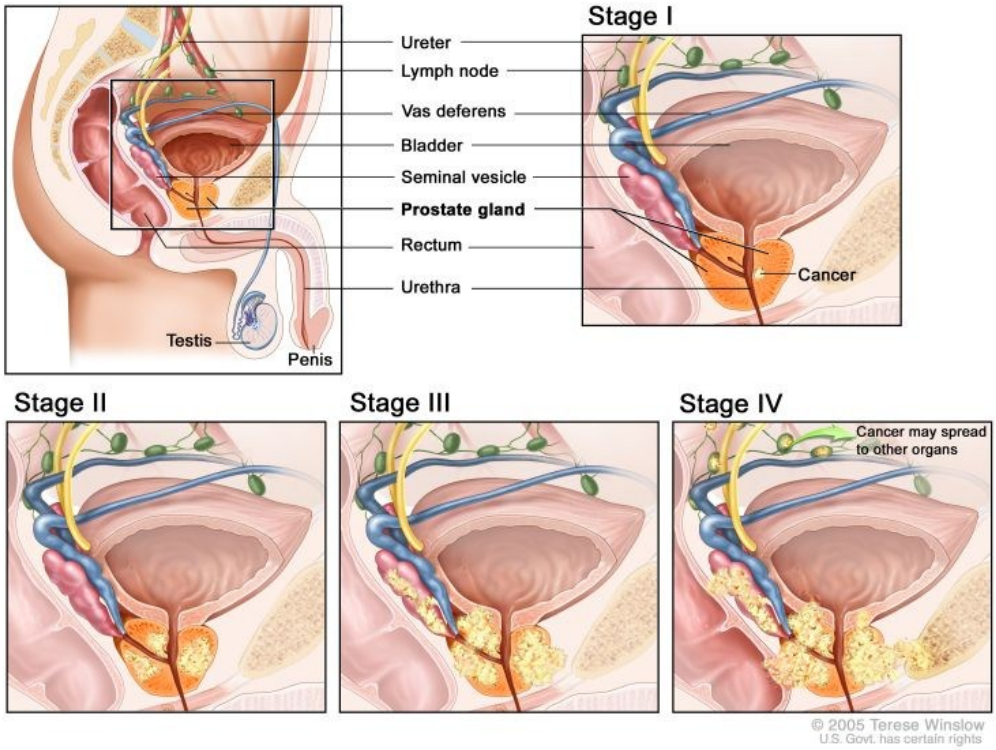

Fig. 6.1. An Illustration showing normal prostate (top left), and spread of prostate cancer during different stages. This illustrates how prostate cancer can spread out to the capsule, bladder and urethra, which poses a problem in obtaining clear margins during radical prostatectomy. (*Image Source*: Ohio State University Cancer Center website[87]).

6.1 Study protocol and sample size

In this study, 8 freshly resected radical prostatectomy samples were randomly selected for measurement. The measurement protocol followed was same as explained in Chapter 5, except that the prostate glands were measured before inking, since the surface was to be measured. Three types of extra capsular tissues (ECT) were measured, namely, bladder muscle at prostate base (BM), urethra at prostate apex (UT), and prostate capsule (CAP). For each prostate gland, one or more regions of each type were identified, and 5 optical readings were taken on each region. Table 6.1 shows a distribution of sample size.

Each of the measured regions was submitted to pathology for analysis and all the tissues were confirmed to be benign after histopathology examination. As can be seen from Table 6.1, a total of 185 locations were measured.

Table 6.1 The sample size distribution table for ECT study.

	No. of regions (data points)			
Subject	**BM**	**UR**	**CAP**	
1	1 (5)	1 (5)	3 (15)	
2	1 (5)	1 (5)	2 (10)	
3	2 (10)	1 (5)	2 (10)	
4	2 (10)	1 (5)	2 (10)	
5	1 (5)	1 (5)	2 (10)	
6	2 (10)	1 (5)	2 (10)	
7	1 (5)	1 (5)	2 (10)	
8	2 (10)	1 (5)	2 (10)	
Total	**60**	**40**	**85**	**N(ECT) = 185**

6.2 Data Analysis

The LRS and AFLM data was first quantified using the data analysis methods to extract 6 LRS ([HbO], [Hb], [HbT], [Mel], [β-car], and μ_s' at 750 nm) and 20 lifetime related AFLS parameters for each measured location, as described in Chapter 5.

Next, multinomial classification with 10-fold cross validation was performed to evaluate the accuracy of *dMOD* to discriminate PCa from ECTs, along with nPZ. As explained in Chapter 5, 3-level and 5-level classification was performed: in 3-level, the three tissue levels included PCa (n = 221) ,nPZ (n = 175) and ECT (n = 185); in 5-level classification, five levels included PCa (GS 9,n=56), PCa (GS 8, n=40), PCa (GS 7, n=125), nPZ(n=221) and ECT (n = 185). Therefore, 3-level classification tested the accuracy for identifying any type of high grade PCa in presence of benign ECTs, as well as nPZ tissue, whereas, 5-level classification tested the accuracy to identify high grade PCa by Gleason scores in presence of these benign tissues.

Table 6.2. Classification metrics depicting performance of *dMOD* in presence of ECTs.

	Type	Sensitivity	Specificity	Accuracy	AUC
3 Class	PCa	92.08 ± 1.03	92.42 ± 0.78	**92.29 ± 0.52**	0.98 ± 0.00
	nPZ	89.35 ± 1.01	94.13 ± 0.49	92.68 ± 0.24	0.98 ± 0.00
	ECT	99.13 ± 0.46	98.91 ± 0.27	98.98 ± 0.26	1.00 ± 0.00
5 Class	GS 9	82.80 ± 1.83	95.48 ± 0.46	**94.26 ± 0.49**	0.96 ± 0.01
	GS 8	83.50 ± 3.16	92.48 ± 0.25	**91.87 ± 0.28**	0.95 ± 0.01
	GS 7	91.44 ± 1.43	90.96 ± 0.34	**91.07 ± 0.26**	0.97 ± 0.00
	nPZ	92.00 ± 1.53	95.50 ± 0.53	94.44 ± 0.53	0.98 ± 0.00
	ECT	98.14 ± 0.70	99.59 ± 0.18	99.14 ± 0.20	1.00 ± 0.00

Table 6.3. Selected Features from both modalities for each classification routine

Classification Type	LRS	AFLM
3-level	*All 6 features*	*17/20 Features*: 532 nm (τ_2,τ_m,a_1,a_2); 562 nm (τ_1,τ_2,τ_m,a_2); 632 nm (τ_1,τ_2,τ_m,a_1,a_2); 684 (τ_1,τ_m,a_1,a_2)
5-level	*All 6 features*	*10/20 Features*: 532 nm (τ_1,τ_m,a_2); 562 nm (τ_1, a_2); 632 nm (τ_1,τ_2,τ_m, a_2); 684 (a_1)

6.3 Results and Discussion

From Table 6.2, it can be observed that *dMOD* provided excellent accuracy of above 90%, in discriminating PCa from benign ECT, both overall (92.29%) and by gleason scores (91.07% to 94.26%). In comparison, each modality alone did not perform as well (see Table

6.4), although the accuracy was still high for classifying combined PCa (82% AFLS, 87% LRS), and PCa by GS (78-91% AFLS, and 78-82% LRS). It can also be seen that when stratified by grade, AFLS provides very high accuracy of approx. 91% for both GS 9 and GS 8, which is comparable to the values obtained by *dMOD*. However, the accuracy for identifying GS 7 is much better in case of *dMOD*, once again justifying the use of dual-modality approach for prostate cancer diagnosis.

Table 6.4 Classification results for individual modalities. For LRS, all parameters were used for classification. AFLS used 16/20 in 5-level and 11/20 in 3-level classification.

5 -level		**Sensitivity**	**Specificity**	**Accuracy**	**AUC**
AFLS	**GS9**	88.07 ± 2.65	91.70 + 0.23	**91.36 + 0.36**	0.95 + 0.01
	GS8	76.75 + 2.06	92.32 + 0.32	**91.25 + 0.33**	0.93 + 0.01
	GS7	83.34 + 1.20	75.97 + 0.90	**77.54 + 0.73**	0.88 + 0.00
LRS	**GS9**	80.17 ± 2.04	78.17 + 0.46	**78.35 + 0.33**	0.85 + 0.01
	GS8	70.25 + 5.33	79.72 + 0.77	**79.07 + 0.75**	0.81 + 0.00
	GS7	87.06 + 2.26	80.43 + 1.02	**81.84 + 0.78**	0.92 + 0.00
3 -level		**Sensitivity**	**Specificity**	**Accuracy**	**AUC**
AFLS	**PCa**	86.60+1.66	79.37+1.15	**82.12+0.79**	0.92+0.00
LRS		76.67+0.49	92.62+0.73	**86.55+0.39**	0.93+0.00

The corresponding ROC curves pertaining to the classification using *dMOD* are shown in Fig. 6.2. For each algorithm, the features/parameters were also selected in each case based on the feature selection algorithm described in Chapter 5. As can be seen from Table 6.3, 23 features were used for 5-level classification, and 16 features were used for 3-level classification. All parameters from LRS were used in each case, and in case of AFLS, at least one parameter from each emission wavelength was used, suggesting no redundancy in design.

The accuracy observed here for detecting cancer in presence of extra-prostatic tissues, which applies to margin assessment during radical prostatectomy, is superior to that obtained in presence of transition zone tissue (BPH) in Chapter 5, which is more applicable to biopsy

application. The results in this strongly suggest that *dMOD* is an excellent tool for margin assessment during prostatectomy, thus improving the prostate cancer treatment approach.

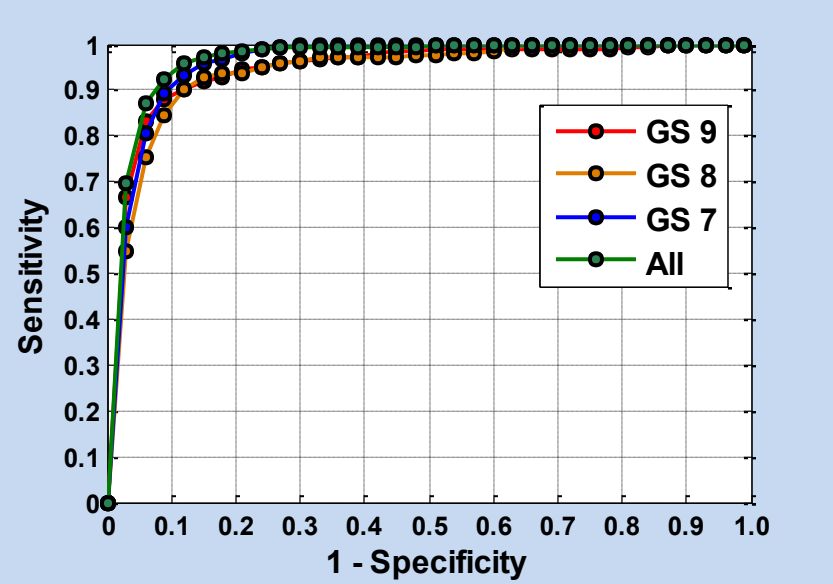

Fig. 6.2 ROC Curves obtained for different Gleason scores (GS 9, GS 8 and GS 7) using 5-level classification algorithm, and for all cancers (All), using 3-level classification algorithm.

In future work, *in vivo* evaluation of *dMOD* is warranted, where the results will be contingent upon the contrast alteration due to change in tissue perfusion. However, *in vivo* studies on animal models are supportive of *dMOD's in vivo* applicability. In addition, there may be other types of extra-prostatic tissues that need to be considered like pedicles and nerve bundles. Also, while a 1 mm fiber optic probe seems ideal for a biopsy set-up, the probe will have to be modified for margin assessment in a laparoscopic setting. In an ideal case, a thick fiber probe, possibly involving multiple channels, that covers a surface area of ~ 5mm diameter would make an excellent margin assessment tool. One possible design would be to have an array of source detector fibers in a probe, which can be alternately illuminated/detected using fiber optic multiplexer/s.

This chapter concludes the studies on prostate cancer detection. In the next chapter, the applicability of *dMOD* towards human breast cancer is discussed.

CHAPTER 7

APPLICATION TO BREAST CANCER DETECTION

dMOD works on the basic principles that probe the morphology and biochemistry of the localized tissue. Therefore, it would not be improbable to extrapolate that *dMOD* can be applied to discriminate other cancer types. In this chapter, the application of *dMOD* to detect breast cancer in the localized tissue was explored, which presents a critical clinical need, i.e., intraoperative margin detection.

7.1 Introduction

Breast cancer is one of the most common forms of cancers among American women with an estimated 230,480 new cases and 39,520 deaths in 2011[2]. With the advancement in diagnostic techniques, it is now possible to diagnose breast cancer in early stages while it is still localized. A standard treatment procedure for women with early breast cancer is breast conserving therapy[88], a surgical procedure known as the lumpectomy (or partial mastectomy) followed by irradiation therapy. Surgery is imminent in treating breast cancer, with many early stage patients being cured without recurrence. The goals of the surgery include complete resection of the primary tumor, with negative margins to reduce the risk of local recurrences. However, due to lack of definitive tools for intra operative assessment of cancer margin during lumpectomy, there is incidence of positive margins in 20-50% of patients who undergo the procedure[89,90]. Patients with positive margins must undergo a second surgery, leading to higher risk of wound infection, associated psychological distress, compromised cosmesis, and added medical expenses. Hence, an accurate diagnostic tool that helps in assessing these margins intra operatively is essential.

Many optical techniques have been evaluated for diagnosing breast cancer for more than a decade[91]. In particular, auto-fluorescence spectroscopy (AFS) and diffuse reflectance

spectroscopy (DRS) [also termed light reflectance spectroscopy (LRS)] have been developed and extensively evaluated by multiple groups of researchers to achieve clinically relevant results for cancer demarcation[20,53-55,86,92,93]. Many of these studies were focused on breast cancer: some were focused on the detection of breast cancer for clinical diagnosis[20,53,54,92]; some others were focused on the surgical margin detection[55,86,93]. Brown et. al.[86] recently developed a fiber-based DRS imaging system for breast cancer margin detection, with an overall sensitivity and specificity of 79.4% and 66.7%, respectively. Around the same time, Keller et. al.[55] evaluated DRS and AFS for using a point based approach with sensitivity and specificity of 85% and 96%, respectively, while also demonstrating the feasibility of converting the point based approach into an imaging system for larger area assessment.

In this feasibility study, I wish to explore the optical characteristics of AFLS and LRS of breast cancer in order to determine if LRS can serve either as a stand-alone method or as a combined approach with AFLS for breast cancer detection and classification. A protocol was designed to obtain measurements from freshly excised breast samples. A fiber optic probe of 1 mm diameter was utilized in collecting AFLS and LRS from human ex vivo breast specimens of 7 cases with invasive ductal carcinoma (IDC). Three tissue types were measured, namely, IDC, benign fibrous tissue (FT) and adipose tissue (AT).

The motivation and goal of this pilot study was to examine the feasibility of finding optical pre-biomarkers through each or both of the two optical modalities that could serve as intrinsic classifiers for IDC, which is the most common form of breast cancer in lumpectomies. If such pre-biomarkers can be found in a prompt time frame, this methodology may have a potential to become a quick assessment tool for accurate detection of positive breast cancer margins during breast conserving surgery.

7.2 Methods

The instrumentation used was the same (*dMOD*) as in case of prostate ex vivo study, as described in previous chapters.

7.2.1 Measurement protocol and Sample Size

AFLM and LRS readings of human breast cancer specimens were acquired at The University of Texas Southwestern (UTSW) Medical Center, Dallas, TX. The optical measurement protocols were compliant with the UTSW IRB requirements. The data were collected ex vivo from the breast specimens immediately after their resections through mastectomies or lumpectomies. Selection criteria for this pilot study included tissue samples with biopsy confirmed IDC, with no prior exposure to chemotherapy, and having a tumor size of 5 mm in at-least one dimension confirmed via imaging history. Seven such breast cases were selected for collecting optical measurements.

Prior to measurement, the excised breast samples were inked at the margins by the pathologist as per standard pathology protocol. Based on the surgical markings on the sample, multiple cuts were made across the breast tissue, and the tumor was located visually; Fig. 7.1(c) shows an example. Further, after the pathologist visually identified regions of cancer tissue, benign fibrous tissue, and adipose tissue, multiple (approximately 3-6) AFLM and LRS readings were obtained on each of the three pathological regions. AFLM and LRS readings were taken sequentially (in no particular order) at each measurement point. The integration time was for AFLM was 5 sec per emission wavelength for IDC and FT, and 10 sec per emission wavelength for AT. For LRS measurements, up to 100 ms integration times were used. With manual switching between the two modalities, the acquisition time was about 60 sec per measured point. After data acquisition, the measured regions (i.e., three pathological types of tissues) were marked with ink, sliced out from the rest of the breast tissue, and sent for histological analysis. The corresponding histology results for all of the specimens sent were later obtained, confirming 100% correctness in initial identification of breast cancer versus benign tissues. According to the histology results, the measured optical points were categorized as cancer or controls.

One of the 7 cases was excluded from the analysis due to contamination from Isosulphan Blue, a surgical dye commonly used to trace the lymphatic drainage during surgery. The presence of the dye in this case was confirmed by the occurrence of an odd spectral feature around 570 nm - 650 nm in the LRS data[94]. Therefore, a total of 93 locations across 6 breast cancer cases were measured: 34 from IDC regions, 31 from FT regions and 28 from AT regions.

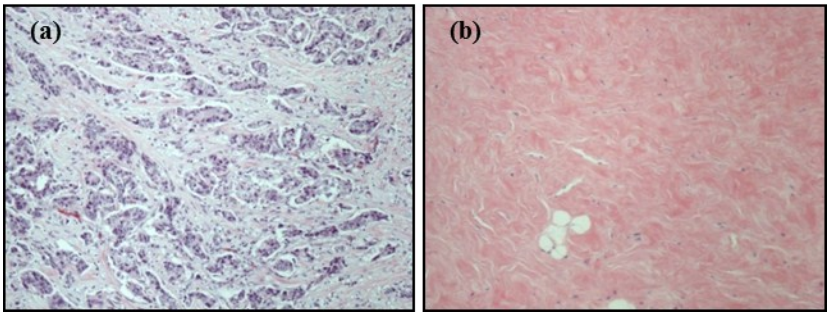

Fig. 7.1: Histological findings showing an example of histological difference between (a) invasive ductal carcinoma and (b) benign breast stroma in pink color.

Figure 7.1(a) is a histopathology illustration of invasive ductal carcinoma showing malignant infiltrative ducts with blue cellular nuclei in a background of abundant purplish stroma. The tumor can be viewed differently from normal breast tissue on physical examination as well as histomorphological evaluation. The overall histological alteration is evident, from a homogeneous stroma, as seen in Fig. 7.1(b), and two-layer epithelium ductal structure, not shown here, to a highly heterogeneous stroma admixed with many disorganized ducts, as demonstrated in Fig. 7.1(a).

7.2.2 Data Analysis

7.2.2.1 AFLS Analysis

The data analysis for AFLS was same as described previously for in Chapter 3 (please see Section 3.3). Briefly, each lifetime curve was fitted with a two-component exponent model, to obtain two lifetimes, τ_1, and τ_2, and their respective weights, $\mathbf{a_1}$ and $\mathbf{a_2}$. Integral-intensity-weighted mean lifetime (τ_m) was also calculated, generating 5 usable contrast parameters per

emission wavelength. Since there are four emission curves per measured locations, overall 20 (5X4) parameters were obtained at each location. Each of these parameters were then evaluated for statistical differences between IDC and AT, as well as IDC and FT, using a linear mixed model analysis for repeated measures, implemented in SAS.

7.2.2.2 LRS Analysis

For LRS data analysis, a different empirical approach was implemented, compared to quantification approach described previously. Each acquired LRS spectrum was divided by the calibration reflectance spectrum obtained from a diffuse reflectance standard (WS-1, Ocean Optics, FL, USA). While the acquired LRS included data from 475-1100 nm, we selected the spectral segments between 500-840 nm for further analysis. This selection was based on the quantification algorithms described in Chapter 2, which covers major absorbers including hemoglobin[59], and the fact that the signal to noise ratio of the system falls off outside this range. However, it is possible to include the wavelengths beyond 500-840 nm in the analysis. Given the chosen spectral region, each spectrum was divided into multiple 20-nm segments [as marked by dashed lines in Fig. 7.3(a)]. A spectral slope of each region was calculated using linear regression, resulting in 17 slopes (S1 to S17) for each measured spectrum: S1 representing the slope in 500-520 nm region, S2 representing the slope in 520-540 nm region, and so on. Each slope was then compared among all three breast tissue types, followed by statistical significance tests using linear mixed model regression analysis.

7.2.2.3 Classification and ROC analysis

The classification ability of each of the three methods, namely, LRS only, AFLS only, and *dMOD* were assessed independently. Among these multiple parameters/features were available for classification using each method: 17 slopes for LRS, 20 fluorescence lifetime parameters for AFLS, and a combination of both, 37 (17 + 20) for *dMOD*. As we have observed in Chapter 5, feature selection is an essential process which provides a best set of features that can provide improved classification, based on certain criteria. This works especially well in

cases where the data matrix is sparse, which means that the number of features is comparable to the number of observations (or data points), or typically less than 5 times the number of observations.

As explained in Section 5.2.5, the feature selection was achieved using one of the four methods involving two feature selection algorithms and two independent selection criteria: [SFA+A, SFS+B, SBS+A, SBS+B]. The selected features were used for classification of three tissue types (IDC, AT and FT) using the 3-level multinomial logistic regression algorithm (see Section 5.2.5). The Sensitivity (Sn), specificity (Sp), accuracy (Acc) and area under the curve (AUC) for the receiver operating curve were obtained as classification metrics, for each of the three methods.

7.3 Results

7.3.1 AFLS Results

Each lifetime curve was used to obtain 4 fitted parameters (τ_1, τ_2, $\mathbf{a_1}$ and $\mathbf{a_2}$) and a derived parameter (τ_m). With four emission wavelengths, overall 20 AFLS parameters were obtained from each measured location.

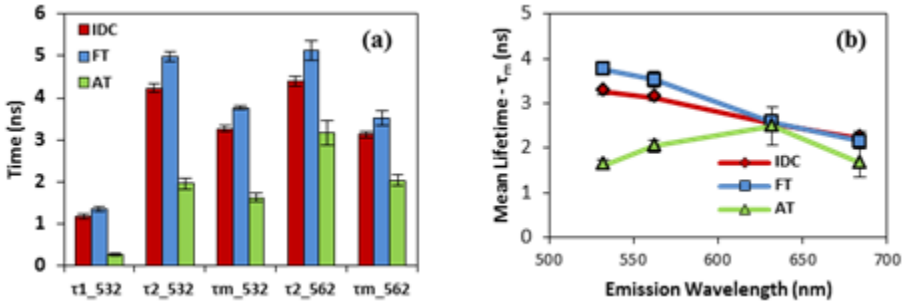

Fig. 7.2 (a) Mean AFLS parameters that showed a significant difference between IDC (n=34) and FT (n=31), as well as IDC and AT (n=28). (b) Average of τ_m plotted for all three tissue types as a function of emission wavelength. . The error bars in both (a) and (b) represent standard error of the mean.

A mixed model repeated measures linear regression analysis was performed, revealing significant differences between means of cancer and the other two types of breast tissue, in 5 out of 20 AFLM parameters, as seen in Fig. 7.2(a). The p-values associated with all 5 significant

AFLM features are tabulated in Table 7.1. All these significant parameters were derived from emission wavelengths 532 nm and 562 nm. Among the rest of the parameters, some showed significant differences either between IDC and FT or between IDC and AT, but not differentiating IDC from both FT and AF, whereas some did not show any significant difference among any tissue types.

As shown in Fig. 7.2(a), IDC lifetimes were overall found to be shorter than those of FT, and longer than those of AT. Figure 7.2(b) shows the variation of mean lifetimes as a function of wavelength, for the three tissue types. As can be seen, the τ_m values of IDC and FT are similar in their spectral trends across wavelength, but exhibit stark contrast at first two emission wavelengths. AT, on the other hand, follows a different mean lifetime pattern over the emission spectral range, with an increased then followed by a decreased τ_m; nevertheless, τ_m of AT still shows even more significant contrast at 532 nm and 562 nm, with respect to the τ_m values of both IDC and FT.

Table 7.1: The p-values of significant features of both modalities, derived from mixed model regression analysis for test of significant differences between IDC and other two breast tissue types. 'λ' represents wavelength.

LRS Features λ range (nm)	IDC vs. FT	IDC vs. AT	LRS Feature λ range (nm)	IDC vs. FT	IDC vs. AT	AFLM Features	IDC vs. FT	IDC vs. AT
S1 (500-520)	0.001	< 0.001	**S13 (740-760)**	< 0.001	< 0.001	**τ_1_532nm**	0.022	< 0.001
S3 (540-560)	< 0.001	< 0.001	**S14 (760-780)**	0.01	< 0.001	**τ_2_532nm**	< 0.001	< 0.001
S4 (560-580)	< 0.001	0.052	**S15 (780-800)**	0.003	< 0.001	**τ_m_532nm**	< 0.001	< 0.001
S7 (620-640)	0.03	< 0.001	**S16 (800-820)**	< 0.001	< 0.001	**τ_2_562nm**	0.012	0.001
S12 (720-740)	0.004	< 0.001	**S17 (820-840)**	< 0.001	< 0.001	**τ_m_562nm**	0.032	< 0.001

7.3.2 LRS Results

Figure 7.3(a) shows a comparison of mean LRS spectra of the three breast tissue types. As described previously in Section 7.2.2.2, 17 spectral windows of 20 nm width were generated (as marked by dotted vertical lines); corresponding spectral slope of each region was

computed for all the data points using a linear regression curve fit, giving us overall 17 parameters to compare IDC with FT and AT. Statistical significance was tested using a mixed model repeated measures analysis model, which revealed that 10 out of 17 mean spectral slopes was significantly different between IDC and the other two types of breast tissues (*note*: S4 is marginally significant for IDC vs. AT with p = 0.052). The p-values of these significant features have been tabulated in Table 7.1. As an example, Fig. 7.3(b) shows a comparison of scaled slopes (slope x 10^3) among the three breast tissue types at several spectral windows, whose slopes are statistically different between IDC and the other two tissue types. Note that S12 to S17 shared similar slope patterns for all three breast tissue types, so only slope values of S13 among those are plotted in Fig. 7.3(b). It was also observed that within S12 to S17, IDC has the maximum absolute slope values as compared to FT and AT.

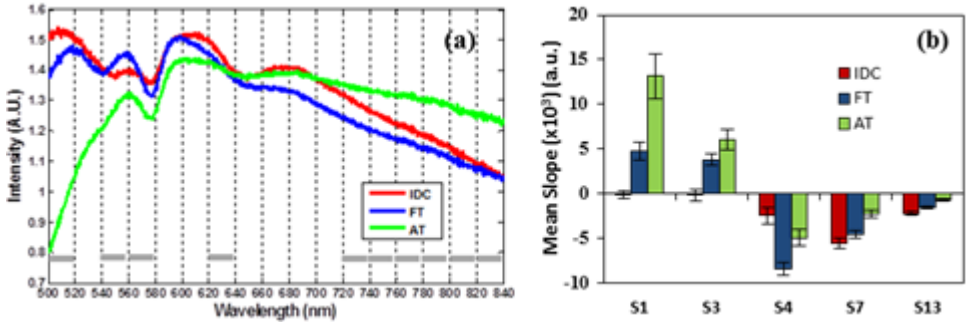

Fig. 7.3 (a) Average reflectance spectra of IDC (n=34), FT (n=31) and AT (n=28). Vertical black lines indicate the 20-nm spectral windows (S1-S17) selected for spectral slope analysis. The gray bars on the bottom of figure mark the spectral windows whose spectral slopes are significantly different between IDC and two other types of breast tissue. (b) Means of scaled spectral slopes (Slope x 10^3) along with standard errors, for 5 selected spectral regions, which showed a significant difference between IDC and the other two breast tissue types.

7.3.3 Classification Results

While statistical analyses given in Sections 7.3.1 and 7.3.2 showed 5 and 10 significant features in AFLM and LRS, respectively, I still fed all the features (i.e., 20 in case of AFLS, 17 in case of LRS, and 37 for both) as input parameters to the feature selection algorithm. The underlying reason is that the feature selection algorithm has an ability to identify unique features which otherwise may not be significantly different among classes, but add value to the

classification of data. Specifically, as described earlier in Section 7.2.2.3, classification ability was assessed for three cases: (a) AFLS only, (b) LRS only, and (c) *dMOD* (i.e., LRS + AFLS together). In each of these three cases, a best set of features was selected from one of the four feature selection methods. For AFLS only, "*SFS + A"* gave the best feature set that included [τ_1 (532 nm), τ_m (532 nm), τ_1 (562 nm), and τ_2 (562 nm)]. For LRS only, the best results were obtained using "*SBS + B"* feature selection routine, and the selected feature set consisted of [S1, S5, S6, S7, S8, S9, S17]. Similarly, for *dMOD*, the routine used was *"SBS + B"*, and the selected feature set was [τ_2 (562 nm), a_1 (562 nm), a_2 (562 nm), S1, S8, S9, S14, S17].

Table 7.2. Classification statistics obtained using three methods: (a) AFLS-only, (b) LRS-only, (c) *dMOD* method.

Modality	Tissue Type	Sensitivity (%)	Specificity (%)	Accuracy (%)	AUC
LRS	IDC	93.8 ± 1.3	98.0 ± 1.0	**96.4 ± 0.8**	1.00
	FT	82.3 ± 6.1	82.8 ± 2.6	82.6 ± 2.3	0.96
	AT	77.3 ± 4.2	88.8 ± 3.0	85.6 ± 2.1	0.96
AFLM	IDC	89.8 ± 2.1	93.8 ± 1.9	**92.3 ± 0.8**	0.99
	FT	90.0 ± 1.6	95.2 ± 0.6	93.5 ± 0.6	0.97
	AT	91.8 ± 2.0	100.0 ± 0	97.5 ± 0.6	0.98
dMOD	IDC	91.4 ± 3.4	98.6 ± 1.1	**96.0 ± 1.3**	1.00
	FT	87.3 ± 4.1	93.6 ± 1.2	91.6 ± 1.1	1.00
	AT	86.0 ± 2.1	94.4 ± 2.0	92.0 ± 1.7	1.00

Interestingly, classification model utilizes certain features which otherwise may not be significantly different among classes, but add value to the classification of data, for example, S8, S9, a_1 (562 nm), a_2 (562 nm). The four parameters (Sn, Sp, Acc, AUC) that summarize the classification ability are tabulated in Table 7.2 for each case. As can be clearly observed, the accuracy of classifying IDC is greater than 90% using any of the three cases, i.e., either technique alone, or in combination. In fact, the best accuracy for cancer detection in this study is for LRS alone (96.4±0.8) which is quite close to both methods used together (96.0±1.3). AFLS provides slightly better results for the other two tissue classes, when compared with LRS and the combined technique.

7.4 Discussion and Conclusions

Changes in cellular metabolism caused by cancer development in vivo can result from a number of factors including genetic changes, changes in tissue vascularization, and changes in metabolic demand[57,95]. Flavins (co-enzymes) that are involved in cellular oxidative phosphorylation[96], porphyrins, and lipo-pigments were the targeted auto-fluorophores in this study for AFLM measurements. At 447 nm excitation, it was found that the mean auto-fluorescence lifetimes quantified by the two exponential components were significantly different between IDC and two other types of benign breast tissue, predominantly at 532 nm and 562 nm. This implies that the detected fluorescence signals stem mainly from flavins and lipo-pigments[52,96]. Also, there were significant differences within the LRS between the cancerous and benign breast tissue, in the predominantly hemoglobin absorption range (500-640 nm), as well as in predominantly scattering domain (700-840 nm) (see Table 7.1). These findings are consistent with previously published work[20,53-55], as well as with the expected morphology of cancer.

In this study, I chose a relatively straightforward and empirical approach for LRS data analysis (i.e., quantification of segmented spectral slopes), as opposed to model-based or feature-extraction algorithms that quantify physiological and other feature-based parameters. The spectral slopes are light-intensity independent, and do not require frequent calibration of the instrument, thus making the measurement and tissue classification faster, simpler, with a lower computational cost. In particular, empirical approaches may be practically useful to extract distinct characteristics due to cancer when non-contact imaging-based approaches (e.g., multi-spectral imaging) are utilized. In these cases, there often exist spectral broadening and other factors that lead to low-resolution spectra[55] and thus make model-based fitting difficult or inaccurate. The classification results that I obtained (see Table 7.2) are comparable to the ones published using absolute-quantification methods[54,86,92,93] and other empirical methods[20,55]. Therefore, while the sample size of the breast specimens in this pilot study is relatively limited

(n=6), the results from LRS are consistent and convincing to show that a simple, empirical approach using selected spectral slopes can provide high sensitivity and specificity to identify IDC.

Both AFLS and LRS methods independently provided contrast parameters to differentiate IDC from benign breast tissue types, with excellent accuracy (see Table 7.2). LRS was found to be the most robust and accurate (Acc = 96.4±0.8 %) in IDC identification in this implementation. However, AFLS was not too far (Acc = 92.3±0.8 %) in accuracy, and provided better accuracies when being used to identify other two classes of breast tissues. Nevertheless, it can be argued that "high accuracy in identifying IDC" would be a better qualifier when we select a cancer-detection method. Thus, LRS would be a preferred approach over the others (i.e., AFLS and *dMOD*) since it provides highest accuracy for IDC discrimination in the given sample set. It is also observed from Table 7.2 that *dMOD* approach does not significantly improve the results. It should be noted however, that there are multitudes of methods available for data classification and feature selection, and application of other methods may provide slightly different results.

As shown in Section 7.3.1, integral-intensity-weighted mean lifetimes at 532 nm for cancer, fibrous and adipose tissue were 3.27±0.43 ns, 3.77±0.25 ns, and 1.62±0.57 ns, respectively. There has been limited report in literature on lifetimes of fresh breast tissues, especially with excitation near 450 nm. However, these results are comparable to a previous report on lifetimes of IDC and fibroadenoma[79]. There are various endogenous fluorophores that could be excited within 400-500 nm range; their lifetimes range from <0.01 ns for protein bound FAD at the shorter end, and up to 15 ns for protoporphyrin IX at the longer end [31]. It is thus difficult to determine the individual fluorophores that are exactly responsible for the two lifetime components.

In Sections 7.3.1 and 7.3.2, 5 AFLM and 10 LRS features were identified that showed statistical significance ($p < 0.05$) between breast cancer and other breast tissue types (i.e.,

fibrous and adipose tissues). It is important, however, to point out that some of the significant ($p<0.05$) features may not contribute uniquely to the classification model in a separate or combined LRS, AFLM or LRS + AFLM case, possibly due to multi-collinearity. Namely, a set of individually significant contrast features may not form the best feature set for tissue classification. Therefore, in Section 7.3.3, I still utilized all the parameters (20 for AFLM, 17 for LRS and 37 for LRS+AFLM) for feature selection. Feature selection algorithms then revealed a reduced set of features (4 for AFLM, 7 for LRS, and 8 for LRS+AFLM), including some features that were found to be statistically different between cancer and other two types, and some additional features which were not. In addition, to account for overfitting, we also used a 10-fold cross validation routine, and the results were evaluated on the test data, which was separate from training data.

The short-term goal of this study was to examine and demonstrate the feasibility of identifying and predicting IDC based on ex vivo breast tissue samples using AFLS, LRS, or combined approaches. The long term goal of this investigation is to assess LRS and AFLS for clinical translation towards breast cancer margin detection. Among three possible methods, this study suggests that LRS is a highly sensitive and accurate technique to differentiate a solid IDC mass from surrounding fibrous tissue or adipose tissue with a localized point measurement. However, there are other tissue types in the breast that need to be evaluated or identified besides IDC, such as preneoplastic proliferative changes (pre-cancer) and ductal carcinoma in situ (DCIS). Again, a continuous study is warranted in order to develop a more comprehensive and robust classification algorithm for identification of normal, pre-cancer, DCIS, and IDC. Such a study may also allow us to take into account the demographics of patients in analysis[93], including the population with prior chemotherapy[55]. Surgical margin detection would rather require an imaging platform for fast surface assessment of excised samples. Both LRS and AFLS have the ability to be implemented in a non-contact imaging geometry, and the data (Table 7.2) suggest either of these methods could be a useful tool. A larger pool of breast tissue

specimens involving the rest of the tissue types may provide an insight into the clear dominance of either technique, but for now, LRS displays an edge over AFLS given cost as a consideration factor.

CHAPTER 8

DISCUSSION AND FUTURE SCOPE

A dual-modality optical device was successfully developed and evaluated *in vivo* on animal models of prostate cancer, as well as on *ex vivo* human prostate gland. While multiple research groups have explored these two modalities individually for various types of cancers in human and animal models, my approach is unique in multiple ways. Firstly, the implementation of quantification algorithm in LRS is novel to this research. Secondly, the excitation-emission design used in AFLS is also novel, and is a relatively less explored region in fluorescence based cancer detection, targeting flavins, porphyrins and lipo-pigments. Lastly, there are limited or no reports in literature for these methods towards prostate cancer detection especially in human tissue.

Recently, few studies have been reported towards the detection of prostate cancer *ex vivo* in human prostate tissue[15,76-78], using either multimodality approach of combining fluorescence spectroscopy, white light reflectance and high-frequency impedance measurement[15], or electrical properties of prostate tissue[76-78]. Table 8.1 shows a comparison of current work with the previously published studies. The accuracy obtained using *dMOD* is comparable or better than reported works. In addition, this work includes transition zone tissue (BPH) in the classification, and extra-capsular tissues, which makes the results more robust both for optical biopsy for prostate cancer diagnosis, and intra-operative margin assessment during radical prostatectomy for improved surgical outcome. Lastly, in an optical biopsy set-up a probe diameter of 1mm, used in this study, is more compatible, along with a better spatial sampling accuracy.

It should be noted that in the animal studies (Chapter 4), and in case of breast cancer (Chapter 7), either optical method (LRS or AFLS) proved to be sufficient for cancer

discrimination. However, in case of human prostate cancer study (Chapters 5 & 6), either modality alone provided insufficient contrast, in comparison to *dMOD*. This justifies the use of dual-modality technique for detection of prostate cancer in humans. This also suggests that prostate cancer is a harder problem to solve, which is evident from the fact that non-invasive imaging modalities are still under development for a robust diagnosis of prostate cancer. On the other hand, animal models are certainly more aggressive as compared to naturally growing human prostate cancer, providing enough contrast to be differentiated using single modality. Similarly, small lesions in breast cancer are also identified easily with X-ray imaging modalities indicating a good contrast, which was consistent with our finding. In fact, there have been several studies in the literature using LRS-like set-up for breast cancer detection [20,55,86].

Table 8.1 Comparison of current work with major competing studies (ICT = intra capsular prostatic tissue; ECT – extra capsular tissues)

	Current Work (2012)	**Halter et. al., 2011**	**Salomon et. al., 2009**
***Ex vivo* Sample condition**	Fresh (Within 2 Hours of resection)	Fresh (exact time not specified)	Frozen fresh, then thawed later for measurement
Sample size	PCa (221 [GS-7 (125); GS-8 (40); GS-9 (56)]) Benign 503 [PZ (176) TZ (142), ECT (185)])	PCa (71 [GS-6 (28);GS-7 (28); GS-8 (13); GS-9 (2)]) Benign (465)	79(PCa), 16 (Benign)
Results **[AUC** = area under ROC curve; **Sn** = Sensitivity **Sp** = Specificity**]**	**ICT: AUC (Sn/Sp)** All = 0.91(79/85%) GS-7 = 0.95 (86/89%) GS-8 = 0.94 (82/91%) GS-9 = 0.92 (82/85%)	**AUC** All = 0.82 Low Grade = 0.8 High grade = 0.9	**Sn/Sp =** 87.3/75%
	ECT: AUC (Sn/Sp) All = 0.98(92/92%) GS-7 = 0.97 (91/91%) GS-8 = 0.95 (83/92%) GS-9 = 0.96 (83/95%)		
Tissues identified	GS-7,8,9; Benign [nPZ, BPH (TZ), ECT]	GS-6,7,8,9; Benign	PCa, non-PCa
Cancer Stratification?	Yes	Yes	No
Sampled area / sampling resolution (diameter)	< 1 mm	3.5 mm	Not reported

The animal studies were conducted *in vivo*, whereas the human studies were conducted *ex vivo* in this research. One of the main differences in these two scenarios is blood perfusion. While changes in oxygen saturation and hemoglobin concentrations are highly affected by blood perfusion, one can expect scattering to change less. A comparison of scattering coefficient in both scenarios reveals that in comparison to benign control tissue, scattering coefficient decreases in tumor tissue for subcutaneous rat model (Fig.4.4) as well as for mice orthotopic model (Fig.4.10). However, a reverse effect is observed in human *ex vivo* study (Fig. 5.3), where scattering coefficient is larger in cancer tissue compared to benign tissues.

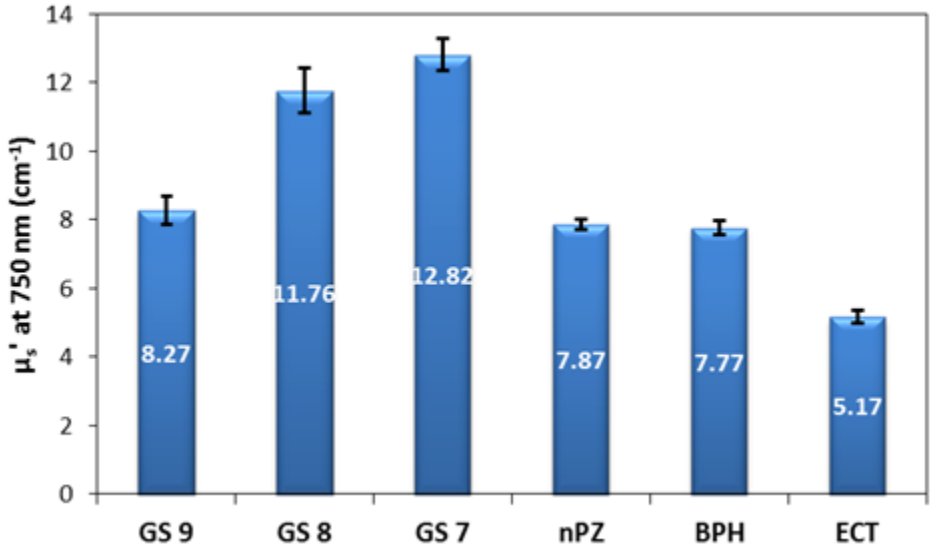

Fig. 8.1 A comparison of scattering coefficient for different prostate cancer, benign prostatic and extra-prostatic tissues. Bars represent the mean across all measured points, and error bars represent standard error of mean.

Since animal models of prostate cancer usually present a very aggressive form of prostate cancer, it would be interesting to compare scattering coefficient by Gleason scores/grades. Interestingly, Fig. 8.1 shows that the scattering coefficient decreases as the tumor becomes more aggressive. Specifically, scattering coefficient of GS 7 > GS 8 > GS 9, which is comparable to intra-prostatic benign tissues (nPZ and BPH) in this case. Although this

does not completely explain why scattering coefficient in animal models is lower, the observation does seem to follow the logic that more aggressive the cancer is, the lower the scattering.

Another interesting observation that can be made from the results of this study is that different contrast parameters were obtained in different models of cancer, especially for AFLS. For instance, in rat ectopic model study, mean-lifetime (τ_m) was the major classifier, whereas in mice orthotopic model study, the first lifetime component (τ_1), was the major classifier, whereas τ_m did not exhibit much contrast. Similarly, whereas most of the 20 lifetime parameters exhibited contrast in case of prostate cancer, only a few (mainly for 532 nm and 562 nm emission) showed contrast for breast tissue. Although it is difficult to determine the exact biochemical differences that lead to variability in AFLS contrast in different cancer models, their environment is expected to be different given the difference in origin of the cancer types. This observation certainly illustrates how sensitive AFLS technique is to various tissues, residing in distinct biochemical environments.

8.1 Limitations and Future Scope

While the results obtained in this research are promising, there are various translational steps required for *dMOD* to be realized as a clinical tool. These points are listed below:

a) The human prostate study was performed ex vivo, within 2 hours of the resection. In an in vivo setting, these parameters could be expected to change which could either enhance or diminish the contrast. In vivo study of human prostate is warranted to explore this issue.
b) Four emission wavelengths were initially used for AFLS, to determine the best combination of wavelengths based on contrast obtained. The results suggest that unlike animal in-vivo studies, where even one emission wavelength is sufficient, all four emission wavelengths contribute to the tissue discrimination in humans. Since switching of emission filter increases the acquisition time, a time multiplexing approach could be implemented in AFLS for data faster acquisition[97].

c) LRS acquisition is currently in milliseconds, but the data processing algorithms require much iteration and are not real time. Implementation on dedicated processors or alternatively exploring empirical methods of LRS analysis as shown in Chapter 7 is warranted for clinical applicability.

d) To develop a better understanding of contribution of various fluorophores (flavins, porphyrins and lipo-pigments) probed, a multi-band excitation-emission protocol would enhance the understanding of contrast observed.

e) Practical implementation of *dMOD* for prostate biopsy, would require a motorized set-up, similar to one described in Chapter 1 (Fig. 1.3). Similarly, for intraoperative margin detection, a thicker probe, with a 5mm diameter field of view would be more appropriate, which would require either a multiplexing, or scanning approach to be implemented in hardware, to increase the current field of view, which is less than 1mm.

f) A contact measurement probe is always susceptible to pressure related changes, and it is important to account for those. Studies have shown that while AFLS is not very sensitive to small pressure changes[98], LRS readings can be heavily affected by pressure applied on the tissue[99,100]. An independent study conducted using *dMOD* (please see Appendix A) was also consistent with these findings. Therefore, incorporating a pressure sensor at the tip of fiber optic probe with real-time pressure feedback should enhance the diagnostic ability of *dMOD*.

APPENDIX A

EFFECT OF PROBE PRESSURE ON OPTICAL PROPERTIES

Measurements with a fiber optic probe such as the one in *dMOD* require contact with the tissue, which may induce pressure onto the tissue under investigation, based on the application geometry. In my study, I used an optical frame that held the weight of the probe, and gently place the probe on tissue surface to avoid pressure related changes. Additionally, the sample size used in this study is large, and should average out the inconsistencies related to pressure. However, it is important to understand how different pressures may affect the measured optical properties. In the past, a few groups have investigated the effect of probe pressure on the tissues for both LRS[99,100] and fluorescence measurements[98,100].

Here, I investigated the pressure effect that could possibly exist in *dMOD* measurements. I used three different types of animal tissue from a fresh meat market, with different structural appearances, as shown in Fig. A1. To measure pressure, I placed the probe on a manual linear stage, with a resolution of 0.001 inches (see Fig. A2).

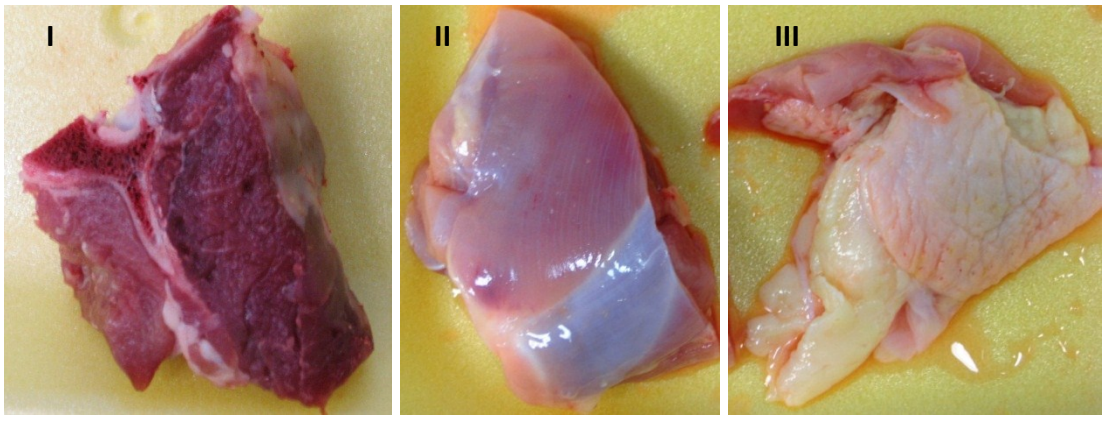

Fig. A1. Tissue types measured: (I) Lamb muscle; (II) Chicken thigh muscle; (III) Chicken Skin and soft tissue

The tissue was placed on a weighing scale, which had a resolution of 0.01 grams. The probe was first placed slightly above the tissue, and then lowered 0.005 or 0.01 at a time. 3 locations on each tissue type were measured, and 10 pressure readings were 10 readings were taken, lowering the probe by 0.005 or 0.01 inches per iteration. At each point, the gram weight

was noted, which was later converted to Newtons (N) (1 g = 0.0098 N). Pressure (in N/mm^2) was also calculated by dividing Newton force by area of the probe, which was $1mm^2$.

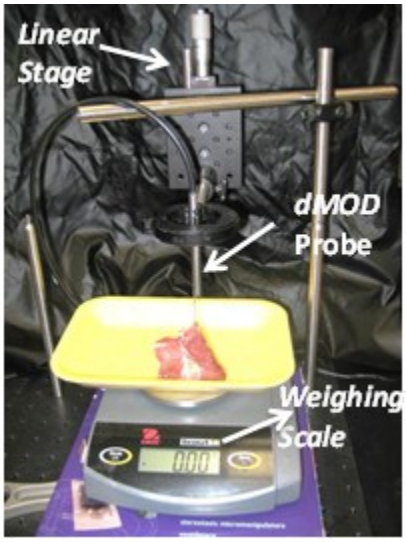

Fig. A2. Experimental set-up for pressure measurements.

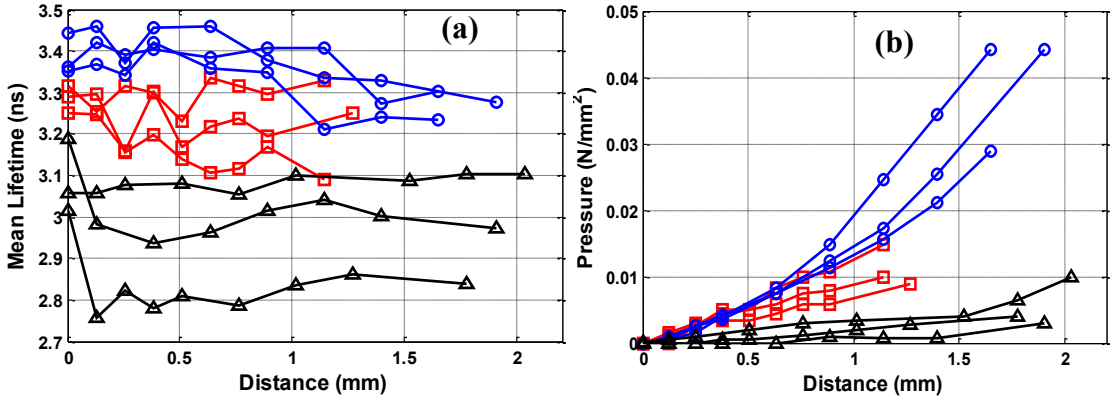

Fig. A3. Results for AFLS experiment. In both plots, red lines = tissue Type I, blue lines = tissue Type II, black lines = tissue Type III. (a) Mean lifetime (τ_m) at 562 nm as a function of distance pushed down from surface. (b) Change in pressure against plotted against the distance travelled by the probe from tissue surface.

AFLS Results:

For AFLS, τ_m at 562 nm is shown in Fig. A3(a) as a function of distance from surface. It can be seen that there is no relationship between mean lifetime and distance from surface for tissue types I and III. However, for Tissue type II, there a slight change is observed after 1 mm,

which is of the order of ~200 ps. Comparing the pressure against distance for Type II in Fig. A3(b) suggests that this may be due to higher pressures (> 0.02 N/mm^2) observed after 1 mm. It can also be observed from Fig. A3(b) that pressure perceived by the tissue also depends on the tissue type, with lowest perception by the soft tissue. In other words, the placement of the probe on a soft tissue (Type III) is less prone to induce pressure related changes, as compared to a harder tissue (Type I or II). Results from 562 nm have been presented here, because the signal to noise ratio was the highest for 562 nm. However, other wavelengths demonstrated similar results.

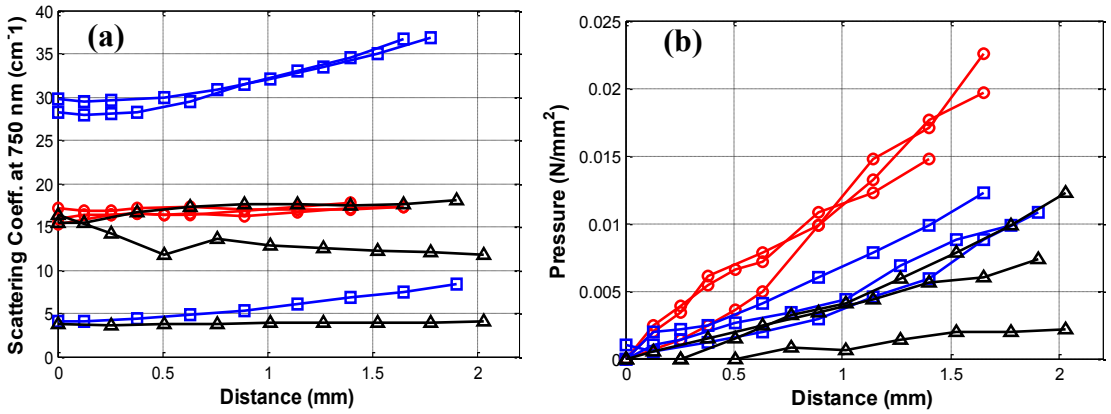

Fig. A4. Results for LRS experiment. In both plots, red lines = tissue Type I, blue lines = tissue Type II, black lines = tissue Type III. (a) μ_s' at 750 nm as a function of distance pushed down from tissue surface. (b) Change in pressure against plotted against the distance travelled by the probe from tissue surface.

LRS Results:

LRS experiments were carried out on a different set of tissues, although similar in categories to Type I, II and III described in Fig. A1. The data fitting algorithm was used to extract μ_s', [HbO], and [Hb]. As evident from Fig. A4(b), tissue Type II (blue lines) was relatively soft in comparison to the Type II measured for AFLS. Fig. A4(a) shows the effect of probe distance on scattering coefficient (μ_s'). It can be seen that while Type I and Type III do not exhibit a definite pattern or dependency on distance, Type II shows a linear increase in

scattering after approx. 0.6-0.7 mm, which corresponds to pressures of greater than 0.005 N/mm^2.

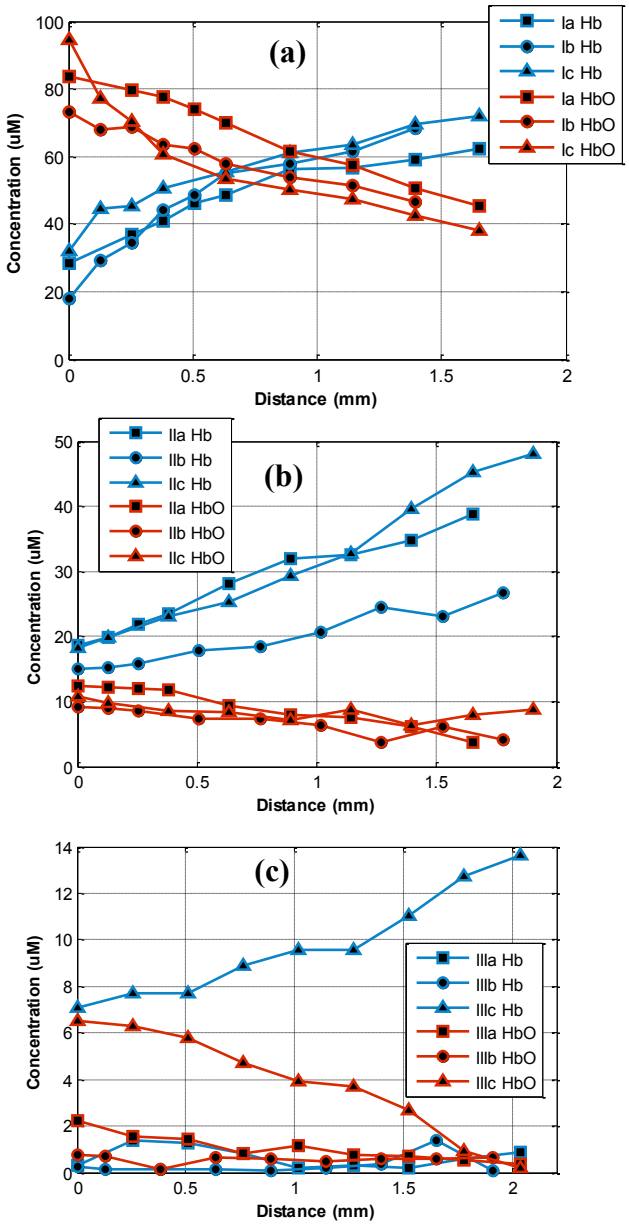

Fig. A5. Effect of probe distance from tissue surface on [Hb] (blue) and [HbO] (red) for (a) tissue Type I, (b) tissue Type II, and (c) tissue Type III.

Fig. A5 shows the effect of probe placement on hemoglobin concentrations ([Hb] and [HbO] for all three tissue types. There is a strong linear relationship between change in hemoglobin and probe placement. In all three tissue types, which possess different baseline levels of hemoglobin to start with, a similar trend is observed showing an increase in [Hb] and decrease in [HbO] indicating a decrease in oxygen saturation.

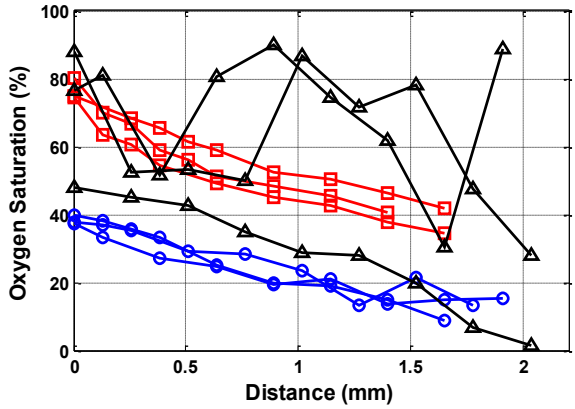

Fig. A6. Oxygen Saturation as a function of probe distance from surface for tissue types I (red), II (blue) and III (black).

Table A1. Linear Fit statistics for curves in Fig. B6.

Tissue	R-squared	Slope	Intercept
Ia	0.9796	-19.5	72.66
Ib	0.8986	-25.83	72.83
Ic	0.9166	-21.36	66.8
IIa	0.9772	-18.82	39.59
IIb	0.8988	-14.07	37.86
IIc	0.8802	-11.57	33.45
IIIa	0.169	-12.02	73.97
IIIb	0.0431	-5.96	75.96
IIIc	0.9577	-23.22	51.92

Fig. A6 shows changes in oxygen saturation, with the probe distance. A decrease in saturation is observed in all curves, except in tissues IIIa and IIIb, where the hemoglobin levels are extremely low (see Fig. A5). Also, except for IIIa and IIIb, which exhibit a noisy saturation

behavior (Fig. A6), the relationship is largely linear with distance, as evident from R-square values in Table A1.

Discussion and Conclusions:

The results obtained here indicate that when using a thin fiber optic probe in contact with the tissue, the perceived pressure on the tissue varies in different tissue types, and in general is perceived less for softer tissue types. AFLS measurements seem to be almost insensitive to the probe pressures up to 0.02 N/mm^2, after which a small linear effect can be observed. These findings are also consistent with previously published work by Nath et. al.,[98] which suggested that "pressure does not significantly affect fluorescence intensity or lineshape".

In case of LRS, a decrease in oxygen saturation was observed along with the increase in scattering coefficient, which is consistent with the previously published work by Reif et. al.[99]. However, Reif et. al. reported a much slower decrease in oxygen saturation (less than 10% per 0.05 N/mm^2), which is much smaller than observed here. One possible reason could be that they measured tissue in vivo, where the dynamics were different. Another possible explanation is that they quantified the pressure based on weight applied to the probe, whereas here the perceived pressure is measured by weighing the tissue under pressure. It has been demonstrated in Fig. A3(b) and A4(b), that perceived pressure can vary based on tissue type. Lastly, the diameter of the probe used in this study is much smaller (1 mm compared to 2.7 mm), which could lead to different dynamic changes. However, this needs to be investigated further for any definitive reasoning.

In context of the studies conducted in this thesis, the probe placement was simulated on different tissue types blindly, and the gram-weight was measured to assess the possible pressures induced on prostate tissues during the measurement. It was found that the gram-weight ranged from 0 to 0.5 g in most cases, with up to 0.8 g in a few cases. In terms of pressure, this corresponds to a maximum of 0.008 N/mm^2. Thus, while AFLS measurements

should not be affected by pressure, this could cause some variability in LRS measurements, especially [Hb] and [HbO] which appear to be highly sensitive to small changes in pressure. This conclusion is also supported by high standard deviations observed in case of LRS as compared to AFLS, as shown in Table A2.

Table A2. Mean and standard deviations of various AFLS and LRS parameters for PCa (all cancers combined)

	LRS			AFLS	
	[HbO]	**[Hb]**	**μ_s' (750 nm)**	**τ_m(532 nm)**	**τ_m(562 nm)**
Mean (PCa)	2.853882	4.335498	11.47353	3.123961	4.280118
Standard Deviation	4.00564	3.185203	5.006287	0.43747	0.759722
% Deviation	140.3576	73.46798	43.63338	14.00369	17.75002

This study suggests that including a measure for the pressure on the probe tip may help increase the sensitivity of the technique, since pressure seems to affect the optical parameters in a predictable manner, especially in case of LRS. Also, for margin assessment application, it is possible to increase the probe surface area, which can reduce the overall pressure on tissue, when same force is applied[100].

REFERENCES

1. Jemal, A. et al. Cancer statistics, 2009. *CA Cancer J Clin* **59**, 225-49 (2009).
2. American Cancer, S. Cancer Facts & Figures 2011. *Atlanta* (2011).
3. Heidenreich, A. et al. [EAU guidelines on prostate cancer]. *Actas Urol Esp* **33**, 113-26 (2009).
4. Gleason, D.F. & Mellinger, G.T. Prediction of prognosis for prostatic adenocarcinoma by combined histological grading and clinical staging. *J. Urol* **111**, 58-64 (1974).
5. Burger, M., Steginga, S., Williams, S. & Gardiner Robert A, R. Prostate Cancer. *Endocrinology of male reproduction* (2006).
6. Delongchamps, N.B. & Haas, G.P. Saturation biopsies for prostate cancer: current uses and future prospects. *Nat Rev Urol* **6**, 645-52 (2009).
7. Rocco, B. et al. Sensitivity and detection rate of a 12-core trans-perineal prostate biopsy: preliminary report. *Eur. Urol* **49**, 827-33 (2006).
8. Patel, U. TRUS and prostate biopsy: current status. *Prostate Cancer Prostatic Dis* **7**, 208-10 (2004).

9. Descazeaud, A. et al. Saturation biopsy protocol enhances prediction of pT3 and surgical margin status on prostatectomy specimen. *World J Urol* **24**, 676-80 (2006).

10. Jones, J.S. et al. Saturation technique does not improve cancer detection as an initial prostate biopsy strategy. *J. Urol* **175**, 485-8 (2006).

11. Pushkar, .D. & Govorov, .A. Re: Saturation technique does not improve cancer detection as an initial prostate biopsy strategy - Jones JS, Patel A, Schoenfield L, Rabets JC, Zippe CD, Magi-Galluzzi C - J Urol 2006;175 : 485-8. *European Urology* **50**, 157-158 (2006).

12. Unknown, OPTICALLY GUIDED NEEDLE BIOPSY SYSTEM USING MULTI-MODAL SPECTROSCOPY. (2011).

13. Berger, A.P. et al. Complication rate of transrectal ultrasound guided prostate biopsy: a comparison among 3 protocols with 6, 10 and 15 cores. *J. Urol* **171**, 1478-80; discussion 1480-1 (2004).

14. Pinkhasov, G.I. et al. Complications following prostate needle biopsy requiring hospital admission or emergency department visits - experience from 1000 consecutive cases. *BJU international* (2012).doi:10.1111/j.1464-410X.2011.10926.x

15. Salomon, G. et al. The feasibility of prostate cancer detection by triple spectroscopy. *Eur. Urol* **55**, 376-83 (2009).

16. Yossepowitch, O. et al. Positive surgical margins in radical prostatectomy: outlining the problem and its long-term consequences. *Eur. Urol* **55**, 87-99 (2009).

17. Wieder, J.A. & Soloway, M.S. Incidence, etiology, location, prevention and treatment of positive surgical margins after radical prostatectomy for prostate cancer. *J. Urol* **160**, 299-315 (1998).

18. Sammon, J.D. et al. Risk factors for biochemical recurrence following radical perineal prostatectomy in a large contemporary series: A detailed assessment of margin extent and location. *Urologic oncology* (2012).doi:10.1016/j.urolonc.2012.03.013

19. Giller, C.A., Liu, H., German, D.C., Kashyap, D. & Dewey, R.B. A stereotactic near-infrared probe for localization during functional neurosurgical procedures: further experience. *J Neurosurg* **110**, 263-73 (2009).

20. Bigio, I.J. et al. Diagnosis of breast cancer using elastic-scattering spectroscopy: preliminary clinical results. *J Biomed Opt* **5**, 221-8 (2000).

21. Perelman, .L.T. et al. Observation of periodic fine structure in reflectance from biological tissue: A new technique for measuring nuclear size distribution. *Physical Review Letters* **80**, 627-630 (1998).

22. Utzinger, U. et al. Reflectance spectroscopy for in vivo characterization of ovarian tissue. *Lasers Surg Med* **28**, 56-66 (2001).

23. Zonios, G. & Dimou, A. Modeling diffuse reflectance from semi-infinite turbid media: application to the study of skin optical properties. *Opt Express* **14**, 8661-74 (2006).

24. Izuishi, .K. et al. The histological basis of detection of adenoma and cancer in the colon by autofluorescence endoscopic imaging. *Endoscopy* **31**, 511-516 (1999).

25. RICHARDSKORTUM, .R. et al. SPECTROSCOPIC DIAGNOSIS OF COLONIC DYSPLASIA. *Photochemistry And Photobiology* **53**, 777-786 (1991).

26. McGinty, J. et al. Wide-field fluorescence lifetime imaging of cancer. *Biomed Opt Express* **1**, 627-640 (2010).

27. Munro, I. et al. Toward the clinical application of time-domain fluorescence lifetime imaging. *J Biomed Opt* **10**, 051403 (2005).

28. Backman, V. et al. Detection of preinvasive cancer cells. *Nature* **406**, 35-6 (2000).

29. Zonios, G. & Dimou, A. Optical properties of human melanocytic nevi in vivo. *Photochem Photobiol* **85**, 298-303 (2009).

30. Radhakrishnan, H., Senapati, A., Kashyap, D., Peng, Y.B. & Liu, H. Light scattering from rat nervous system measured intraoperatively by

near-infrared reflectance spectroscopy. *J Biomed Opt* **10**, 051405 (2005).

31. Liu, H. et al. Near infrared and visible spectroscopic measurements to detect changes in light scattering and hemoglobin oxygen saturation from rat spinal cord during peripheral stimulation. *NeuroImage* **40**, 217-27 (2008).

32. Johns, M. & Liu, H. Limited possibility for quantifying mean particle size by logarithmic light-scattering spectroscopy. *Applied Optics* **42**, 2968-2971 (2003).

33. Graaff, R. et al. Reduced Light Scattering Properties for Mixtures of spherical particles: a simple approximation derived from Mie calculations. *Applied Optics* **31**, 1370-1376 (1992).

34. Zonios, G. & Dimou, A. Light scattering spectroscopy of human skin in vivo. *Opt Express* **17**, 1256-67 (2009).

35. Kashyap, D. Development of a Broadband Multi-Channel NIRS System for Quantifying Absolute Concentrations of Hemoglobin Derivatives and reduced scattering Coefficients. *Thesis dissertation* (2007).

36. Ocean Optics, I. USB2000 Fiber optic spectrometer: Installation and Operation Manual. (2005).

37. Zijlstra, W.G., Buursma, A. & Assendelft, O.W. *Visible and Near-infrared Absorption Spectra of Human and Animal Hemoglobin: Determination and Application* (VSP: 2000).

38. van Staveren, H.J., Moes, C.J.M., van Marie, J., Prahl, S.A. & van Gemert, M.J.C. Light scattering in Intralipid-10% in the wavelength range of 400GÇô1100 nm. Ap*plied Optics 3*0**,** 4507-4514 (1991).

39. Online Brochure: http://www.iss.com/products/oxiplex/oxiplexTS.pdf. (0).

40. Matcher, S.J., Cope, M. & Delpy, D.T. Use of the water absorption spectrum to quantify tissue chromophore concentration changes in near-infrared spectroscopy. Ph*ys Med Biol 3*9**,** 177-96 (1994).

41. Spector, L. Ad*vances in Genetic Programming (*1999).

42. Ashlock, D. Ev*olutionary Computation for Modeling And Optimization (*2006).

43. Eiben, A. & Smith, J. In*troduction to Evolutionary Computing (*2003).

44. Dorigo, M., Maniezzo, V. & Colorni, A. Ant system: optimization by a colony of cooperating agents. IE*EE Trans Syst Man Cybern B Cybern 2*6**,** 29-41 (1996).

45. Franceschini, M.A., Gratton, E. & Fantini, S. Noninvasive optical method of measuring tissue and arterial saturation: an application to absolute pulse oximetry of the brain. Op*t Lett 2*4**,** 829-31 (1999).

46. Hueber, D.M. et al. Non-invasive and quantitative near-infrared haemoglobin spectrometry in the piglet brain during hypoxic stress, using a frequency-domain multidistance instrument. Ph*ys Med Biol 4*6**,** 41-62 (2001).

47. Dugdale, D.C. Hemoglobin. 20**10,** (2010).

48. Mitsuharu, M., Yukio, U., Britton, C., Britton, C. & Robert, A.R. Development of time-resolved spectroscopy system for quantitative noninvasive tissue measurement. 23**89,** 142-149 (1995).

49. Zonios, G. & Dimou, A. Melanin optical properties provide evidence for chemical and structural disorder in vivo. Op*t Express 1*6**,** 8263-8 (2008).

50. Sharma, V. et al. Optical reflectance spectroscopy for detection of human prostate cancer. Co*nf Proc IEEE Eng Med Biol Soc 2*0**09,** 118-21 (2009).

51. Sharma, V., He, J.W., Narvenkar, S., Peng, Y.B. & Liu, H. Quantification of light reflectance spectroscopy and its application: determination of hemodynamics on the rat spinal cord and brain induced by electrical stimulation. Ne*uroimage 5*6**,** 1316-28 (2011).

52. Wagnieres, G.A., Star, W.M. & Wilson, B.C. In vivo fluorescence spectroscopy and imaging for oncological applications. Ph*otochem Photobiol 6*8**,** 603-32 (1998).

53. Palmer, G.M. et al. Comparison of multiexcitation fluorescence and diffuse reflectance spectroscopy for the diagnosis of breast cancer (March 2003). IE*EE Transactions on Biomedical Engineering 5*0**,** 1233-1242 (2003).

54. Volynskaya, Z. et al. Diagnosing breast cancer using diffuse reflectance spectroscopy and intrinsic fluorescence spectroscopy. J *Biomed Opt 1*3**,** 024012 (2008).

55. Keller, M.D. et al. Autofluorescence and diffuse reflectance spectroscopy and spectral imaging for breast surgical margin analysis. La*sers Surg Med 4*2**,** 15-23 (2010).

56. Skala, M.C. et al. In vivo multiphoton fluorescence lifetime imaging of protein-bound and free nicotinamide adenine dinucleotide in normal and precancerous epithelia. J *Biomed Opt 1*2**,** 024014 (2007).

57. Chen, H.M., Chiang, C.P., You, C., Hsiao, T.C. & Wang, C.Y. Time-resolved autofluorescence spectroscopy for classifying normal and premalignant oral tissues. La*sers Surg Med 3*7**,** 37-45 (2005).

58. Tadrous, P.J. et al. Fluorescence lifetime imaging of unstained tissues: early results in human breast cancer. J *Pathol 1*9**9,** 309-17 (2003).

59. Sharma, V. et al. A dual-modality optical biopsy approach for in vivo detection of prostate cancer in rat model. JI*OHS 4*, 269-277 (2011).

60. Sharma, V. et al. Auto-fluorescence lifetime and light reflectance spectroscopy for breast cancer diagnosis: potential tools for intraoperative margin detection. Bi*omed. Opt. Express 3*, 1825-1840 (2012).

61. Lakowicz, J. Pr*inciples of Fluorescence Spectroscopy (*2006).

62. Mycek, M.A., Schomacker, K.T. & Nishioka, N.S. Colonic polyp differentiation using time-resolved autofluorescence spectroscopy. Ga*strointest. Endosc 4*8**,** 390-4 (1998).

63. Marcu, L. et al. Fluorescence lifetime spectroscopy of glioblastoma multiforme. Ph*otochem. Photobiol 8*0**,** 98-103 (2004).

64. Siegel, J. et al. Studying biological tissue with fluorescence lifetime imaging: microscopy, endoscopy, and complex decay profiles. Ap*plied Optics 4*2**,** 2995-3004 (2003).

65. Braslavsky, .S.E. Glossary of terms used in Photochemistry 3(rd) Edition (IUPAC Recommendations 2006). Pu*re And Applied Chemistry 7*9**,** 293-465 (2007).

66. Stokes, G. On the refrangibility of light. Ph*il. Trans. Royal Soc. London 1*4**2,** 463-562 (1852).

67. Valeur, .B. & Berberan-Santos, .M.N. A Brief History of Fluorescence and Phosphorescence before the Emergence of Quantum Theory. Jo*urnal Of Chemical Education 8*8**,** 731-738 (2011).

68. Herman, B., Lakowicz, J., Murphy, D., Fellers, T. & Davidson, M. Fluorescence Excitation and Emission Fundamentals. (2009).

69. Berezin, M.Y. & Achilefu, S. Fluorescence lifetime measurements and biological imaging. Ch*em Rev 1*1**0,** 2641-84 (2010).

70. Mukerjee, A. et al. Spectroscopic properties of curcumin: orientation of transition moments. J *Phys Chem B 1*1**4,** 12679-84 (2010).

71. Luchowski, R. et al. Instrument response standard in time-resolved fluorescence. Re*v Sci Instrum 8*0**,** 033109 (2009).

72. Gunn, S. Support Vector Machines for Classification and Regression. Te*chnical Report, Image Speech and Intelligent Systems Research Group, University of Southampton* (1998).

73. Vaupel, P. & Mayer, A. Hypoxia in cancer: significance and impact on clinical outcome. Ca*ncer Metastasis Rev 2*6**,** 225-39 (2007).

74. Conn, P. So*urcebook of Models for Biomedical Research (*2008).

75. Kommu, S.S., Andrews, R.J. & Mah, R.W. Real-time multiple microsensor tissue recognition and its potential application in the management of prostate cancer. BJ*U Int 9*7**,** 222-3 (2006).

76. Halter, R.J., Schned, A., Heaney, J., Hartov, A. & Paulsen, K.D. Electrical properties of prostatic tissues: I. Single frequency admittivity properties. J. *Urol 1*8**2,** 1600-7 (2009).

77. Halter, R.J., Schned, A., Heaney, J., Hartov, A. & Paulsen, K.D. Electrical properties of prostatic tissues: II. Spectral admittivity properties. J. *Urol 18***2,** 1608-13 (2009).

78. Halter, R.J., Schned, A.R., Heaney, J.A. & Hartov, A. Passive bioelectrical properties for assessing high- and low-grade prostate adenocarcinoma. Pr*ostate 7*1**,** 1759-67 (2011).

79. Elson, D. et al. Time-domain fluorescence lifetime imaging applied to biological tissue. Ph*otochem Photobiol Sci 3*, 795-801 (2004).

80. Hosmer, D.W. & Lemeshow, S. Ap*plied Logistic Regression (*Wiley, John & Sons, Inc: 2000).

81. MATLAB, ver*sion 7.13.0 (R2011b) (The Mathworks, Inc., Natick, Massachusetts) (*2011).

82. Perkins, N.J. & Schisterman, E.F. The inconsistency of "optimal" cutpoints obtained using two criteria based on the receiver operating characteristic curve. Am *J Epidemiol 16***3,** 670-5 (2006).

83. Hastie, T., Tibshirani, R. & Friedman, J. The *Elements of Statistical Learning, Data Mining, Inference, and Prediction (*Springer: 2008).

84. Ng, A. Machine Learning Course at Stanford (CS229) Lecture notes. (2011).

85. Sharma, V. et al. Optical reflectance spectroscopy for detection of human prostate cancer. Co*nf Proc IEEE Eng Med Biol Soc 2*0**09,** 118-21 (2009).

86. Brown, J.Q. et al. Optical assessment of tumor resection margins in the breast. IE*EE J Sel Top Quantum Electron 1*6**,** 530-544 (2010).

87. The Ohio State University, All about prostate cancer. (2012).

88. Rahman, G.A. Breast Conserving Therapy: A surgical Technique where Little can Mean More. J *Surg Tech Case Rep 3*, 1-4 (2011).

89. Pleijhuis, R.G., Graafland, M. & De Vries, J. Obtaining adequate surgical margins in breast-conserving therapy for patients with early-stage breast cancer: current modalities and future directions. An*nals of surgical 1*6**,** 2717-2730 (2009).

90. Singletary, S.E. Surgical margins in patients with early-stage breast cancer treated with breast conservation therapy. Am *J Surg 1*8**4,** 383-93 (2002).

91. Demos, S.G., Vogel, A.J. & Gandjbakhche, A.H. Advances in optical spectroscopy and imaging of breast lesions. J *Mammary Gland Biol Neoplasia 1*1**,** 165-81 (2006).

92. Nachabe, R. et al. Diagnosis of breast cancer using diffuse optical spectroscopy from 500 to 1600 nm: comparison of classification methods. J *Biomed Opt 1*6**,** 087010 (2011).

93. Kennedy, S. et al. Optical breast cancer margin assessment: an observational study of the effects of tissue heterogeneity on optical contrast. Br*east Cancer Res 1*2**,** R91 (2010).

94. Burgoyne, L.L., Jay, D.W., Bikhazi, G.B. & De Armendi, A.J. Isosulfan blue causes factitious methemoglobinemia in an infant. Pa*ediatr Anaesth 1*5**,** 1116-9 (2005).

95. Liu, H., Gu, Y., Kim, J.G. & Mason, R.P. Near-infrared spectroscopy and imaging of tumor vascular oxygenation. Me*thods Enzymol 3*8**6,** 349-78 (2004).

96. Ramanujam, N. Fluorescence spectroscopy of neoplastic and non-neoplastic tissues. Ne*oplasia 2*, 89-117 (2000).

97. Shrestha, S. et al. High-speed multispectral fluorescence lifetime imaging implementation for in vivo applications. Op*t Lett 3*5**,** 2558-60 (2010).

98. Nath, A. et al. Effect of probe pressure on cervical fluorescence spectroscopy measurements. J *Biomed Opt 9*, 523-33 (2004).

99. Reif, R. et al. Analysis of changes in reflectance measurements on biological tissues subjected to different probe pressures. J *Biomed Opt 1*3**,** 010502 (2008).

100. Lim, L., Nichols, B., Rajaram, N. & Tunnell, J.W. Probe pressure effects on human skin diffuse reflectance and fluorescence spectroscopy measurements. J *Biomed Opt 1*6**,** 011012 (2011).

BIOGRAPHICAL INFORMATION

Vikrant Sharma, born July 27th 1980, received his Bachelor of Engineering degree in Biomedical Engineering from University of Mumbai, India in August 2001. He worked as a Biomedical Engineer in P.D. Hinduja Hospital and Medical Research Center, Mumbai, India for 2 years as a Biomedical Engineer before he started his graduate studies in United States of America. Vikrant received his Master of Science degree in Biomedical Engineering at the Joint Program of University of Texas at Arlington and University of Texas Southwestern Medical Center at Dallas, Texas in August 2005, with a thesis titled “Near Infrared Spectroscopy: A Study Of Cerebral Hemodynamics During Breathholding And Development Of A System For Hot Flash Measurement”. He continued his research with NIH funded project at Baylor Research Institute, Dallas, Texas, for a few years on optical spectroscopy and imaging for applications in neuroscience and oncology. In 2008, he joined a start-up effort, assuming role of company President to lead project proposals and conduct research and development for optical spectroscopy devices. In Spring 2010, he started his Ph.D. in Biomedical Engineering at the Joint Program of University of Texas at Arlington and University of Texas Southwestern Medical Center at Dallas, Texas, completing it by Summer 2012. His research expertise is in medical imaging, optical spectroscopy and signal processing, for applications in medical diagnostics and therapy. His interests include developing novel methods, problem solving and providing engineering solutions to medical problems. In near future, he hopes to contribute in improvement of global healthcare through his work in medical device industry.